PARTICLE CONTAMINATION OF HIGH VOLTAGE DC INSULATORS

by

Mark Nathan Horenstein

S.B., Massachusetts Institute of Technology
(1973)

M.S., University of California (Berkeley)
(1975)

SUBMITTED IN PARTIAL FULFILLMENT
OF THE REQUIREMENTS FOR THE
DEGREE OF

DOCTOR OF PHILOSOPHY

at the

MASSACHUSETTS INSTITUTE OF TECHNOLOGY

May 4, 1978

Signature of Author .....
Department of Electrical Engineering and Computer Science — May 4, 1978

Certified by .....
Thesis Supervisor

Accepted by .....
Chairman, Department Committee

PARTICLE CONTAMINATION OF HIGH VOLTAGE DC INSULATORS

by

MARK NATHAN HORENSTEIN

Submitted to the Department of Electrical Engineering and Computer Science on (May 4, 1978) in partial fulfillment of the requirements for the Degree of Doctor of Philosophy

ABSTRACT

A scaled dc insulator contamination experiment in which the electric field, air flow, and particle dynamics around an insulator string are modeled has been implemented. Outstanding contamination features, including sharp clean rings and leeward wakes on the insulator surfaces, and diffuse contamination bands on the pin caps, are explained using simple trajectory models, which are both qualitatively and quantitatively verified. A simplified contamination model is demonstrated, in which the deposition rate on surfaces that are contaminated is given by the average product of particle mobility, particle mass density, and normal electric field.

Large scale deflection of incident charged particles is shown to be unlikely. Segregation of oppositely charged particles to upper and lower regions of the insulator string is observed, but explained via a trajectory perturbation analysis.

A dynamic particle charging model suggests that corona ions may be capable of charging initially neutral particles to values comparable to naturally occurring mobilities.

Design concepts for improved dc insulators, aimed at minimization of the normal electric field on insulator surfaces, are offered. The time average "particle mass density-collection time product" is indicated as a good parameter for evaluating contamination severity at both existing and proposed dc transmission line sites.

THESIS SUPERVISOR: James R. Melcher

TITLE: Professor of Electrical Engineering

Acknowledgements:

I would like to extend my thanks to the many individuals whose help and influence led to the completion of this thesis. Prof. James R. Melcher, my thesis advisor, provided me with overall direction, and gave good insight and unique approaches to the problems encountered. He likewise introduced me to the theoretical fundamentals upon which the models presented here are based. Dr. David Jolly, staff researcher at MIT Electric Power Systems Engineering Laboratory (EPSEL), managed the contract under which this work was performed. He also helped me with various experimental problems, and provided overall perspective of the significance of this work to the engineering world. His infamous dry wit has been a source of great moral support. Dr. Jolly, and research assistants Fred Donahue and Ed McHale were responsible for the initial stages of construction of the experimental test chamber.

Several undergraduates deserve recognition for their contributions to the experiment. Craig Poole performed admirably during the unpleasant and messy orange dust phases of the experiment, when the management techniques (often poor) and measurement proceedures (often tedious) for the test contaminant were developed. My apologies to the members of EPSEL for fluorescent fallout experienced during this peroid of time. Rick Baer constructed the generating voltmeter used for the voltage distribution measurements reported in Appendix C. Alan Barnett constructed the mobility measuring device, unofficially

named the Barnettometer, as part of his Bachelor's thesis. The electrolytic tank was constructed rather creatively by R. Steve Colby, who, along with Alan Presser, performed the tedious macroscopic field measurements of Chapter 4.

Prof. Markus Zahn of the University of Florida, who was at MIT for the academic year 1976-77, contributed many helpful discussions about some of the early theoretical aspects of the thesis.

Special commendation is due my officemates and other colleagues at EPSEL, for their plight in tolerating my unpublishable, but nonetheless colorful phrases coined during times of duress. These will no doubt become part of the permanent EPSEL vocabulary. Likewise my thanks to the countless smiling faces that make the lab a human place in which to work.

My thanks to Margaret Underdown, who did a fine job of typing this thesis. I marvel at her efficiency, and often wish I had more of my own.

Finally, I would like to thank the other members of my thesis committee. Prof. John Trump has contributed much of his experience, gleaned over many years of High Voltage research, in providing perspective over the role of this research in the High Voltage area. Prof. Gerald Wilson, director of EPSEL, has kept me aware of the relationship between my research and the rest of the power industry, and provided important insight into many phases of the investigation. Prof. Wilson also provided the moral support necessary to conduct research when confronted

with the realities of daily life. I feel fortunate to have been able to work within the EPSEL laboratory.

This work was sponsored by the United States Department of Energy (formerly ERDA), under contracts No. E(49-18)-2068 and EC-77-S-01-5003. I gratefully acknowledge this source of financial support during the period of my Research Assistantship.

TABLE OF CONTENTS

TABLE OF CONTENTS (Contd.)

TABLE OF CONTENTS (Contd.)

LIST OF FIGURES

LIST OF FIGURES (Contd.)

LIST OF FIGURES (Contd.)

LIST OF FIGURES (Contd.)

LIST OF TABLES

LIST OF VARIABLES

(All units are SI units unless otherwise noted)

a	radius of line conductor
a	subscript referring to "actual" system
A	coefficient of linear algebraic equations
A	area
$\bar{A}$	vector potential
b	particle mobility (reflects sign of charge)
B	coefficient of linear algebraic equations
c	factor used in corona equations - defined in Eq. (6.2)
C_m	parallel capacitance of generating voltmeter
d	insulator disk thickness
D	diameter
e	electronic charge: 1.6×10^{-19} coul
$\bar{E}$	electric field
E_o	ambient electric field
E_c	general variable for field strength at surface of line conductor
E_p	Peek's field strength at surface of line conductor in corona
$E_\perp$	normal component of electric field on a surface
$E(k)$	complete elliptic integral of the second kind
$\bar{F}$	force
$g(t)$	fraction of q_{sat} to which a given particle is charged, i.e. q/q_{sat}

h	heat transfer coefficient
i_c	line corona current
I	current
$\bar{J}$	current density
$K(k)$	complete elliptic integral of the first kind
k	argument to elliptic integrals - defined in Eq. (5.13)
kT/e	thermal voltage
ℓ	general physical dimension
ℓ	half vertical distance between adjacent insulator skirts
L	specific physical dimension, length
m	subscript referring to "model system"
m	particle mass
m	total mass of a collection sample
M	average insulator contamination in kg
N	particle number density (particles per m^3 of air)
N	total number of charges in charge simulation
n	number of insulators on a string
n	summation index indicating location of point or ring charge
$\bar{n}$	outward directed unit vector normal to a given surface
p	summation index indicating location of point where potential is to be matched
P	precipitation rate
P_{xx}	power
q	particle charge

Q	$q/4\pi\varepsilon_o$
r	radial distance
r_d	clean ring (demarcation ring) radius
r_i	inner insulator radius (radius of pin cap)
r_o	outer insulator radius (skirt radius)
r_q	radius of ring charge
r_t	small radius of toroidal shell
R_h	relative humidity
R_m	parallel resistance of generating voltmeter
R_o	outer coaxial shell radius
R_p	particle radius
R_s	surface resistance
R_y	Reynolds number for fluid flow
S	volume sample rate m^3/sec
t	time
T	collection time
T_{xx}	temperature
U	wind velocity
U_o	ambient wind velocity
$\bar{v}$	wind velocity vector
$\bar{v}_p$	particle velocity
$\underline{V}$	normalized voltage constant
V	voltage
V_c	corona onset voltage
V_o	voltage across a single insulator
W	width

$\bar{x}$ generalized position vector

x position coordinate

z height

z_c linear-logarithmic potential crossover point

α, β mass loading measurement calibration factors

α, β factors used in elliptic integrals - defined in Eq. (5.13)

$\bar{\Gamma}$ particle flux density

δ layer thickness

ε_o permittivity of free space - 8.85×10^{-12} coul/v-m

Φ potential

η kinematic air viscosity - 1.83×10^{-5} n-sec/m^2

ρ particle mass density - mass of particles in one m^3 of air

ρ_c space charge density - coul/m^3

ρ_g gas density - kg/m^3 (air)

ρT mass density-collection time product

$\overline{\rho T}$ time averaged mass density-collection time product

σ_s surface conductivity

σ_v volume conductivity

σ factor in Boltzmann distribution

τ time constant

θ angle

ϕ angle

$\frac{1}{\xi}$ factor used in corona equations $= \left[\frac{i_c}{2\pi\varepsilon_o b}\right]^{1/2}$

CHAPTER 1

INTRODUCTION

The transport of electricity from power plant to load has been accomplished, since the early days of power generation history, by high voltage ac transmission lines. The difficulty encountered in converting ac to dc at high voltages and large power levels has always dictated high power dc lines to be unfeasible. The last two decades or so have seen the successful development of high power, high voltage switching and rectifying devices, and with them the attractive possibility of interfacing ac to dc at high voltage levels. Direct current transmission lines operating at hundreds of kilovolts are now an engineering reality, and successful dc links between ac systems now appear on a limited worldwide scale.[12] This innovation in power transmission, and its associated advantages from a power system point of view, have stimulated interest in new dc insulation problems that have since become evident. While general rules of thumb and years of field experience have long dictated insulator design for ac lines, a lack of understanding of dc insulation, contamination, and flashover processes has left a void in the design and selection of dc insulators. At present, dc lines utilize those ac insulators that have performed best under a limited number of withstand voltage tests, but no insulators have been specifically designed for dc use.

While field reports are scanty from the several dc lines that exist worldwide, experiences with the first line in the U.S. indicate severe flashover difficulty over certain sections of the line. The link in question, the Pacific Intertie, extends some 800 miles from The Dalles, Oregon, to suburbs just outside Los Angles, and normally ships surplus hydropower from the Pacific Northwest to the predominantly fossil fired areas of Southern California. In service since 1970,[8] the line has had no unusual difficulties, except for a short section just outside the Sylmar, California converter station, where contamination of the dc insulators is so severe, and flashover so frequent, that the insulators are hot-line washed regularly by a full time crew working seven days a week. Observations at Sylmar indicate the dc hardware to be constantly covered by dirt and contaminants, while adjacent ac hardware remains virtually dirt free.

While efforts aimed at solving this particular problem motivate current dc contamination and flashover research at MIT, it is clear that the fundamental understanding of dc insulation phenomena that will be gained from the work done here will be valuable to designers of dc lines everywhere. Although the mechanisms contributing to flashover of contaminated dc insulators are also being investigated by our research group at MIT, the scope of this thesis focuses on the mechanisms by which the insulators become contaminated in the first place. It is certain that before the problem of dc contamination can

be corrected, a better understanding of the fundamental processes by which insulators become contaminated is needed.

Why do insulators under dc service become contaminated far more rapidly than their ac counterparts? The basic differences between ac and dc contamination phenomena have long been recognized.[15,33,13] In particular, charged airborne particulate that approach an energized ac insulator cannot respond quickly enough to the surrounding electric field before the 60 Hz field changes polarity, and the direction of the particle force is reversed. In other words, charged particles around an ac insulator experience no time average coulomb force. On a dc line the coulomb force is most certainly relevant. If the ac line emits any corona, the space charge surrounding the conductor will change sign each half cycle,[10] while any dc space charge will be monopolar, and thus capable of charging otherwise neutral contaminant particles that enter the space charge region. It has been generally recognized by most previous investigators[1,15,33] that there are four important forces acting on contaminant particles: coulomb force, wind drag force, gravity, and polarization force. Of these four forces, only the coulomb force is irrelevant to ac contamination. Thus one may expect it to be a key element of the dc contamination theory. A usable contamination theory likewise must presume a knowledge of the charge of the contaminant particles that surround the insulators and respond to the coulomb force.

The major part of this thesis deals with contamination phenomena in which the corona emitted from the line conductor has little effect. Modifications to the contamination theory due to the presence of corona are considered in Chapter 6. The charge to be found on particles in nature may generally be attributed to processes of all sorts, including frictional electrification, combustion processes, and ion diffusion charging. For particles in the 1.0 micron range, charges of 10^{-3} to 10^{-4} coul/kg are typical,[34] and suggest a range of mobility to be considered when examining the contamination problem. Because one of the goals of this research is a prediction of contamination on actual energized dc insulators, a measurement of particle mobilities at sites of relevance should augment use of the contamination theories in the subcorona regime.

The long-term goals of this work are twofold. First, as mentioned, a fundamental understanding of the deposition process should make it possible to predict how fast insulators in the field will become contaminated, given onsite data like particle density, mobility distribution, and average wind velocity. With knowledge gained from the flashover experiments, it should likewise be possible to estimate the frequency of insulator flashover. Second, the knowledge herein gained should be useful to those engaged in the design of improved dc insulators. Indeed, the implications of the contamination theory to be described in the following chapters suggest some

straightforward modifications to the design of disk suspension insulators that seem quite practical for reducing experienced insulator contamination. These basic design modifications are presented and evaluated in Chapter 7.

In this thesis, the assumption is made that once a particle strikes the insulator surface, it remains there indefinitely. According to currently available evidence, this assumption will generally be valid for the range of particle sizes considered in the study. Typically, only larger diameter particles suffer reentrainment.[26] The effects of rain washing as a natural cleansing mechanism for contamination should ultimately be integrated into any overall prediction of mean time to insulator flashover. Nevertheless, for periods of time between rainfalls, the contamination theories presented here are useful for estimating the accumulation of contaminants. Likewise, not all contaminants are cleansed by rainfall--for example certain organic contaminants may form sticky, insoluable residues on insulator surfaces which tend to hold other contaminant particles. Hence, the contamination theories in this thesis have general applicability to the design and evaluation of dc insulators.

CHAPTER 2

CONCEPT OF THE LABORATORY EXPERIMENT

2.1 The Scaling Philosophy

Obtaining data from actual field insulators can be an unwieldy and time-consuming process, due to the physical location of equipment involved. Another major problem encountered when testing actual insulators in the field is the impossibility of controlling the many variables that may contribute to the contamination process. Wind, humidity, rainfall, particle type, particle size and particle charge cannot be chosen by the experimenter when testing in the field. These variables are somewhat controllable in the laboratory -- however, the physical size of actual insulators limits the degree to which the configuration of insulator string and transmission line conductor can be duplicated. The basic philosophy adopted for contamination work at MIT has been to construct a scaled down version of an insulator and conductor, in order to simulate and control, as closely as possible, the conditions found in the field. A scale model experiment offers several distinct advantages over full sized insulator tests. The capability of running tests under repeatable conditions is greatly enhanced, and the turnaround time between tests is of course quite short, since the small insulators are easy to manipulate. Furthermore, the variables of the scale model experiment can be changed one at a time to test various hypotheses about the

contamination process.

Until a detailed understanding of contamination can be formulated, it is difficult to determine which fundamental physical laws are most important to the contamination process. It is therefore essential, when designing a scaled experiment, to simulate the fundamental parameters of as many of these laws as possible, so that complicated phenomena based on them will proceed in similar ways in the real and model systems. In our experiment we have set down a hierarchy of parameters and physical conditions that should be matched as closely as possible between the two systems.

2.2 Physical Size

A convenient scaling factor for the physical dimensions is 1:5. All dimensions for the insulator hardware used for most of the experimental work thus follow:

$$\frac{\ell_m}{\ell_a} = \frac{1}{5} \tag{2.1}$$

where "m" and "a" refer to the "model" and "actual" systems respectively, and ℓ is any physical dimension of relevance. For geometrical scaling factors other than 1:5, the ratio $\frac{\ell_m}{\ell_a}$ may still be considered a fixed constraint of the scale model.

2.3 Air Flow Pattern

The wind, besides carrying particles into the

neighborhood of the insulators, is thought to exert a significant force on the particles in the contamination process.[1,33,15] It is therefore important to duplicate the airflow around the insulator in the model system. This duplication may be difficult to accomplish because as it approaches the insulator the air will have some characteristic turbulent structure. Although the issue of turbulence, and the size of turbulent eddies and turbulent diffusion are important ones that must certainly be addressed, a minimum criterion for the duplication of the airflow in the two systems requires that, for windspeeds of practical interest, a constant Reynolds number be maintained. Reynolds number, the ratio of inertial to viscous forces in the air, is defined, for incompressable flow, by

$$R_y = \frac{\rho_g U \ell}{\eta} \tag{2.2}$$

where ρ_g = gas density, U = ambient average wind speed, ℓ = scale dimension, and η = air viscosity. Both ρ_g and η are the same in both systems, and we have already specified the relationship between ℓ_m and ℓ_a, whence:

$$\frac{\rho_g U_m \ell_m}{\eta} = \frac{\rho_g U_a \ell_a}{\eta}$$

implies

$$\frac{U_m}{U_a} = \frac{\ell_a}{\ell_m} \tag{2.3}$$

for the relationship between the wind velocities. In practice, the range of U_m will be limited by experimental constraints, thereby likewise dictating a limited range of actual wind velocities that may be properly modeled.

2.4 Electric Field Pattern

Since another major force on the contaminant particles is the coulomb attraction, it is important to maintain geometrically similar electric field patterns around the insulator string. It is difficult to simulate exactly in the laboratory the fields between the conductors of the actual line and the ground plane of the earth, because the laboratory dimensions are not of infinite extent, hence some approximation is required. Far away from the insulator, the electric field tends to be determined by the conductor geometry, and, in the case of the scale model, by the boundary conditions at the walls of the test chamber. The grounded floor of the test chamber represents the ground plane of the earth beneath the actual transmission line. At the same time, the grounded walls on either side of the line, which are perpendicular to the floor, produce opposite electrostatic images of the energized line. The field from these images on either side of the line models to some extent the field existing in between the two conductors of the actual bipolar line, although of course this similarity is not exact. Space limitations do not permit exact scale modeling, in accordance with the geometric scaling

ratio Eq. (2.1), of the complete conductor-to-ground plane, and conductor-to-conductor fields. The steel support towers present on the actual line are also not modeled in the experiment. Nevertheless, the scale model does account for the general nature of the field around the actual transmission line, and, more importantly, its relative magnitude in the vicinity of the line conductor and insulator string.

In the near vicinity of the insulator string, the field is for the most part determined by the potential distribution along the surface of the insulators, as dictated by their surface conductivity. It is this second region of electric field that can be accurately modeled; the differences in field far from the conductor must be taken into account when interpreting the experimental data.

For potential distributions determined by Laplace's equation, linearity implies that, when a voltage V is applied to the conductor, geometric similarity between the two electric field patterns in the sub-corona regime can be preserved provided that:

$$\frac{V_m}{\ell_m} = \frac{V_a}{\ell_a} \tag{2.4}$$

2.5 Particle Mechanics

The two major forces acting on a particle -- wind drag and coulomb attraction -- must likewise be kept in proper proportion when setting up the model experiment. The viscous

dominated model for the wind force on the particle neglects the effect of particle inertia in determining particle motion. The appropriate viscous term in the particle equation of motion is the Stokes' drag force:

$$\bar{F}_{drag} = -6\ \pi\eta\ R_p(\bar{v}_p - \bar{v}) \tag{2.5}$$

where η is again the viscosity of air, R_p = radius of the particle, $\bar{v}_p$ the velocity of the particle in the lab frame, and $\bar{v}$ the velocity of the surrounding air. Thus $(\bar{v}_p - \bar{v})$ is the velocity of the particle relative to the surrounding air. Stokes' drag is valid for particles down to about .5 microns in size, below which Brownian motion becomes important, and up to about 10 microns, where the Reynolds number based on R_p and $\bar{v}_p$ of interest approaches unity.[4] The equation of motion for a particle in this size range becomes:

$$m\ \frac{\partial^2 \bar{x}}{\partial t^2} + 6\ \pi\eta\ R_p\ (\frac{d\bar{x}}{dt} - \bar{v}) = qE \tag{2.6}$$

where m is the particle mass, and $\bar{v}$ the ambient wind velocity. From the equation (2.6), we see that acceleration times for the particle are on the order of $\tau \sim \frac{m}{6\pi\eta R_p}$, or about 5×10^{-4} seconds maximum for particles of unity density. Times of interest in examining particle motion are characterized by ℓ/U, which equals 10^{-2} sec if ℓ = 1 cm and U = 1 m/sec. Hence the acceleration time required for the particle to reach terminal velocity is usually negligible, and the inertialess

model for particle motion is valid. The particle is thus assumed to instantly acquire that velocity relative to the wind at which the Stokes' drag and coulomb forces just balance:

$$\bar{F}_{coul} + \bar{F}_{wind} = 0 \tag{2.7}$$

$$q\bar{E} - 6\,\pi\eta\, R_p\,(\bar{v}_p - \bar{v}) = 0$$

$$(\bar{v}_p - \bar{v}) = \frac{q\bar{E}}{6\pi\eta R_p}$$

or:

$$\bar{v}_p = \left[\frac{q}{6\pi\eta R_p}\right]\bar{E} + \bar{v} \tag{2.8}$$

Note that in the absence of an electric field, the particles travel along with the ambient wind velocity. The expression in brackets in (2.8) is commonly referred to as the particle mobility "b" (m^2/v-sec) and defines the drift velocity at which a particle travels under the influence of an electric field in the absence of any other forces.

Of all the quantities involving particle motion that could be preserved when setting up the model experiment, the one that is considered most important is the ratio of drift velocity due to electric field, to average wind velocity. Implicit in this choice is the assumption that, at least to some degree, the particles follow trajectory-like patterns that are determined by these two velocities at each point along the particle's path. For a particle of a given charge

and size, then, preserving the ratio of electric drift velocity to average wind velocity assures that the trajectories will likewise be preserved when going from actual to model systems, since the electric field and airflow patterns are presumed similar. What is neglected here, once again, is the effect of turbulence on the motion of the particles -- turbulence, for example, upsets the trajectory picture and makes the particle motion quite random. Nevertheless, if the scale of turbulence is much smaller than the insulator dimensions, the particles will have some trajectory-like behavior, and the preservation of this behavior can be accomplished by setting

$$\frac{\text{drift velocity}}{\text{wind velocity}} = \frac{bE}{U} = \text{constant.} \qquad (2.9)$$

In light of the previously determined requirements on E_m and U_m, this required relation implies:

$$\frac{b_m}{b_a} \equiv \frac{q_m/R_{pm}}{q_a/R_{pa}} = \frac{U_m\ E_a}{U_a\ E_m} = \frac{\ell_a}{\ell_m} \qquad (2.10)$$

Note that satisfying (2.10) allows some latitude in the exact values of q and R_p, provided they fall in proper ratio. Nevertheless, the actual value of R_p in both the actual and model systems must fall in the range for which the Stokes' drag term and inertialess approximation are both valid. Likewise, the particle charge q must of necessity lie

below the maximum saturation charge allowed the particle.

2.6 Surface Conductivity of Insulators

The electric field in the near vicinity of the insulator string is dictated by the potential distribution along the insulator surfaces. On glass and porcelain materials, this surface potential distribution is in turn determined by the surface conductivity, which is generally several orders of magnitude higher than the bulk conductivity. In its simplest approximation, the surface conductivity σ_s of nonporous materials, attributable to an adsorbed moisture layer, may be expressed by:[17,27,28]

$$\frac{1}{\sigma_s} = \lim_{W,L\to 0} \frac{W}{L} R_s \tag{2.11}$$

where W and L are the width and length of a rectangular patch of the surface having resistance R_s. The following relation involving the bulk conductivity σ_v of the adsorbed moisture film and its thickness δ:

$$R_s = \frac{L}{\delta W} \cdot \frac{1}{\sigma_v} \tag{2.12}$$

although probably an oversimplification of the true physical processes occurring on the surface, illustrates the notion of how surface conductivity is related to the bulk conductivity of the adsorbed moisture layer.

If σ_s is uniform everywhere on the insulator surface, the potential distribution, and hence electric fields in the immediate vicinity of the insulators, will be determined only by the insulator geometry. The scaling of electric fields specified in Section 2.4:

$$E_m = E_a \tag{2.13}$$

is thus achieved regardless of the ratio of $\frac{\sigma_{sa}}{\sigma_{sm}}$. Problems arise when one considers thermal processes, like local heating of the adsorbed moisture layer by surface currents, which tend to make σ_s nonuniform. Achieving the desired goal of $E_m = E_a$ around the insulators is thus tantamount to assuring that, locally, $\sigma_{sm} = \sigma_{sa}$ everywhere on the insulator. Note that σ_s may be regarded as a function of position when its uniformity is disrupted.

It must be emphasized that we seek scaling of only gross changes in field distribution caused by local heating, as may occur for example at the base of the metal insulator caps. The model insulator will not in practice duplicate any of the fine structural details prominent on actual insulators; rather, only the general shape of the insulator will be modeled. Similarly, it is impractical to account for the fine details of surface thermal processes likely to occur about intricate insulator surfaces. Hence, the modeling and scaling of thermal processes to be presented here is

approximate, but sufficient for our purposes.

A rather good synopsis of research on surface conductivity may be found in Ref. (17), where the experimental data of many researchers is shown to empirically fit the relation:

$$\sigma_s = \sigma_{so}\, e^{-k(1-R_h')^2} \qquad (2.14)$$

In the above expression, R_h' is the "effective" relative humidity* of the surrounding air, σ_{so} is the surface conductivity measured at the dew point of the air, and k is an empirical constant. The temperature dependence of R_h' may cause exponential changes in σ_s. Although R_h' can in principle be determined from steam tables or other tabulated data, this task need not be performed here, because R_h' will have a temperature dependence unrelated to the insulator size scale provided that:

Model ambient temperature = Actual ambient temperature

Model relative humidity = Actual relative humidity

and that the distributions of temperature over the insulator surfaces are identical. The first two "ambient" requirements are easily met. The requirement concerning local surface temperature distribution can be approximately fulfilled. The

---

*Relative humidity $\triangleq \frac{\text{partial vapor pressure}}{\text{saturation vapor pressure}}$ at a given temperature.

Effective relative humidity $\triangleq \frac{\text{partial vap. pres. at air temperature}}{\text{sat. vap. pres. at substrate temp.}}$

primary source of local surface heating is thought to be due to surface leakage current. Thus the power input to a given incremental area of surface film is

$$P_{in} = E_{||}^2 \sigma_s \quad \text{watts/m}^2 \tag{2.15}$$

where $E_{||}$ is the tangential electric field across the surface film. In the steady state, the power lost by the incremental area is primarily due to convection into the surrounding air:[28]

$$P_{lost} = h(T_1 - T_0) \quad \text{watts/m}^2 \tag{2.16}$$

where T_1 is the local surface temperature, and T_0 the ambient temperature. The heat transfer coefficient h in the above expression will be discussed shortly. At equilibrium,[28]

$P_{in} = P_{lost}$

$$\therefore \quad (T_1 - T_o) = \frac{(E_{||})^2 \sigma_s}{h} \tag{2.17}$$

Note at this point that all the scaling goals are self consistent: The requirement $E_m = E_a$ is achieved by duplicating the potential distribution on the insulator surfaces. The latter is determined by the temperature dependent value of σ_s on the surface, but the temperature distribution is in turn determined by σ_s, the electric field distribution, and the value of heat transfer coefficient h.

Given that we would like $E_{||}$ and σ_s to be identical in the model and actual systems, all the scaling requirements can be met if h is also made identical in the model and actual systems. Again, it must be emphasized that the thermal modeling is only approximate, and meant to underscore only gross field distortions attributable to local joule heating.

The value of the heat transfer coefficient is not a constant, but very dependent upon the circumstances under which heat flow takes place. For example, forced convection and natural convection conditions lead to different values of h, as do the specifics of the geometry of the system being analyzed. Detailed analysis of these issues is of questionable value, however. The two important parameters effecting h that differ in the model and actual systems are the ambient wind velocity and the physical size of the insulators. For all practical conditions likely to be found on both the actual and model systems, h varies only by weak powers of physical size or, if applicable, wind velocity.[25] Hence, for any given location and set of conditions under which heat flow takes place, h may be assumed a constant of the model and actual systems.

The self-consistent goals of maintaining identical electric fields, surface conductivity, and insulator surface temperature are thus met by making the model insulator of materials similar to those comprising actual insulators, i.e. glass or porcelain, so that σ_s will generally be the same.

As shown in Chapter 3, the model insulators for the experiment described here are conveniently made of glass.

As a general rule, all experiments reported in this work were performed at a relative humidity of 50 $\pm$ 5%.

2.7 Summary of Scaled Parameters

The various parameters of the scale model system, and the corresponding values thus represented in the real world, are summarized in Table 2.1, for a scale size of 1:5. The quantities and physical processes that are scaled by no means form a complete set -- no scale model can duplicate an arbitrary number of physical processes. In terms of the physical processes considered important to contamination, however, the model system will resemble the actual Pacific Intertie line closely enough to allow the contamination process to be duplicated to a reasonable degree. Although the model wind velocity range is somewhat low, it serves, as is made evident in Chapter 4, to accentuate the interplay between wind forces and electric field forces in determining the behavior of contaminant particles.

Table 2.1

Summary of Scaled Parameters

Parameter	Units	Scale Factor	Model Value in Experiment	Actual Value Represented
Insulator Diameter	cm	$\frac{\ell_m}{\ell_a} = 1:5$	5.08	25.4
Insulator Separation	cm	$\frac{\ell_m}{\ell_a} = 1:5$	1.9	9.5
Wind Speed	m/sec	$\frac{U_m}{U_a} = 5:1$	.2 -.5	.04-.1
Line Voltage	kV	$\frac{V_m}{V_a} = 1:5$	$\pm$ 75 (nom)	$\pm$ 375
Particle Mobility	m^2/v-sec	$\frac{b_m}{b_a} = 5:1$	5×10^{-7}	1×10^{-7}
Insulator Surface Conductivity	mho	$\frac{\sigma_{sm}}{\sigma_{sa}} = 1:1$	$10^{-12} - 10^{-14}$	$10^{-12} - 10^{-14}$

CHAPTER 3

THE CONTAMINATION TEST FACILITY

3.1 Excitation System

The test facility that was constructed for the scale model contamination tests, under the guidelines set forth in the previous chapter, is depicted in Fig. 3.1. The half wave power supply is capable of producing up to 120 kilovolts dc. Positive or negative polarity may be selected by reversing the direction of the "diode". This diode is really a series of 20 kV PIV semiconductor diodes and limiting resistors, in parallel with some transient smoothing capacitors. A schematic and i-v curve for the string are shown in Fig. 3.2. For comparative testing, ac voltages may be obtained by connecting the transformer secondary directly to the chamber feed through bushing.

Output voltage is adjusted by a remotely controlled, motorized variac on the transformer primary, and is monitored by measuring the primary voltage with a panel-mounted Fairchild digital voltmeter and rectifier circuit. Likewise, line corona current is monitored by measuring the ground return current to the transformer with another digital panel meter and simple RC filter.

Figures 3.3 and 3.4 show schematic diagrams of the voltage and current monitoring circuits. When using the supply, great care is taken to assure that only the line conductor, and not associated hardware fittings of the power supply,

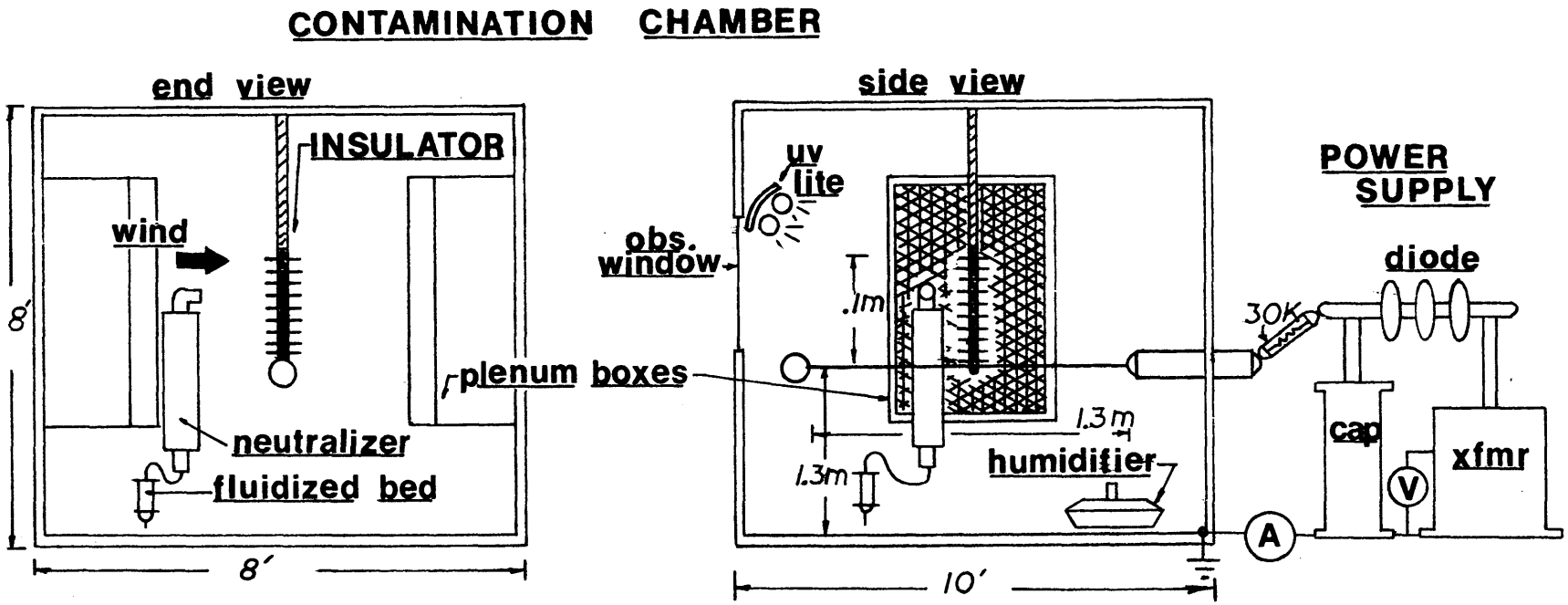

Figure 3.1 Contamination Test Facility. For clarity, the drawing is not to scale, and the neutralizer is shown offset from the insulator string in the side view.

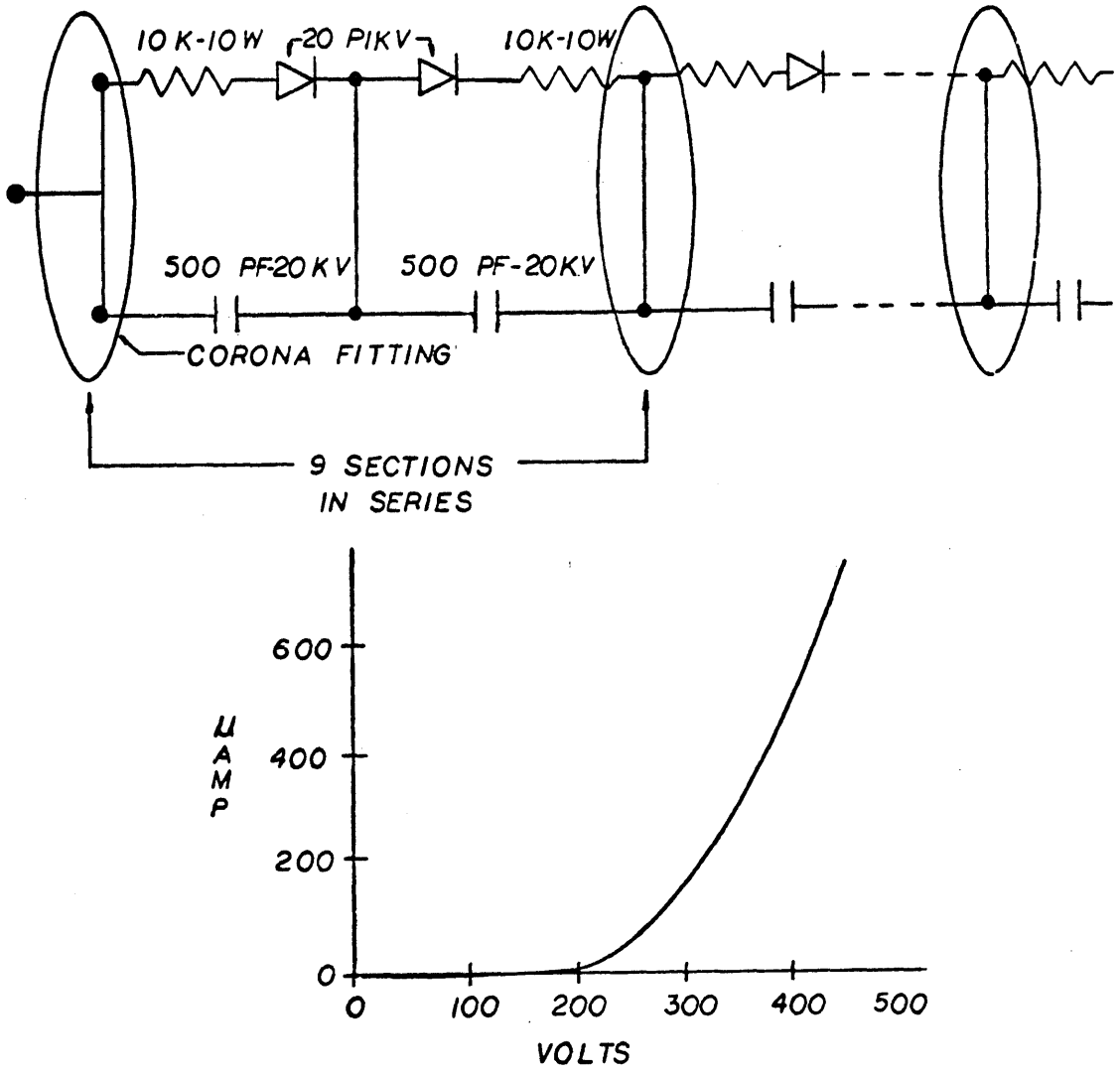

Fig. 3.2 High Voltage Diode Schematic and Measured I-V Characteristic

emit corona current at the highest voltage levels employed. Sharp corners are covered with corona fittings or modeling clay, and the ends of the line conductor are supported by specially designed aluminum bushings. Any corona current emitted by the model line conductor is collected on the walls of the test chamber, which are lined with grounded aluminum sheet for safety reasons.

3.2 Wind Generating System

To establish a uniform wind flow across the model insulator, two honeycomb port plenum boxes were constructed as depicted in Fig. 3.5.

Measurements of the air flow velocities around the test chamber were made with a hot wire anemometer. Initially, the air passed directly out of the upstream plenum box through the honeycomb without the auxiliary baffles, but an extremely non-uniform flow profile resulted. After several cut-and-try installations of additional pressure drop baffles behind the honeycomb, the scheme depicted in Fig. 3.5 was chosen, where standard 1/8" or 1/4" hole pegboard is placed approximately four inches behind the upstream honeycomb, and a denim filter cloth placed behind the honeycomb in the downstream box. The purpose of this filter cloth is to trap contaminant dust particles that have been injected upstream of the insulator, but have not deposited on it, so that they do not recirculate through the blower intake hose and arrive at the upstream plenum box. Re-circulation of this sort was responsible for

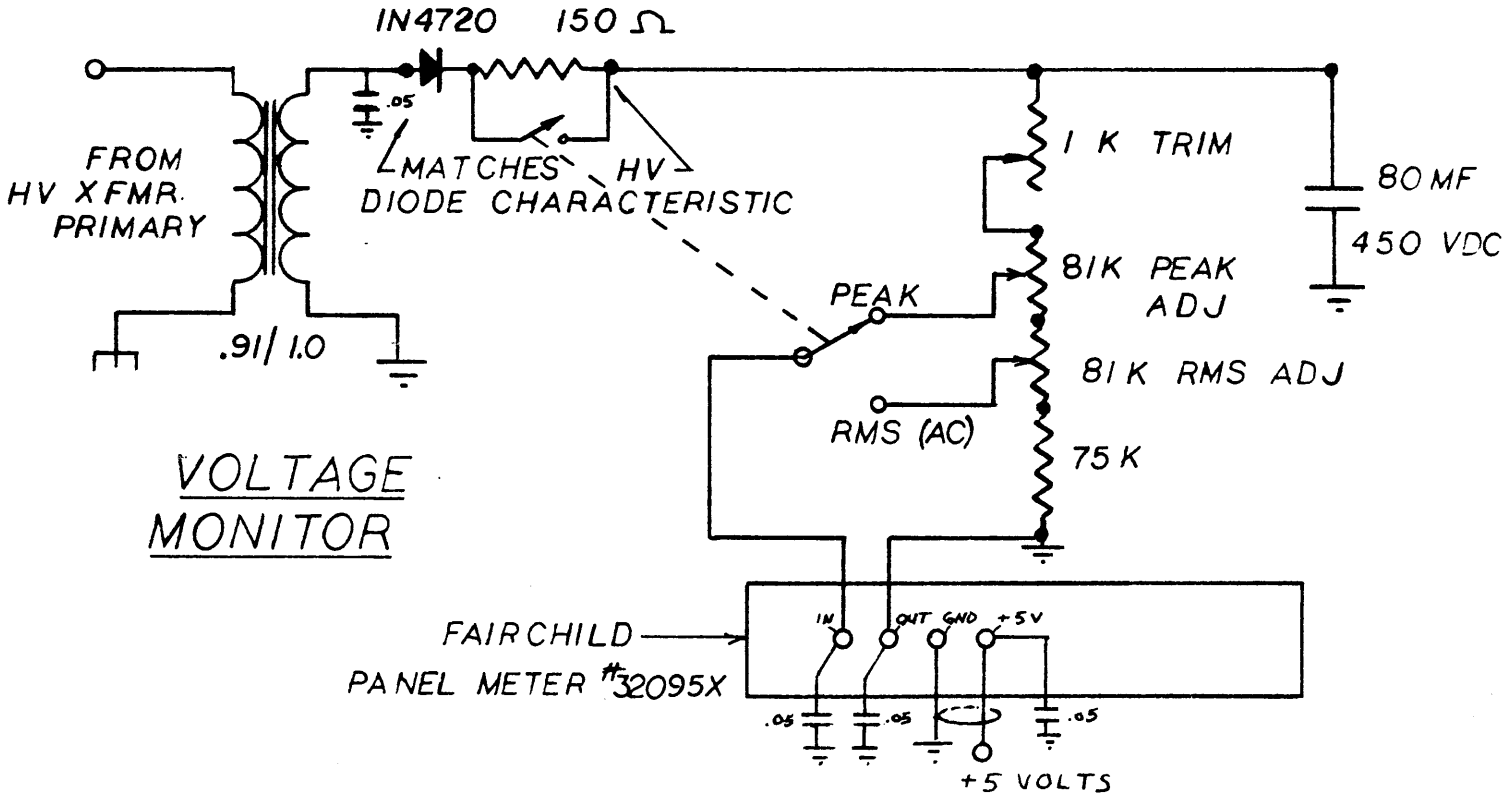

Figure 3.3 High Voltage Monitoring Circuit

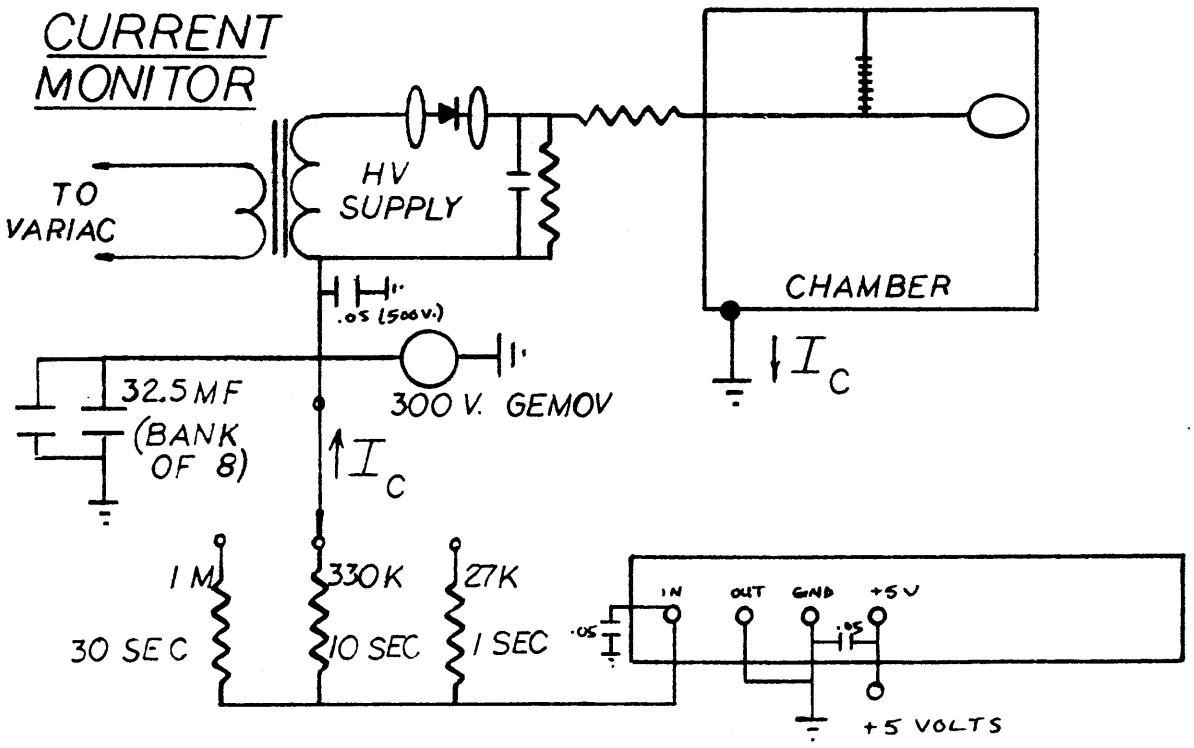

Figure 3.4 Corona Current Monitoring Circuit

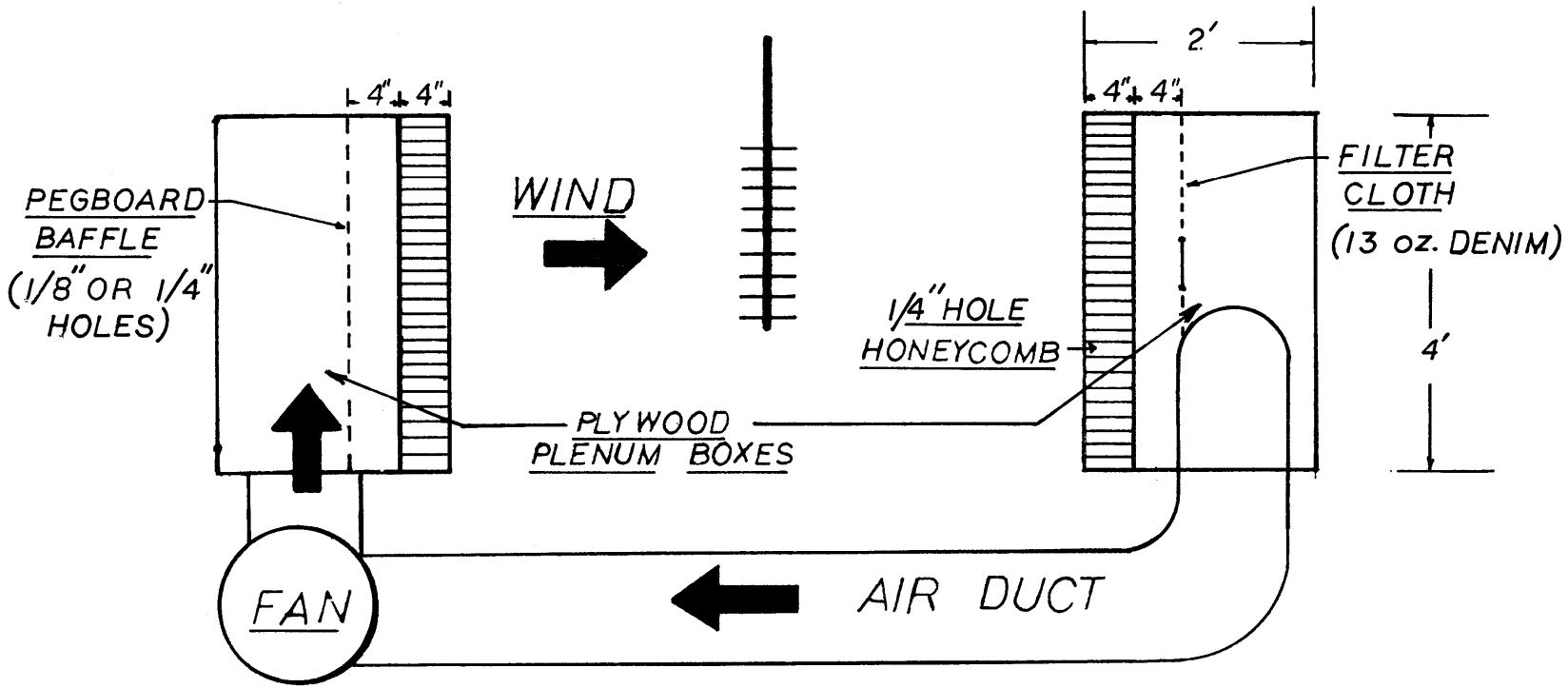

Figure 3.5 Wind Generating System

extremely frustrating failures when initially testing the particle neutralizing device to be described in Section 3.3, because the recirculating particles most certainly become frictionally charged somewhere along their journey.

A matrix of wind velocities, taken point by point in the test chamber with the hotwire anemometer, is given in Table 3.1. As was suggested in Section 2.3, the average wind velocities achievable are really too low to model the range of wind speeds found in the field, but are limited by both the capabilities of the fan, and the need to smooth out the air flow by means of the baffles. Future modifications of the experiment should specifically address this issue.

3.3 Particle Injection

An important consideration in any facility to be used for contamination studies is of course the type of laboratory contaminant, and the method used for injecting the particles into the system. Investigators in the past have used kaolin or alumina particles [1] or even sawdust [33] as the primary contaminant. While these materials are useful for visually observing contamination on the insulators, they may be difficult to produce in monodisperse form, and measuring the amount of their deposition is limited to weighing techniques. While weighing is somewhat useful as an analytical tool, the added weight of the contaminant after any test is usually orders of magnitude smaller than the weight of the insulator

Table 3.1 Matrix of Wind Velocities Taken in Plane of Insulator String and Line Conductor

TABLE 3.1a MATRIX OF WIND VELOCITIES BOTH PEGBOARD BAFFLES

.65	.75	.75
.65	.60	.65
.50	.50	.60
.50	.50	.60

APPROXIMATE LOCATION OF INSULATOR STRING

(VELOCITIES IN METERS/SEC)

TABLE 3.1b MATRIX OF WIND VELOCITIES FILTER CLOTH INSTALLED

.30	.40	.45
.40	.30	.30
.25	.25	.15
.30	.25	.25

itself, so that "before-and-after" weighing methods may be inaccurate. Likewise, any scheme that attempts to remove the contaminant from the insulator surface by washing is subject to inaccuracies due to particle loss. Of course both the washing and weighing methods are limited to measurements of total deposition on the insulator as a whole, or perhaps at best to entire top and bottom surface deposition measurements. With the intent of developing an optical detector capable of measuring deposition point by point around the insulator surface, a laboratory contaminant was chosen that had both fluorescent properties under ultra violet (UV) exposure, and good monodispersity. Sold under the trade name Visolite, by Bag House Accessories Co., Kansas City, Mo., the orange dust particles are made of formaldehyde-based resin with a nominal particle diameter of 4 μm. While normally used as part of a bag house leak detection system, the particles have performed well in all phases of the experiment. The size dispersion of these particles was measured, and will be described in Section 3.7.

After some unsuccessful preliminary experiments with fans and small blowers, a fluidized bed approach was finally adopted as the best, though not necessarily most convenient, method of both breaking up the raw agglomerated dust into reasonably monodisperse particles, and injecting them into the system. A sketch of the particle injector is shown in Fig. 3.6. Fluidizing air is forced through a porous, or

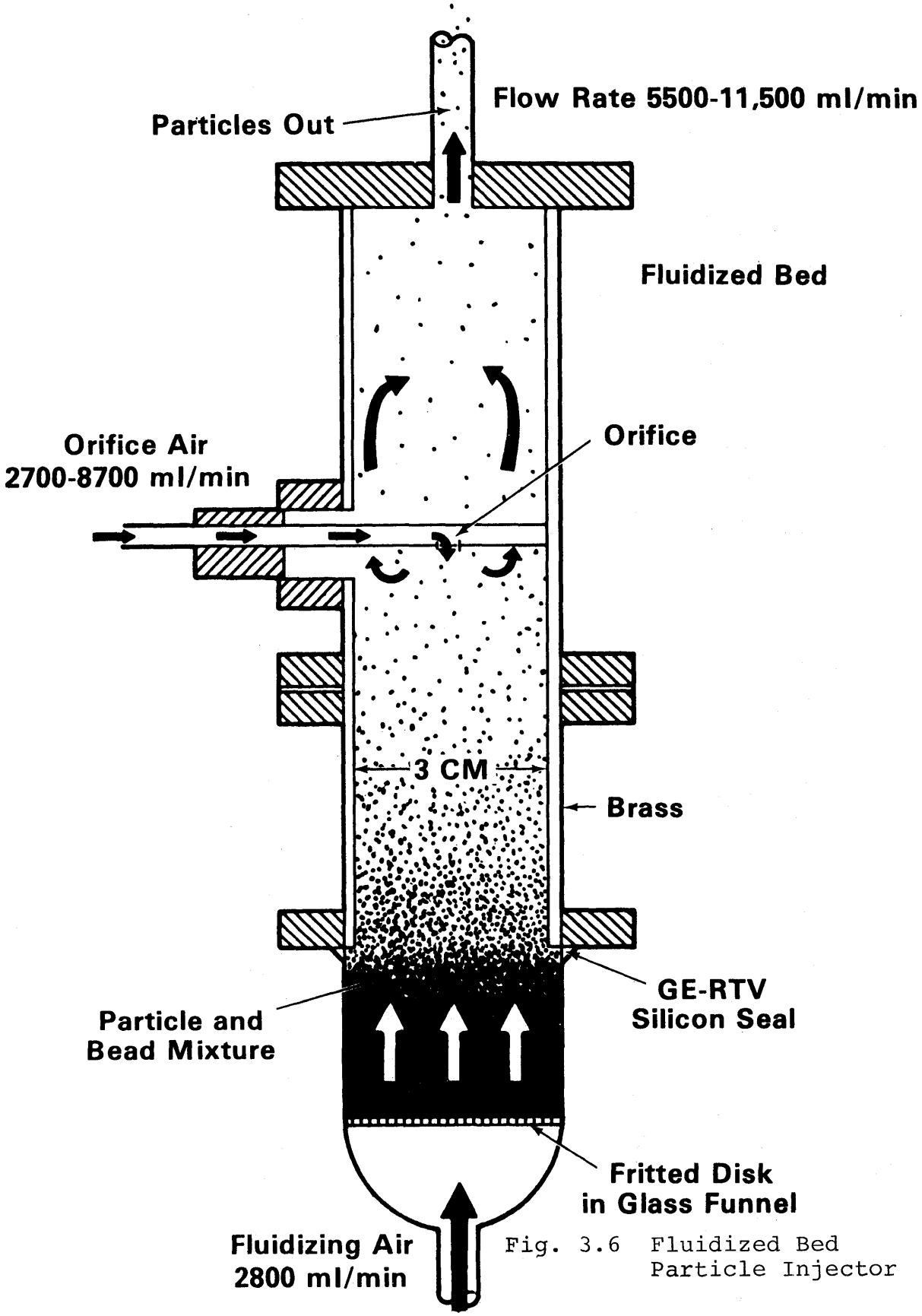

Fig. 3.6 Fluidized Bed Particle Injector

fritted glass disk up into the dust-bead mixture. One piece, premade filtration funnels are commercially available and are convenient to use as a basic container in this application if care is taken not to over pressurize the lower portion of the glass structure. In our case, a No. 36060 Pyrex, 30 ml., medium grit funnel was used.

Following the procedure standard to fluidized bed technology, the raw dust was combined with 500-350 micron (35-45 sieve) glass shot beads in a 50/50 volumetric ratio mixture. The purpose of the beads is to provide a large surface area over which the dust particles may spread. Although the glass beads are too heavy to be lifted by the fluidizing air, the turbulence of the bed knocks them against one another, thereby helping to break up agglomerates of dust particles, and also helping to keep the dust from congealing in the base of the fluidizing column.

In the final design of the particle injector, another stream of air is forced downward out of an upper orifice, thus creating turbulent air flow in the upper portion of the bed. This turbulence further helps to break up particle agglomerates, and helps drift the particles up and out the exit tube. Because of the difficulty of analyzing turbulent flow, this addition to the device was designed by a trial and error method. As will be described in the section on instrumentation, the final design of the particle injector gives good monodispersity and reasonably repeatable particle flow. The

major disadvantages in its design include the filling procedure that must be repeated for every test, because of a lack of sufficient total flow (i.e., the device empties in ten minutes) and a nonuniform flow in time (the flow tapers off as the bed empties). Any future designs for expanded particle injectors should take these two limitations into consideration.

The particles leaving the fluidized bed may, if desired, be fed through a Krypton-85 based radio-active neutralizer whose purpose is to eliminate any natural charge the particles may have accumulated in the injection process. Due to the turbulent and frictional nature of the fluidized bed this naturally acquired frictional charge is not necessarily small.

The neutralizer is a commercial unit made by Thermo Systems, Inc., model 3054. The radio-active material generates plus and minus ion pairs inside the device, from which a naturally charged dust particle attracts whatever ions it requires to neutralize itself. The process is a stochastic one, in which random collisions between charged particles and ions of both signs must be taken into account. A detailed analysis[24] shows that when equilibrium is reached, the number of dust particles with n elementary charges will be given by:

$$\frac{N_n}{N_o} = \exp^{-n^2/2\,\sigma^2} \qquad \text{where} \qquad \sigma = \left[\frac{4\pi\,\varepsilon_o\,R_p\,kT}{e^2}\right]^{1/2} \tag{3.1}$$

where N_n refers to the number of particles per unit volume with n charges, N_o is the total number of particles per unit volume, R_p the average radius of the particles, $\frac{kT}{e}$ is the usual thermal voltage, and e the electronic charge.

This relation, known as Boltzmann's Equilibrium Level, suggests that the 4.0 micron particles used in the experiment will be neutralized to within about twenty elementary charges by the neutralizer.

Other than requiring periodic cleaning with alcohol or soapy water to remove accumulated dust deposits, the device appears to function reliably and consistently if the dust flow is kept below that required for sufficient particle residence time -- in this case an air flow rate of 120 liters per minute.

A design modification was made to the particle injection system midway through the experimental work in an effort to make the source of particles more uniform. The particles exiting from the mouth of the neutralizer represent essentially a point source of injection into the ambient wind. In nature, one can expect contaminant particles to be uniformly distributed by the time they travel from a distant source to the transmission line site. The particles injected in the experiment do disperse somewhat by the time they travel from the neutralizer mouth to the insulator string, spreading out to a cone whose diameter roughly equals the insulator string length. Nevertheless, to simulate a truly homogeneous

distribution of particles, the setup shown in Fig. 3.7, henceforth to be called the "panning" particle source, was constructed. The particles exit from the end of the flexible hose, which is continuously panned up and down, at about .02 m/sec in the plane of injection by a motorized pulley system. The maximum excursions of the injection point exceed the length of the insulator string. Thus a homogeneous particle source, while not exactly achieved, is simulated on the time average by many passes of the hose end.

3.4 Particle Charging

Any model for insulator contamination presumes a knowledge of the charge on the contaminant particles. While the neutralizer allows us to achieve near zero charge, it is obviously desirable to also run tests with particles of known charge. Relying on the natural frictional charge of the particles is not a good idea, because the process by which they so become charged is not well understood. It makes more sense to run the neutral particles through a charging device, with the goal of charging the entering neutral particles, assumed to all have the same diameter, to a single, known value of charge, by way of the field charging mechanism described in Appendix A. As it turns out, several factors limit the single-valuedness to which the particles may be charged, and these will be described shortly.

In the corona triode, pictured in Fig. (3.8a), which

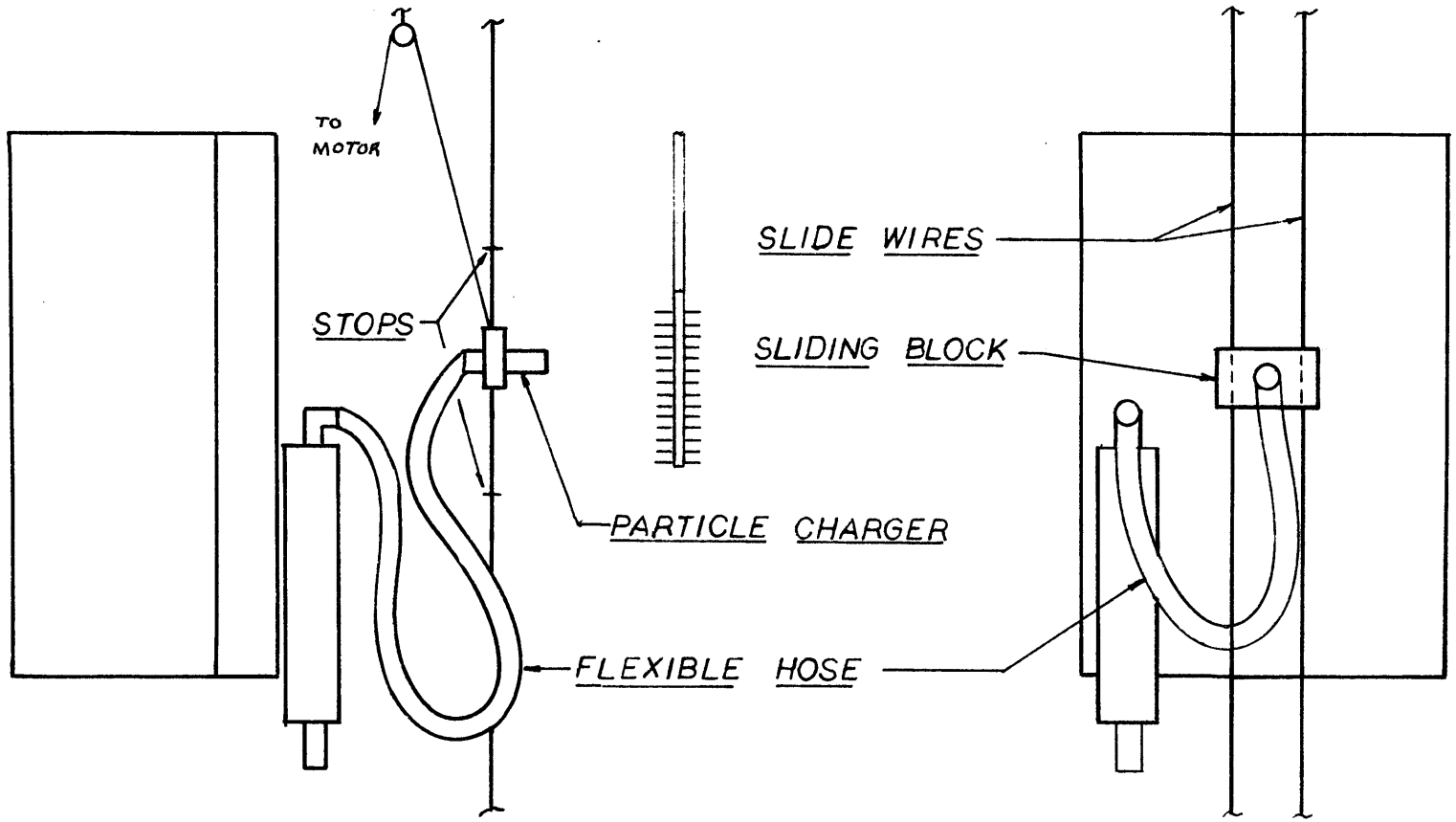

Fig. 3.7 Panning Particle Source

is designed to fit on either the neutralizer mouth or the end of the flexible panning hose, the charging takes place in the second section where the field and space charge may be monitored. The corona pin section generates ions which flow into the charging region, but little or no particle charging is intended to occur in the corona region, even though the neutral particles also pass by the corona pins.

One parameter important to the field charging mechanism, which must be chosen as part of the charger design, is the value of ion space charge density Ne existing in the charging region, where N is the number of density of ions, and e is the electronic charge. (Because the mobility b, in the convention used to describe the particle charging equations, reflects the sign of ion charge, it is sufficient to specify only the magnitude of ion charge density by Ne). The actual value of Ne in the charging region can be monitored by measuring the ion current I_2 flowing into screen 2. The magnitude of the electric field incident on screen 2 may be inferred from the applied voltage V_2 and length L_2; hence I_2, Ne, the screen diameter D, and the electric field are related by:

$$J_2 = \frac{I_2}{\pi \left(\frac{D}{2}\right)^2} = Ne\,|b_{ion}|\,\frac{V_2}{L_2}$$

whence

$$Ne = \frac{I_2/\pi \left(\frac{D}{2}\right)^2}{|b_{ion}|\, V_2/L_2} \qquad (3.2)$$

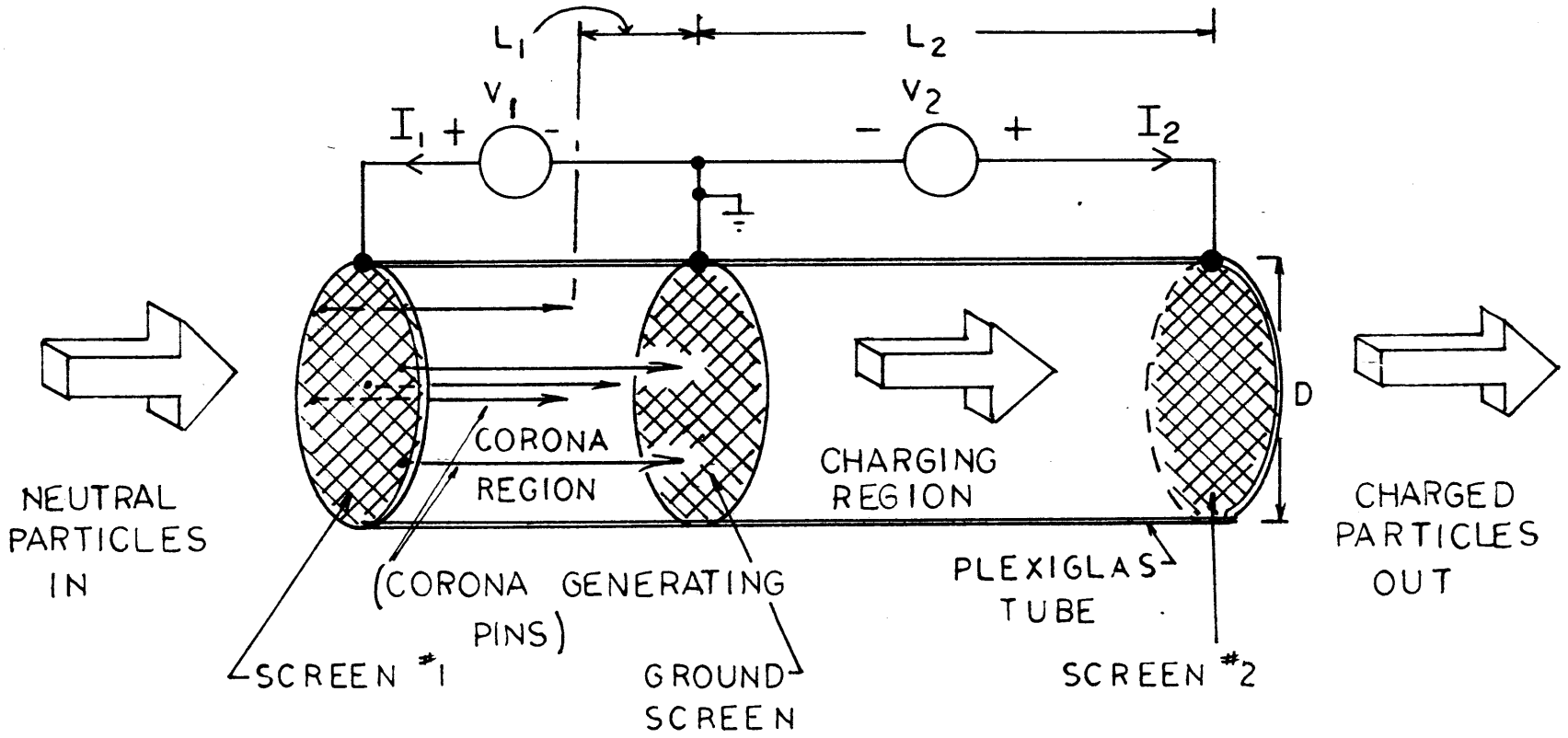

Figure 3.8a Particle Charging Device. Parameters are listed in Table 3.1.

After the appropriate value of Ne is chosen for the charging region, the voltage on the corona pins is adjusted until I_2 reaches the desired value. In all cases the value of Ne is not so large as to appreciably distort the electric field imposed in the charging region.

The original charger design established the charging field in a direction perpendicular to the particle flow, with corona ions generated above and outside the particle stream. Unfortunately, this scheme caused the charged particles to self-precipitate in the charging field. The co-flow configuration of the present design has the advantage of using the back pressure of the fluidized bed to force the particles out of the charging region, but requires that the particles travel for a time through the corona generating region where the fields and space charge are not well known. The first approximation incorporated into the charger is thus to keep the gap between the corona pins and ground screen as small as possible. Hopefully the regions of high field surrounding the pins, and the corona ions emanating from them, will occupy a minor fraction of the cross sectional area, so that most of the particles can travel through the corona section by way of regions of minimal field and space charge. This approach also assumes that the space charge will diffuse outward once in the charging section and be more or less uniform.

The second approximation utilized in the charger design involves the charging dynamics of the particles. Ideally,

the particles should reside in the charging region for many time constants ($4\varepsilon_o/Neb$) to be certain that saturation charge is reached. Unfortunately, the particle flow rate is so fast that in order to obtain a high enough space charge density Ne, for a sufficiently fast charging time, the requirement that the electric field in the charging region be unaffected by the ion charge density is violated. Compounding the problem is the fact that the charging of particles follows a slowly varying hyperbolic, rather than exponential law, so that leaving them in the charging region for a fixed amount of time less than many time constants will lead to a charge that is less than saturation. This situation is illustrated by the graph of Fig. 3.8b, where the residence time indicated is that experienced in the device and leads to roughly half the saturation charge for the particles. Of course, some particles will reside for more or less than the expected amount of time, leading to some spread in the final value of charge, as described earlier. Hence the expected charge on the particles can in practice be only approximately achieved.

The specifications for the particle charger are listed in Table 3.2. Calibration and testing of the charger were hampered by the unavailability of a standardized instrument for measuring particle charge. The mobility analyzer described in Section 3.7 was designed and built as an instrument to measure particle charge -- however, it requires a source of particles of known charge to be accurately tested.

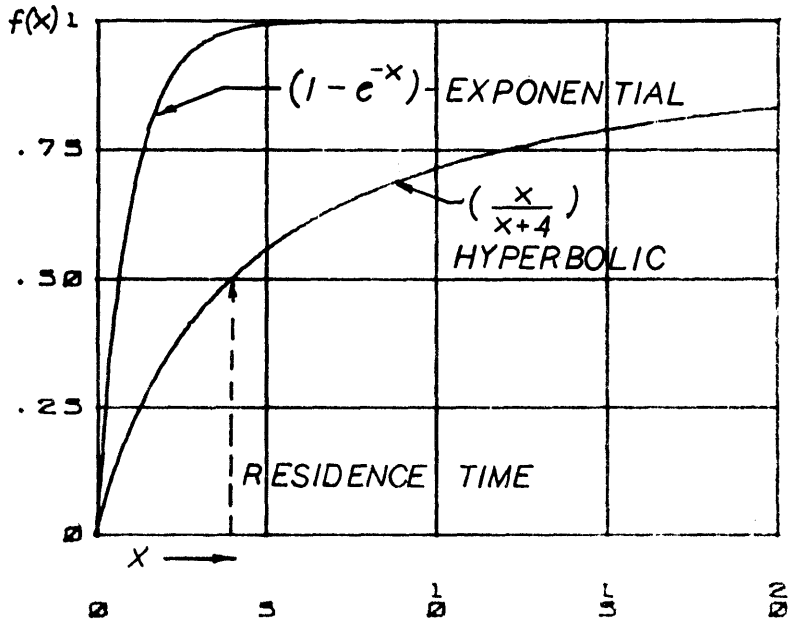

Figure 3.8b Hyperbolic Versus Exponential Particle Charging Functions

Table 3.2

Particle Charger Specifications

Voltage V_1 = 5 - 10 kV; adjust to receive .5 - 1.0 μa corona current at screen 2

Voltage V_2 = 10 kV

Spacing L_1 = approximately .5 cm

Spacing L_2 = 3.4 cm

Diameter D = 2.5 cm

Charging Field = 3×10^5 volts/meter

Maximum Space Charge Perturbation - 2×10^5 volts/meter

Particle Residence Time = .23 second @ air flow rate of 15 cm/sec

Acquired Particle Charge = approx. $2\text{-}4 \times 10^{-16}$ coulomb (for a 4.0 μm particle)

Nevertheless, these two devices, when used concurrently, yield results consistent, within a factor of two or three, with the specifications for which both were designed. This agreement forms the basis on which the value of particle mobility is chosen when analyzing the experimental data.

3.5 Insulator Strings

The trials and tribulations involved in designing the scale model insulator string were many, involving a tradeoff between ease of fabrication and the extent to which the actual insulator string could be physically and electrically modeled. Most insulators in service today, including those used on the Pacific Intertie, are made from glass or porcelain glazed with glass-like materials. As discussed in Chapter 2, the potential distribution over a dc insulator is essentially determined by the surface conducting layer present on glass surfaces, hence for electrical duplication of insulator properties the choice of glass as the working material was obvious. Glass is very difficult to machine, however, and arriving at a glaze-quality surface by mechanical polishing virtually impossible. Careful discussions with personnel at the MIT glass shop and with several professional ceramacists indicated that it might be possible to make glazed ceramic disks by conventional pottery techniques, but any shapes with more complicated geometries were deemed unworthy of the prohibitive expense of both time and money involved. We

therefore settled on a simple disk as the basic insulator shape. Important for our purposes was a uniform coating of glaze, and apparently this is a difficult condition to achieve over the entire surface and edges of a small disk, much less any shape of more complicated structure. As a compromise between the unrealistic expense of obtaining precise, industrial quality glazed disks in the quantity required, and a desire to attempt to make the model insulators from glazed ceramic, a professional potter was engaged to attempt the job. Two months of conscientious effort solved many of the unique problems posed by the task, but yielded glazed disks of Stone Age appearance, totally unsuitable for experimental use. Besides being lumpy and quite non-uniformly glazed many suffered voltage puncture under minimum withstand tests when energized between two electrodes. At the suggestion of the ERDA committee, this approach to the insulator problem was later abandoned as being unworthy of the trouble involved.

Another idea that was tried, and eventually did lead to the final insulator string design, involved using watch glasses of the type normally found in chemical work. Finding a suitable type proved to be somewhat of a problem. It was initially felt important to know the exact chemical composition of the glass, and therefore a large number of quality grade Corning #9985 65 mm dishes were purchased. These dishes, while no doubt excellent for use in chemistry laboratories, were not sufficiently round and symmetrical in shape

for our purposes. Apparently the process by which the pyrex edges are fire polished tends to warp and physically distort the glass.

The "garden variety" watchglasses found at MIT Lab Supply were more evenly shaped, but many had rough-cut edges. The watch glasses used in the final insulator string came from a rather large batch of similar, inferior grade watch glasses purchased from a supplier, from which a small number of physically suitable pieces with reasonably good fire polished edges and symmetrical shape, were selected. One possible drawback in selecting this lesser quality grade of glass is that the material is simply specified "borosilicate". Should any detailed investigation of the insulator surface composition ever be required, some difficulty may be encountered. At present, this situation does not seem to be a problem.

The next step in developing the insulator string was the design of a suitable coupling for attaching the units together. While it may have been simpler to glue together alternate watch glasses and metal post fittings to obtain a single integral string, the goal of the experiment, whereby detailed measurements on each insulator were to be attempted, required a way that each unit could be detached from the string. Designing the coupling proved to be a trial and error process once the basic idea was formulated. The final version is shown in Fig. 3.9. Several types of epoxy glue

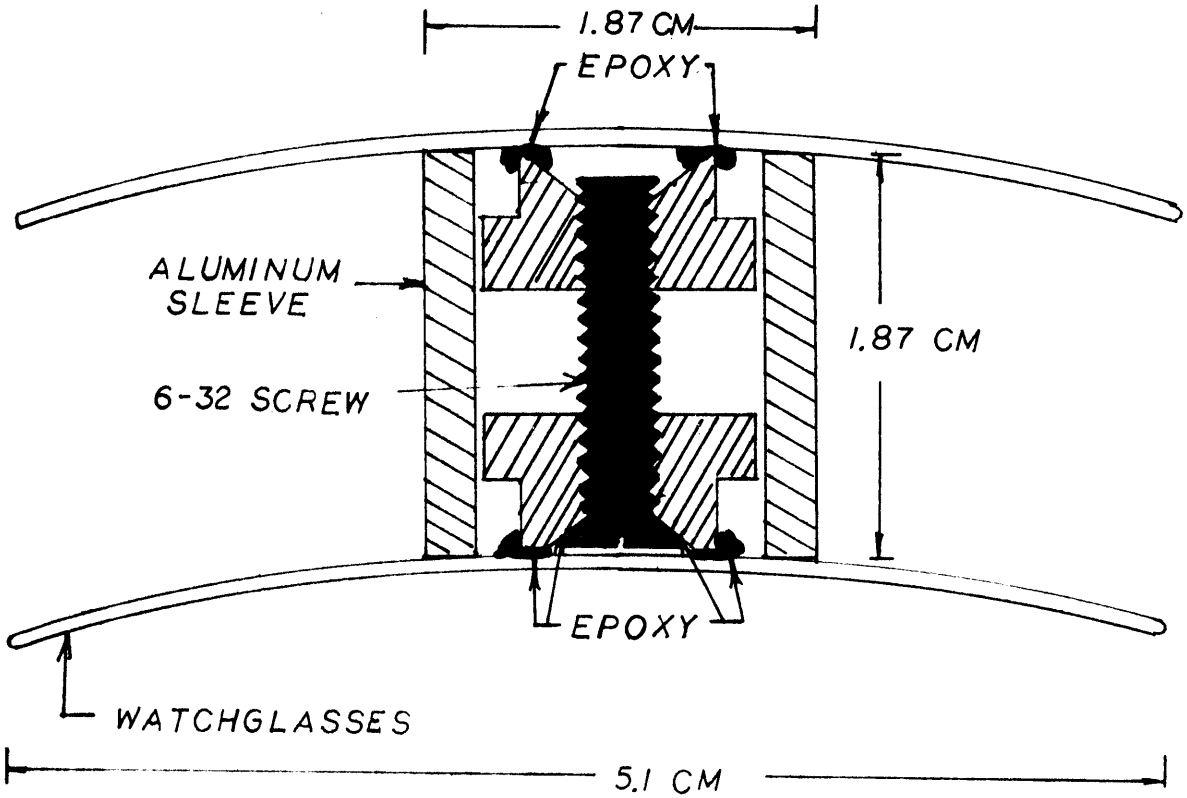

Figure 3.9 Glass Insulator Coupling Design

were tried, and the one found to perform best was Hysol #0151 Epoxi-Patch. The glass-to-metal glued joints can withstand a fair amount of tensile strength if the mating surfaces are first cleaned with alcohol. Of course, joint breakage occurs frequently when the string is in use, and the jig used to assemble the insulators is a handy item for speedy repairs.

The finished glass insulator string is shown in Fig. 3.10. Note the remarkable physical similarity to a real insulator string.

In the early stages of the experiment, an insulator string, shown in Fig. 3.11 was made by alternately gluing plexiglas discs, machined from 1" rod stock, with metal posts. This string was used in initial contamination tests, and provided good qualitative information about the deposition process. These experiments will be described in a later chapter. The plexiglas string was not used for any quantitative measurements.

A limited number of tests on full sized insulators were run --for the most part to examine details of the insulator contamination. The insulators readily available to us were standard 10" and 5" ac units made by the Ohio Brass Co.

3.6 Instrumentation for Measuring Deposited Contaminant

Despite the drawbacks and potential inaccuracies inherent to weighing methods for measuring contamination,a

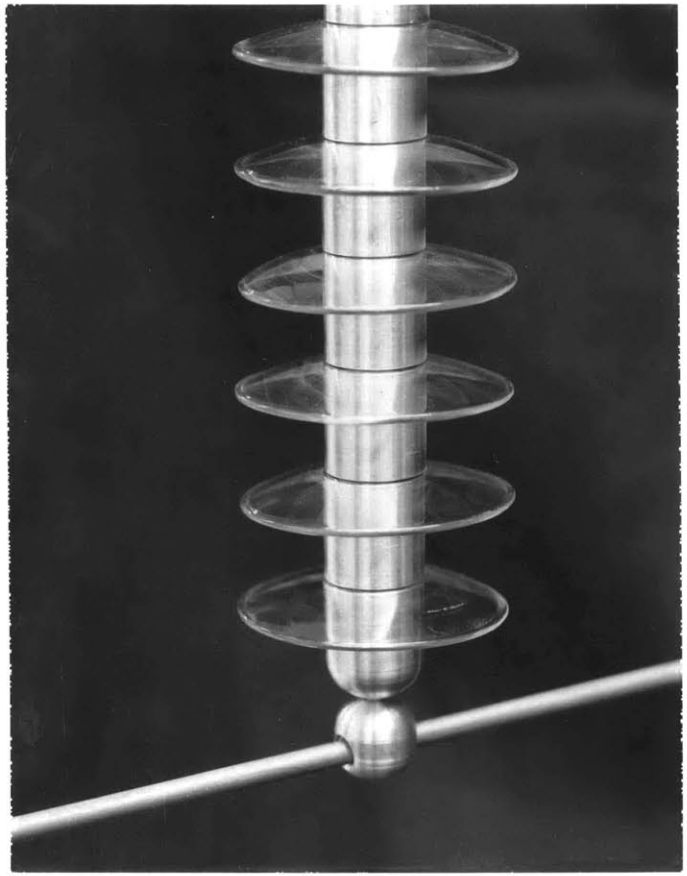

Figure 3.10 Glass Insulator String

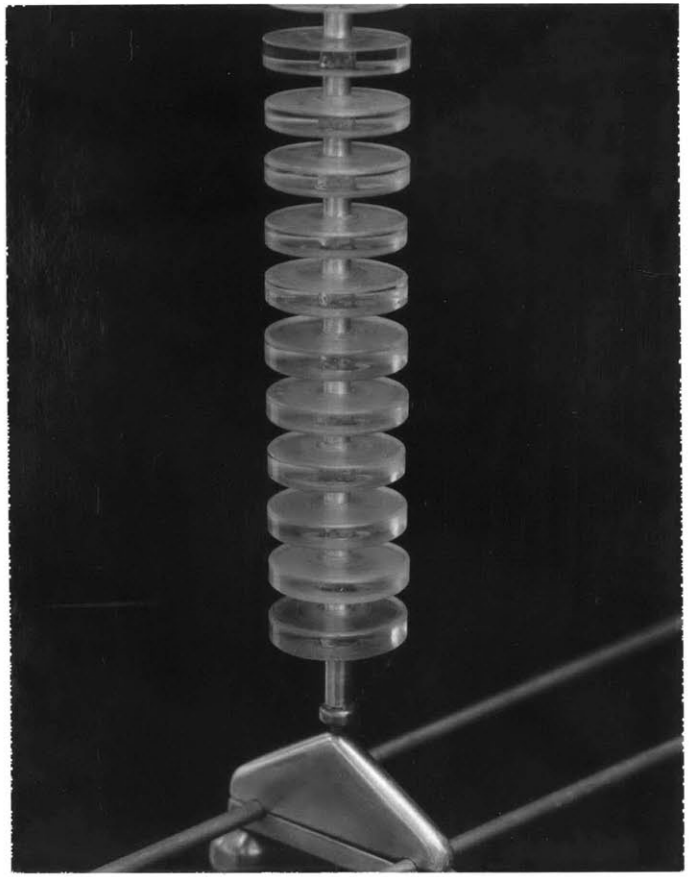

Figure 3.11 Plexiglas Insulator String

technique was developed for using a standard Mettler microgram balance to weigh insulators before and after a given test to measure the net total contamination. A means was thus available to calibrate the optical detector, to be described shortly, and provide a crosscheck on some of the experimental results. With the tare weights of the model insulators falling into the 15 gram range, extreme care was required to detect the contaminant layer weighing in the 500 microgram range. By carefully wiping one surface of the insulator and weighing again, an approximate distribution of contaminant between top and bottom surfaces could be obtained. Experience gained on the Mettler balance also proved invaluable when using other pieces of measuring equipment to be described in later sections.

The majority of quantitative measurements were performed with a specially designed optical detector, shown in Figs. 3.12 and 3.13. The advantage of using the fluorescent Visolite test contaminant becomes obvious when one examines the convenience of using this detector. The sensing element for the detector is a Weston Photronic^{TM} Cell, a device developed in the early 1930's for use in photographic and theatrical lighting work - perhaps one of the first practical uses made of semiconductor materials.[3]

A Pen-Ray^{TM} quartz lamp provides UV light, which passes through a filter to screen out any visible light that may emanate from the bulb. The contaminant on the insulator

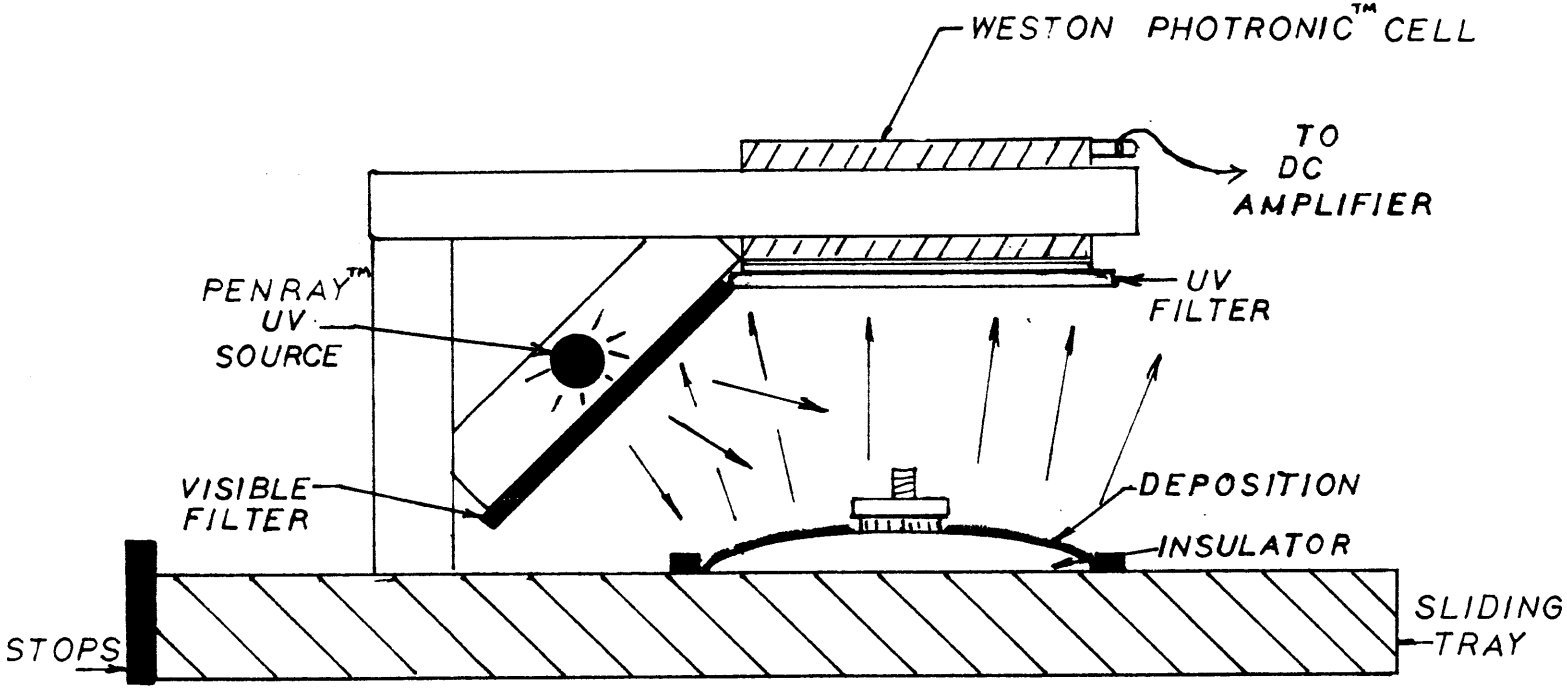

Figure 3.12 Optical Contamination Detector

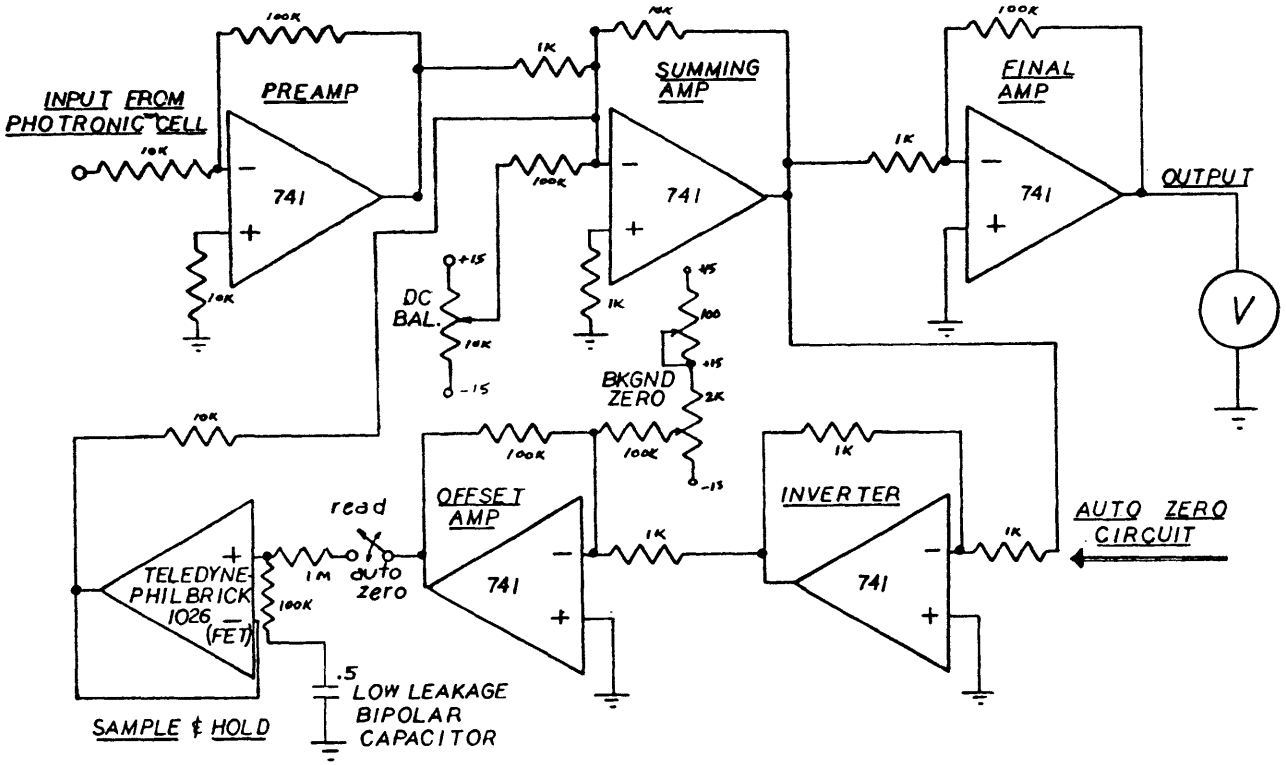

Figure 3.13 DC Amplifier and Automatic Zeroing Circuit for Optical Detector

surface, when exposed to UV, reradiates in the orange. This reradiated light passes through another filter, which screens out any reflected UV, and then strikes the sensor surface. The sensor output is thus proportional to the amount of contaminant on the insulator. Several assumptions are involved here. First, the contaminant layer is presumed light enough to be composed only of single isolated particles that don't overlap or deposit on top of one another, so that masking or shadowing of particles need not be taken into account. Second, the device, by nature, integrates the average contamination over the whole insulator, without regard for variation in dust density over different areas of the surface. Because the UV light shines from one side of the insulator, and deposition patterns are observed to be asymetric in the azimuthal direction, the insulators are always inserted under the sensor with the same orientation and position - usually the more heavily contaminated windward side toward the UV source. Consistent positioning is achieved via secure stops on the sliding tray upon which the insulator rests, and a bracket on the tray to hold the insulator disk in place. Third, no distinction is made between the detector readings obtained from top surface and bottom surface contamination. At present, any loss in UV or visible light intensity suffered when passing through the bulk glass of the insulator is ignored. Very precise measurements of contamination must surely take this minor attenuation into account. The problem

of top surface deposition masking the light from the bottom surface is similarly ignored, though this perturbation on the detector output might be more significant.

Finally, the ideal detection system should give zero output when a clean insulator is scanned. In our case, a background reading is obtained from a clean insulator which is too large to ignore. Although this background reading differs slightly for each individual insulator, an average reading of 3.0 on the detector scale, corresponding to about 200 μgm of deposition, is subtracted from every contamination reading. Again, this modification is only approximate, but for the moderate level of precision currently required by the experiment, it appears entirely sufficient.

The choice of a Weston Photronic Cell as the sensing element appears subject to question, until one examines the pitfalls of using a modern silicon phototransistor device. These devices, by nature of the solid-state properties of silicon, peak in the far red portion of the optical spectrum, and have greatly reduced sensitivity in the orange, where the fluorescence of the Visolite occurs. Secondly, most phototransistors have a limited cone of vision --in fact the one device tried when developing the detector was almost totally insensitive to the level of contamination found in a typical test.

The Photronic Cell, on the other hand, has a large

surface area, almost the size of the insulator itself, over which it is light sensitive. As shown in Fig. 3.14, the spectral response curve conveniently peaks in the orange at 6000 Å. Likewise, it has minimal response at 9000 Å where the visible filter used in the detector has a sub-peak in the infrared.

The output curve of Fig. 3.15 shows the output of the Photronic Cell, when connected to a resistive load of 10 kΩ, to be reasonably linear, if the device is used with low levels of illumination, as it is in the contamination detector.

One disadvantage of the Weston Cell is its tendency to fatigue under prolonged illumination, reducing its output voltage by as much as 3%. Under normal operating procedure, therefore, the insulators were measured first in one order, and then in the reverse order. If a discrepancy resulted, the reading was repeated a third time; a reliable average reading is thus obtained for each insulator.

The calibration curve for the detection device, shown in Fig. 3.16, was obtained using the Mettler balance. The lower points that are out of line are the ones most subject to weighing error because of the small level of contaminant involved. In fact these points appear to be "out of line" also when compared to adjacent readings on the insulator string, and hence may be discounted as weighing errors. Note the horizontal scale is in arbitrary units, determined by the numbers printed on the meter face used for the dc amplifier

Figure 3.14 Approximate Spectral Response Curves of the Various Optical Components

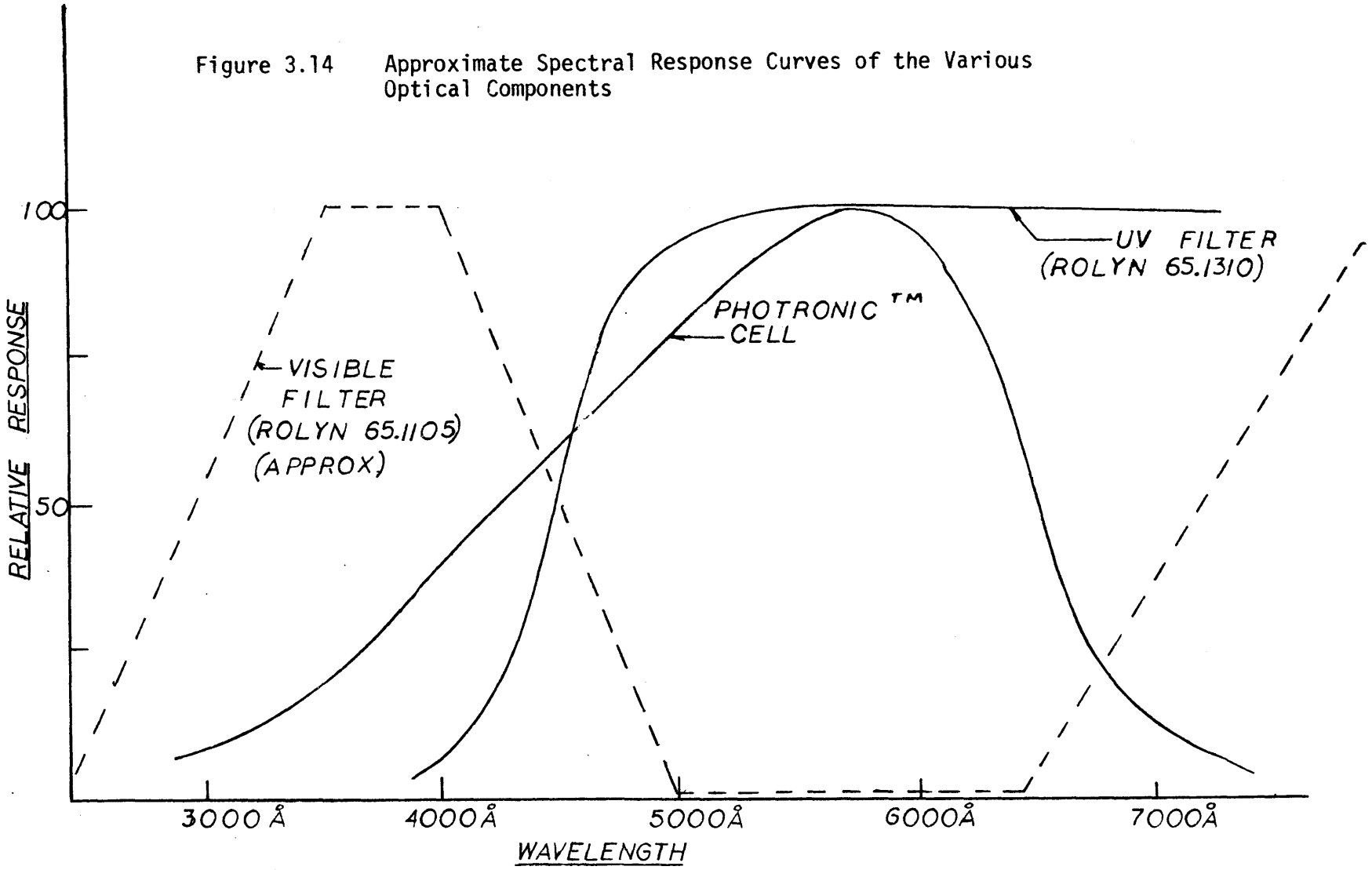

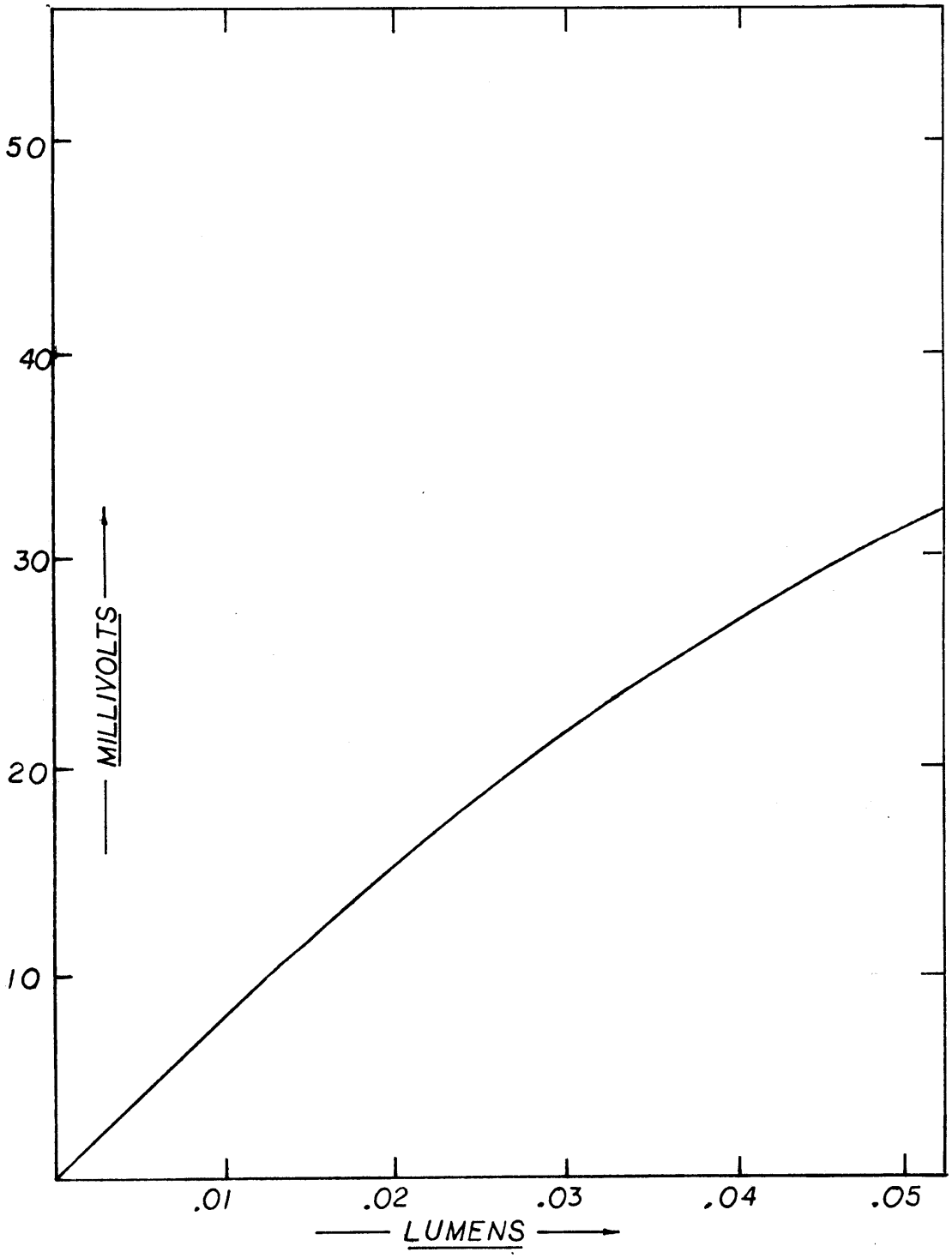

Figure 3.15 Low end of output curve of Weston Photronic(TM) cell terminated in 10 kΩ, using 3000°K tungsten source. Obtained from technical data for the photronic cell, Western Electrical Instrument Corp.

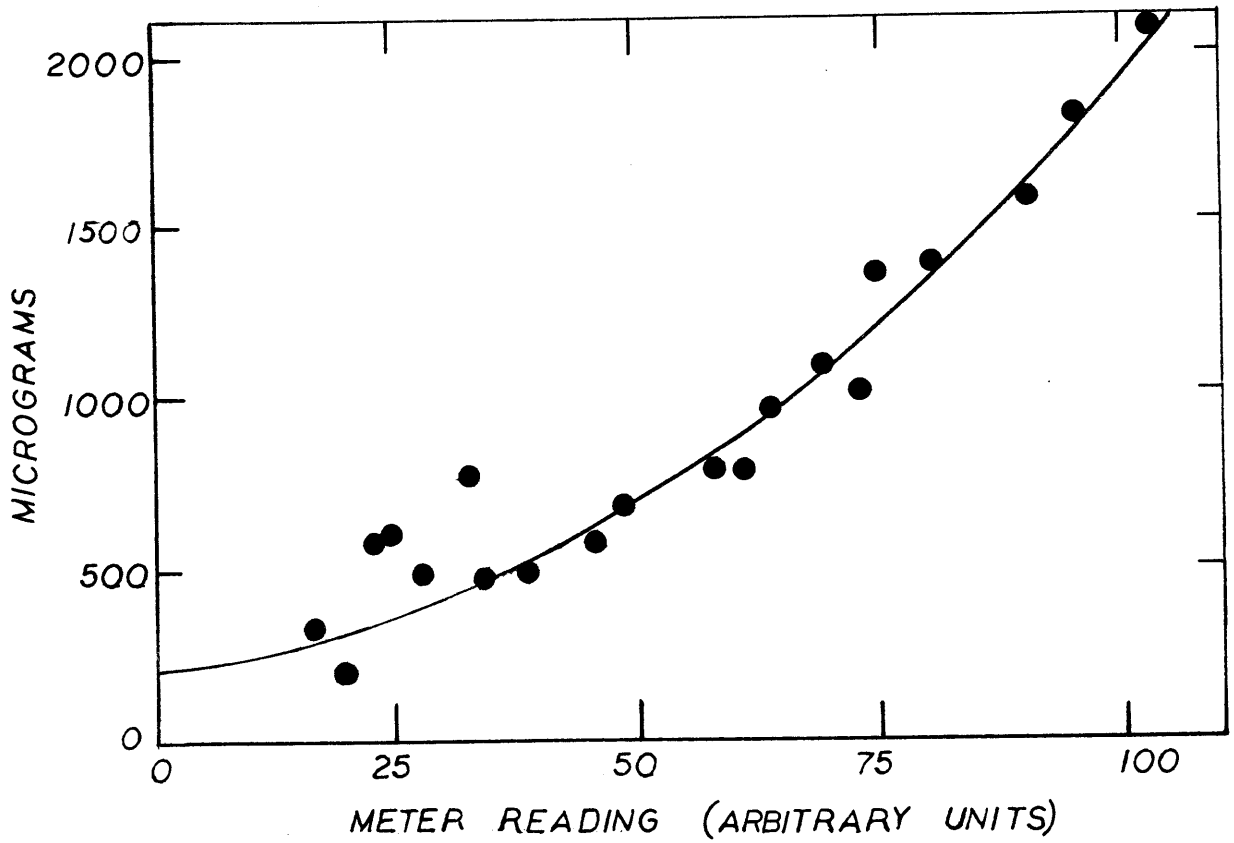

Figure 3.16 Optical Detector Calibration Curve. Micrograms of Deposition vs. Reading on Output Meter

readout. Evident in the calibration curve is an apparent threshold for detectable deposition of about 200 micrograms, below which the background level of the glass insulator itself dominates the measured signal. No attempt has been made to separate the signal from the background noise in this low region of the calibration curve.

3.7 Mass Loading Measurements

The term "mass loading" is borrowed from aerosol technology, and refers to the ambient mass density of particles in kilograms per cubic meter. To measure this mass density in the test chamber, an inertial impactor, depicted in Fig. 3.17, was used.

This device, made by Anderson, Inc., samples the air at 1 CFM, and sorts the particles entering it, according to size, onto one of eight filter paper discs inserted beforehand. The accumulation on each of the eight discs represents particles of a different diameter, as shown in Table 3.3. The accumulated mass increases, although quite small, can be detected on the Mettler microgram balance. The particle dispersion, or relative distribution of particles according to size, can be inferred from these mass increases if the particles are all of the same material, and thus have the same density. In the test chamber, the dispersion curve was found to consistently peak at about 4 microns, and be reasonably monodisperse, regardless of the absolute amount of mass

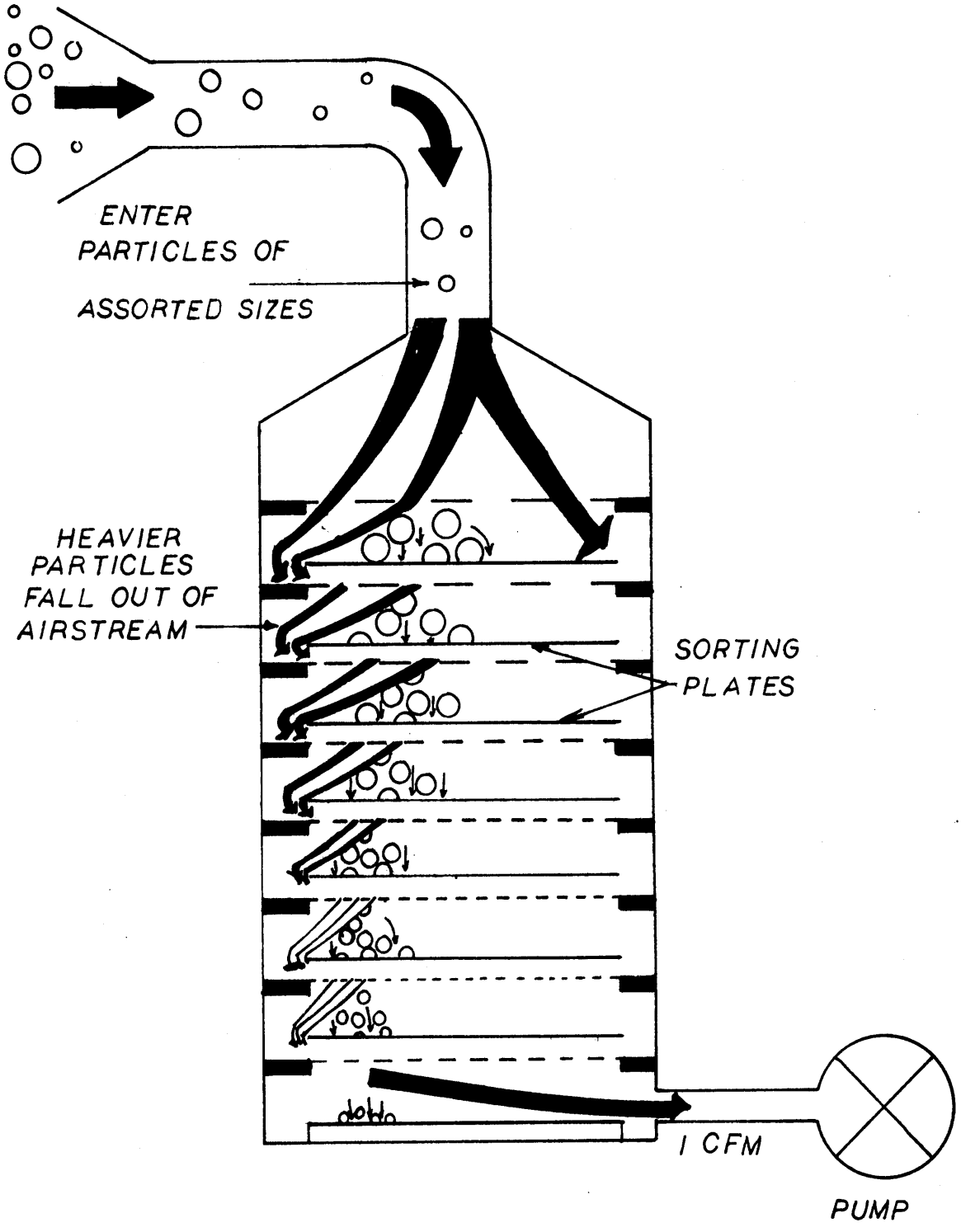

Figure 3.17 Depiction of Anderson Inertial Particle Sampler

Table 3.3

Anderson, Inc. Inertial Particle Sampler Calibration Values

Plate No.	Average Diameter of Collected Particles ("Cut Diameter")
0	11. micron
1	7.0 micron
2	4.7 micron
3	3.3 micron
4	2.1 micron
5	1.1 micron
6	.65 micron
7	.43 micron
F	any remaining smaller particles

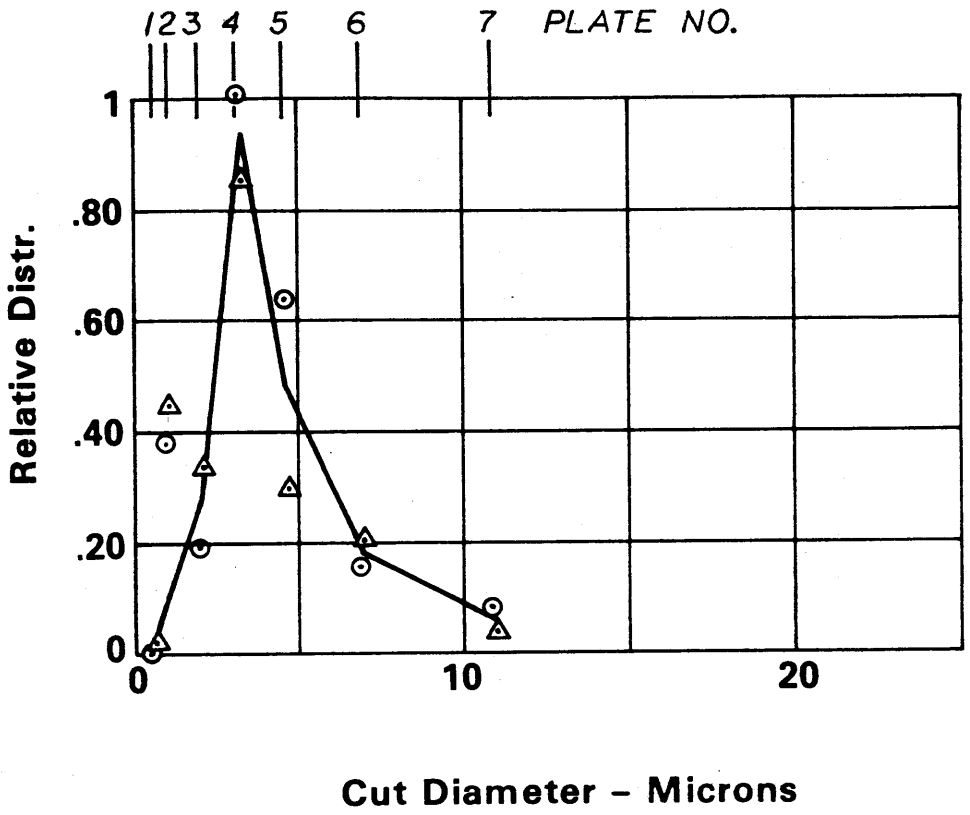

Fig. 3.18 Particle Dispersion Curve Measured in Chamber for Two Separate Test Runs

loading. A typical dispersion curve is shown in Fig. 3.18. Because of the tedious weighing and assembly procedure required for each measuring run made with the inertial impactor and because the dispersion was found to be relatively consistent, it was deemed beneficial to develop some simpler way of measuring the total mass flow during a contamination test, and to assume the dispersion to be the same for every test. A hole approximately three inches in diameter was therefore cut in the filter cloth of the downstream plenum box, and a frame fitted around it to accept a filter paper disc, as shown in Fig. 3.19. By measuring the net mass increase due to collected particles of this one disc, an estimate of the mass loading for a given test can be derived if the net mass increase is assumed proportional to a mass flow-collection time product.

In simultaneous measurements made with both the Anderson sampler and the filter paper sampling disc, the mass increase on plates 2 and 3 of the Anderson was compared to the mass increase of the sampling disc. Plates 2 and 3 were selected because they represent the peak accumulation of particles, as seen on the dispersion curve, Fig. 3.18. The results of these simultaneous measurements are shown in Table 3.4, from which the ratio $\alpha = \frac{\text{mass on sampling disc}}{\text{sum of mass - plates 2 \& 3}}$ is determined to be about $\alpha = .22$. From this value of α, and knowledge of the 1 CFM air sampling rate of the Anderson, the value of mass loading ρ kg/m^3 can be inferred in a given test

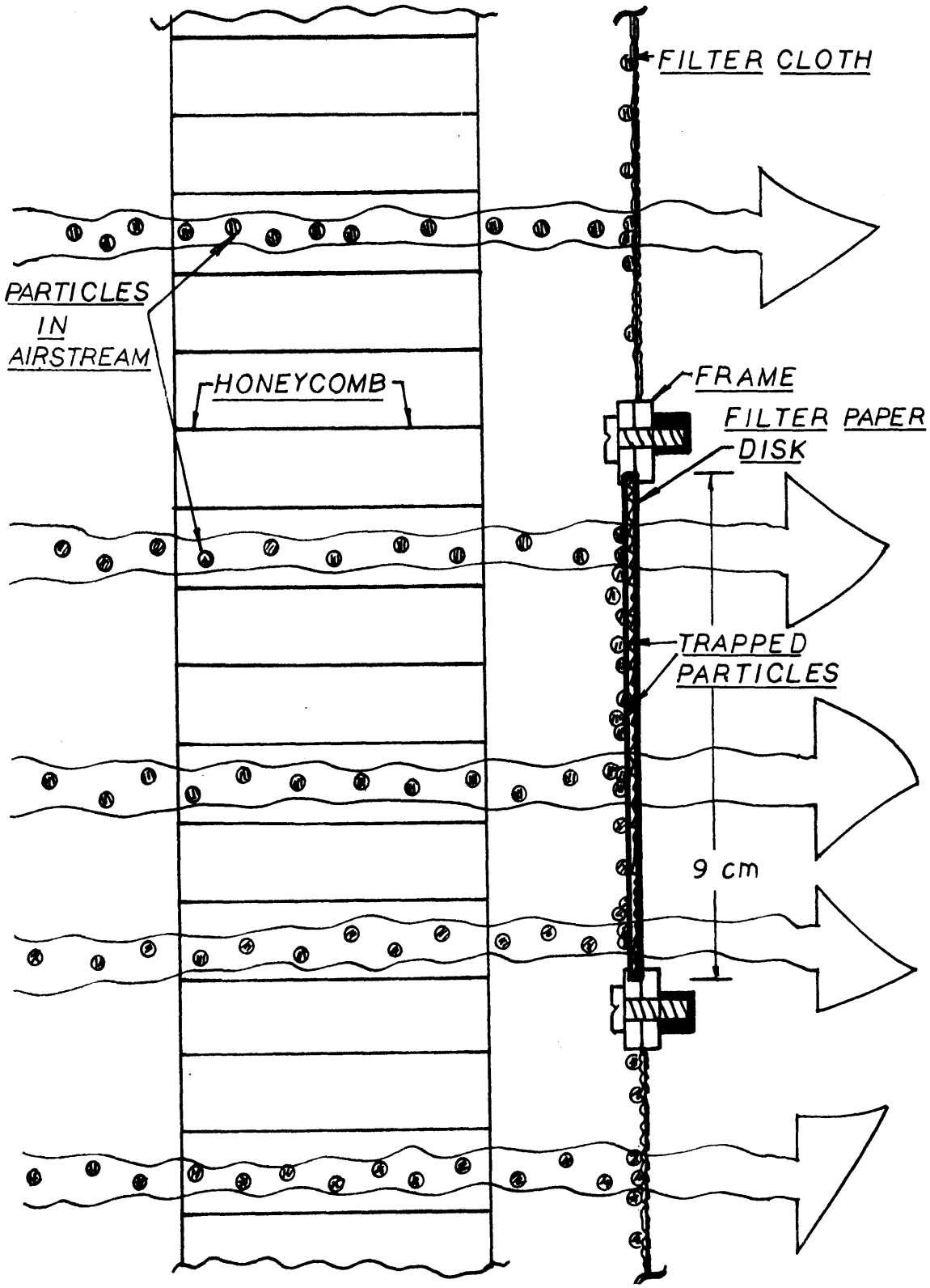

Figure 3.19 System for Measuring Mass Flow

Table 3.4

Calibration of Mass Flow Measuring System

Trial	Anderson Measurements Plate	Δ-μgm	Calibration Mass μgm	α*	β*
1	2	1967	1100	.26	.47
	3	2345			
2	2	1455	430	.15	.29
	3	1485			
3	2	1710	650	.19	.40
	3	1645			
4	2	787	515	.30	.56
	3	920			
Average	2	1480	674	.22	.42
	3	1600			

*α and β are the ratios of calibration mass to Anderson measurements.

α is based on sum of plates 2 and 3; β is based on plate 3 alone.

from the mass increase of the sampling disc, henceforth to be called the "calibration mass".

It should be explained here that during any particular test, the fluidized bed is allowed to run to depletion. Its output is not steady in time, but rather tapers off continuously as the bed empties. The meaningful measurable quantity important to the contamination theory is actually the total mass flow averaged over the run time of the experiment. The concept of an average mass flow-collection time product:

$$\overline{\rho T} = \int_0^T \rho \, dt \tag{3.3}$$

is much more useful in examining the results of contamination experiments than a simple value for the mass loading ρ. The convenience of considering $\overline{\rho T}$ rather than ρ is made evident in the theoretical analysis of Chapter 5, but at this point one should note that the "calibration mass" really reflects the value of $\overline{\rho T}$ for a given test run.

In practice, all $\overline{\rho T}$ measurements made in the test chamber are normalized to a standard calibration mass of 500 μgm.

In an alternate method for measuring mass flow, the sampling disc may be scanned before and after the test run in the UV detector developed for insulator contamination measurements. Although the background fluorescence of the filter paper material is quite high -- typically twice the net

deposition signal -- it is also very consistent and stable. Hence it may be subtracted from the UV reading to provide a figure proportional to the total mass flow of the test. Calibration shows a net UV reading of 82 (arbitrary detector scale units) to be equivalent to a 500 microgram deposition on the sampling disc, and all tests may again be conveniently normalized to this figure. The background reading of just the filter paper alone is usually 32 (arbitrary detector scale units).

3.8 Particle Mobility Analyzer

When the inertia of particles is ignored, as it may be for the particle sizes considered here in both the real and model systems, the particle velocity relative to the air under the influence of an electric field depends on both the particle diameter, and acquired charge. This dependence was simply derived in Chapter 2:

$$\bar{v} = \left[\frac{q}{6\pi\eta R_p}\right] \bar{E} \triangleq b\bar{E} \qquad (3.4)$$

The expression in brackets is defined as the particle's mobility "b" -- that is, the particle will move with velocity $b\bar{E}$ relative to the air under the influence of the electric field. Note that the sign of the charge q is the same as the sign of the mobility.

Knowledge of this mobility is important in

interpreting the results of contamination tests, as well as in predicting contamination from theoretical models of the deposition process. Note that particles with various radii and charge which happen to fall in the same mobility ratio q/R_p will behave similarly in the vicinity of the insulator, so that knowledge of the mobility is actually more important than knowledge of either q or R_p.

An apparatus designed to measure the mobility of particles in the test chamber is shown in Figs. 3.20 and 3.21. A laminar jet of air and incoming particles is established down the center of the channel. With no voltage applied to the side plates, the particles drift undeflected down the channel and are collected in the downstream filter. When voltage is applied to the plates, the electric field causes particle motion perpendicular to the channel at a velocity proportional to the particle mobility. The channel flow is not fully developed, and for our purposes, the assumption of undeveloped slug flow will yield mobility measurements within a factor of two. Knowledge of where the particle hits, as well as average channel flow velocity and perpendicular electric field thus lead to a mobility measurement. The inner walls of the electrodes are lined with removable segments of black paper which may be weighed, visually observed, or placed under the UV detector, to determine the distribution of deposited particles, and hence the distribution of particle mobilities. Simple calculation yields, for the mobility measurement:

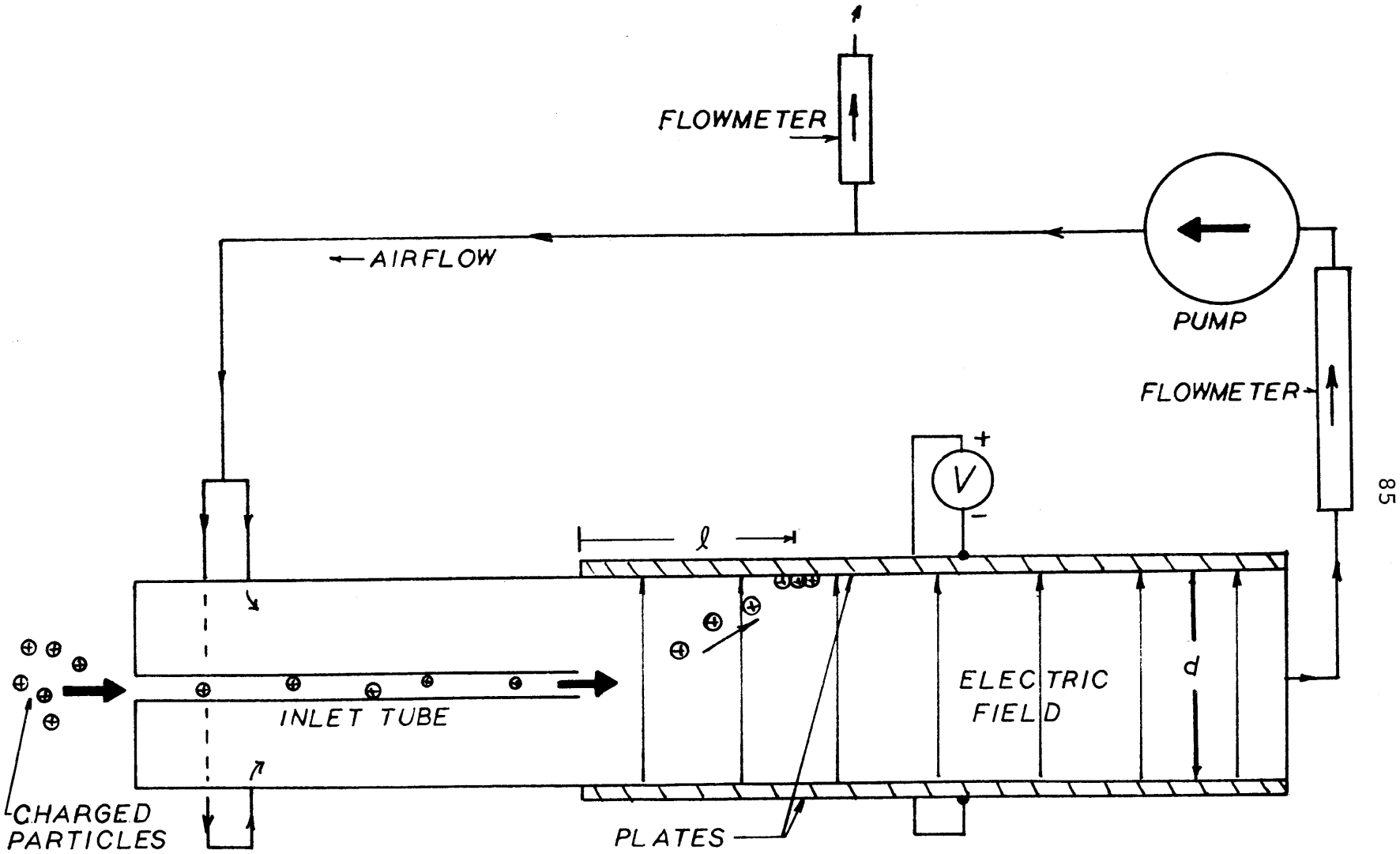

Figure 3.20 Particle Mobility Analyzer Scheme

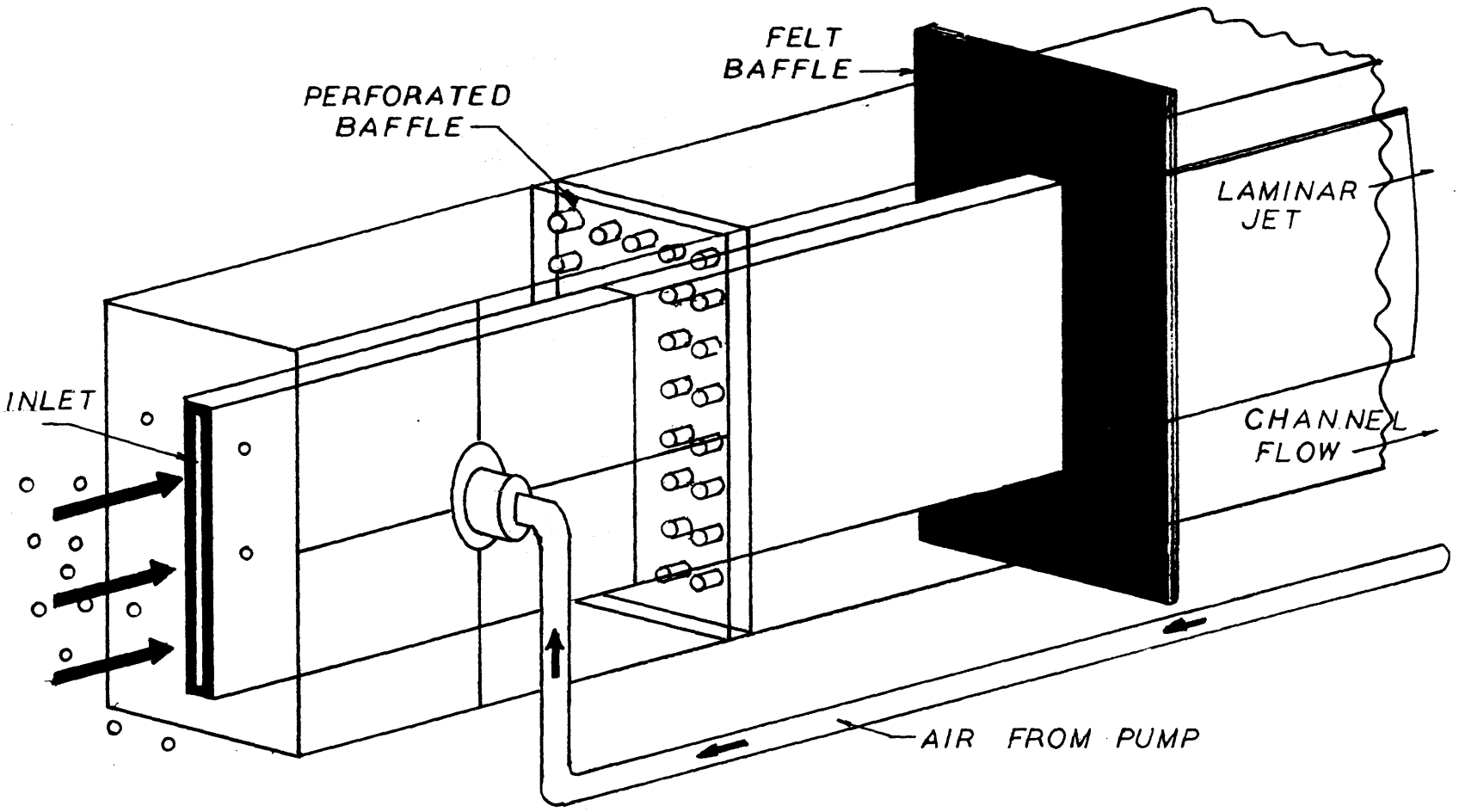

Figure 3.21 Details of Mobility Analyzer Inlet Section

$$b = \frac{Ud^2}{2V\ell} \tag{3.5}$$

where U = flow velocity in the center of the channel, d = channel width, V = applied plate voltage, and ℓ = length down channel at which particle hits the electrode wall.

In practice, the channel flow velocity is measured by sending smoke down the channel and measuring its transit time. A typical applied voltage for the plates, for the range of particle mobilities expected in the chamber, is about 1-4 kV, and the channel flow velocity, which is adjustable, falls in the range of .1 meter per second.

Figure 3.22 shows a plot of the mobility measurement equation for various values of channel voltage. The plotted data points were taken with the particle charging device providing the incoming particles. The parameters for the charger were those listed in Table 3.2. The points on the plot represent the location of the peak of deposition on the channel wall. The deposition signal is typically too weak to provide meaningful measurements of the mobility distribution.

Figure 3.22 suggests a value of 6×10^{-7} m^2/v-sec for the particle mobility. To stay within the bounds of reasonable engineering accuracy, the measured value of mobility will be taken as 5×10^{-7} m^2/v-sec throughout the course of this work.

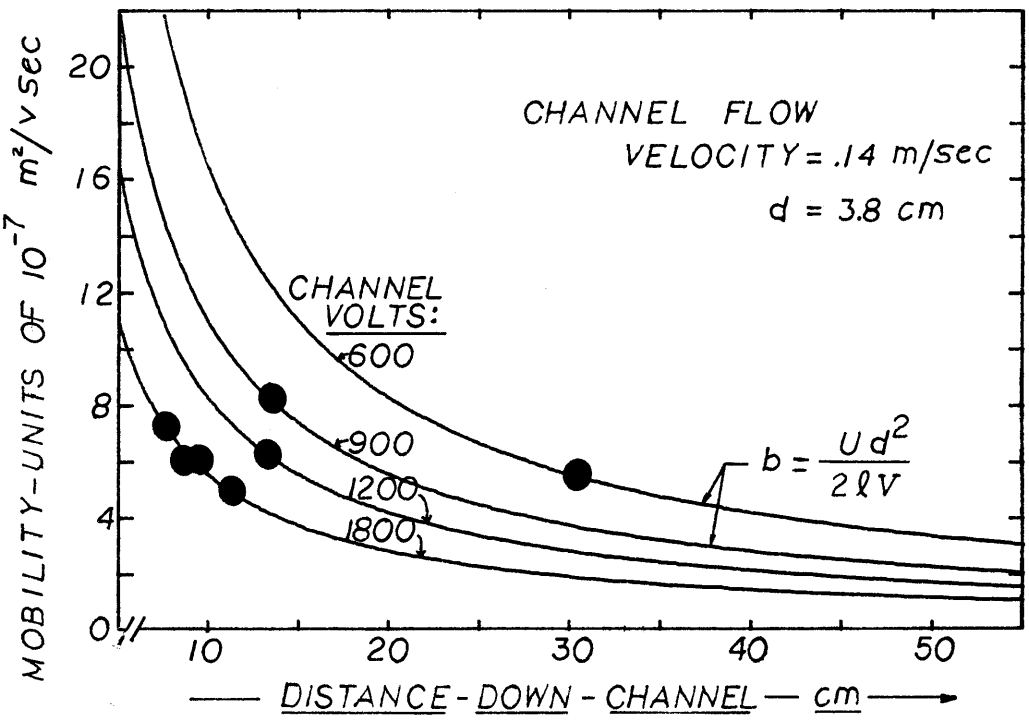

Fig. 3.22 Mobility Measurement Equation and Several Data Points

CHAPTER 4

FUNDAMENTALS OF THE CONTAMINATION PROCESS

4.1 Introduction

In this chapter, the fundamental physical laws cited in Chapter 2 are used to develop the basic principles and definitions governing particle deposition on insulator surfaces. The analysis, aimed at explaining observed experimental results, focuses on the values of particle mobility, wind velocity, applied line voltage, etc., found in the test chamber. As such, the analysis tends to accentuate the regime of lower wind velocities characteristic of the experimental setup, although the analysis is correct for higher wind velocity to particle mobility ratios. The experiments described in the next chapter support a simplified contamination model, applicable for engineering purposes to a wide range of wind velocities.

4.2 Qualitative Experimental Results

Before the equations of particle contamination are developed in detail, it is appropriate to describe qualitatively the general features of the experimental results. They can be divided into two basic categories. The first deals with deposition as a function of relative position on the insulator string and line conductor as a whole, and shall be named the "macroscopic" deposition. The second category, to be discussed shortly, concerns the characteristics of the

deposition pattern on each single (unit) insulator, and will be called the "microscopic" deposition.

The effect of using charged particles of one sign manifests itself most significantly in the differences between the macroscopic deposition patterns when the polarity of the line conductor is changed. Two such tests using the plexiglas insulator string and panning particle source are shown in Figs. 4.1 and 4.2. These observations were obtained in tests below the threshold of corona, where particle charging dynamics are absent.

Because the charged particles shown in Figs. 4.1 and 4.2 are negative, the observed areas of heaviest contamination, as shown by white regions on the string, correspond to areas of negative particle deposition. The results of these two tests suggest a general conclusion, applicable to all charged particles, that is confirmed by the more exact analysis to follow in subsequent sections: Of the particles that do deposit in some way, most appear on the line conductor and lower insulator units when the particles have the opposite polarity of the line conductor, and on the ground post and upper insulators when the particles have the same polarity as the line conductor. In these experiments all regions of the insulator string are essentially accessed uniformly by particle laden wind, hence one might conclude from these results that charged particles carried toward the insulator by the wind are deflected by the electric field toward the upper

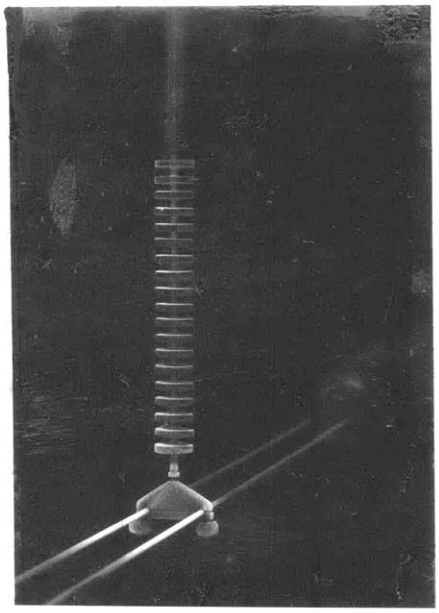

Fig. 4.1 Contamination Test with Plexiglas String. Attracted Particles (Negative particles and Positive conductor). White regions denote deposition.

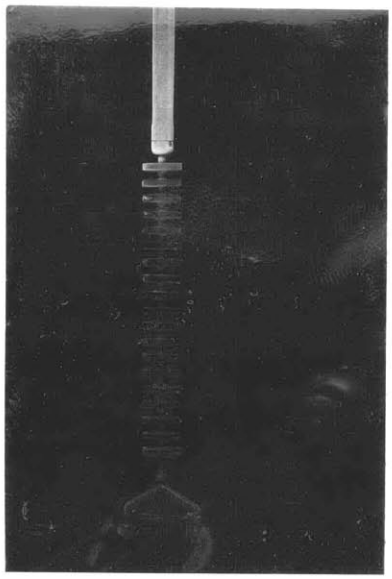

Fig. 4.2 Contamination Test with Plexiglas String. Repelled Particles (Negative particles and Negative conductor). White regions denote deposition.

or lower ends of the string, depending on the sign of the particle charge. The trajectory analysis of Section 4.5 shows that large scale deflection of particles is highly improbable for the size of particles studied here; nevertheless the preference of particles of a given sign for one end only of the insulator string is consistently observed in the experiment. Other investigators[22] have also observed the phenomenon, so it cannot be attributed to a quirk of the experimental apparatus described here. An examination of the phenomenon, which will henceforth be called particle "segregation" (to avoid confusion with the notion of particle deflection), is presented in Chapter 5, where it is demonstrated in detail that large scale particle deflections are indeed unlikely for 4 micron particles. The observed segregation of particles is shown to be caused by processes occurring on or in transition to the microscale. For now, the issue is simply presented as part of the overall qualitative description of the experimental results.

An important observation that accompanies the segregation phenomenon is the preference for deposition on either the top surface or bottom surface of a given contaminated insulator unit, depending on whether the unit is located near the lower end or upper end of the string, respectively. The general nature of the microprecipitation process is embodied in this observation. If one were to make a qualitative statement about the electric field between two insulators on the

string, included would be the fact that the field lines, for a positive conductor, generally extend upward, from lower insulator to upper. One would thus expect negative particles to follow field lines back and land on the top surfaces of the insulators. Similarly, positive particles would deposit on the bottom surfaces of the insulators. Hence, given that, for a positively energized conductor, the positive and negative particles are observed to segregate to the upper and lower ends of the insulator string, respectively, one expects any contamination occurring at the upper end of the string to appear only on bottom insulator surfaces. Of course, for any such bottom surface deposition to occur, positive particles would have to be present. Similarly, any contamination of the lower end of the string should only be found on top insulator surfaces. Such a situation is in fact always observed in the test chamber. A little thought will predict the same general results for particles encountering a negatively charged string; namely, deposition near the lower end of the string occurs on top surfaces only, and deposition at the upper end of the string occurs on bottom surfaces. Again, this generalization to include negative conductors is consistent with what is observed experimentally.

The fact that surface deposition preference and particle segregation act together to produce the same prediction for contamination regardless of conductor polarity suggests that it may be more convenient to speak of charged particles

as "attracted" and "repelled", rather than positive and negative. Hence in other sections of this work these terms are often adopted. More specifically, a particle is "attracted" if it has a sign opposite that of the line conductor (i.e. attracted to the line conductor), and a particle is "repelled" if it has the same sign as the line conductor.

Several other interesting effects, summarized in Fig. 4.3, further highlight the small-scale microscopic deposition patterns. These will be simply stated here, and analyzed in greater detail in subsequent sections. The appearance of clean bands of essentially no deposition around the center of the metal pin caps between the insulators is shown in Fig. 4.3. While a clean band always appears on any post acquiring contaminant, the relative amount of dust on the post just above and below the clean band varies, depending on the sign of the incident charged particles. When the particles have the same sign as the line conductor (repelled particles), the lower portion of the post below the clean zone is contaminated, and vice versa for particles of opposite sign (attracted particles).

Another effect of interest is the demarcation of regions of deposition on insulator surfaces by very sharp clean rings just adjacent to the metal pin caps, also shown in Fig. 4.3. These rings appear on both top and bottom contaminated surfaces, and have been noted consistently in all tests. Their appearance is explained quite adequately by the

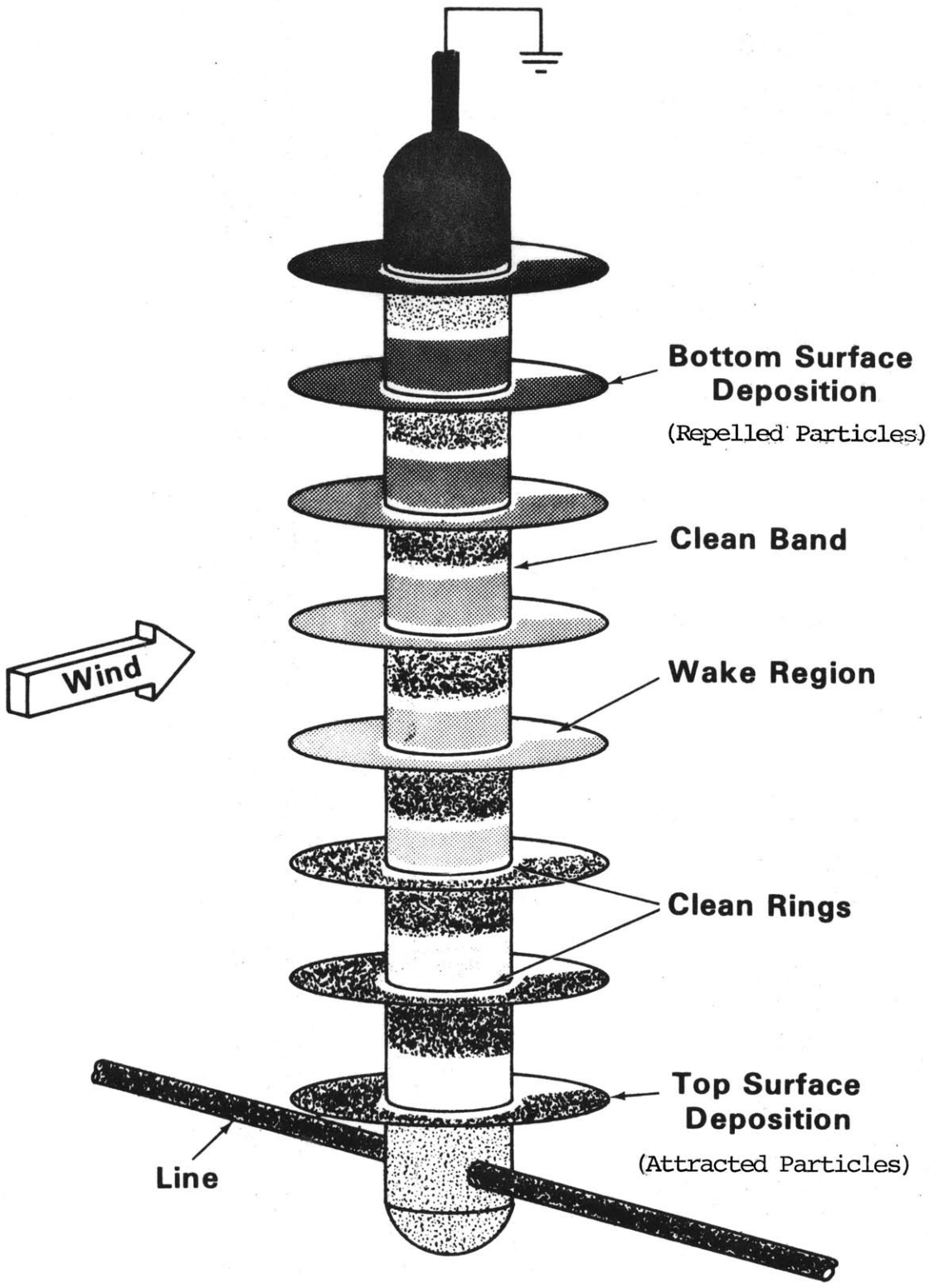

Fig. 4.3 Summary of Microscopic Deposition Patterns

micro-deposition model of Section 4.8, and seems to be a general consequence of using suspension-type insulators under dc conditions.

Finally, the deposition patterns on the insulators are in general azimuthally symmetric, except for the appearance of a diffuse, clean area of no deposition, always located on the leeward side of the insulator surface, as shown in Fig. 4.3. This clean strip has been named the "wake" region because of its suspected relationship to the screening of the insulator surface from the wind by the metal pin cap. The degree to which this wake extends from the pin cap outward, toward the edge of the insulator, seems to vary, and depends on the degree of turbulence present in the vicinity of the insulator, as estimated by visually observing the injected contaminant dust. The more turbulent the flow, the less prevalent is the wake region. Once again, the existence of the wake region, and its general shape are explained by the micro-deposition model of Section 4.8.

As a control check on the experimental technique, and to confirm the notion that insulators energized to ac voltages suffer none of the contaminant precipitation problems that beset their dc counterparts, several quantitative tests with precharged particles and ac line voltages were run. As expected, the insulators suffered no measurable contamination.

4.3 Fundamentals of Particle Migration and Deposition

Before the deposition process on actual insulators can be examined, some very general theorems and definitions concerning the migration of charged particles must be introduced. The following discussions assume the charge on a given particle, and hence its mobility, to be constant--as would be the case in the sub-corona regime. In Chapter 2, the motion of a particle was shown to be, for the inertialess approximation

$$\frac{d\bar{x}}{dt} = \bar{v} + \left[\frac{q}{6\pi\eta R_p}\right] \bar{E} \qquad (4.1)$$

or

$$\bar{v}_p = \bar{v} + b\,\bar{E}$$

where once again, $\bar{v}_p$ = particle velocity in lab frame, $\bar{v}$ = local wind velocity, and b, the particle mobility, reflects the sign of the particle charge*. The Equation (4.1) defines the "force line", which describes the velocity of a particle at a given point in space. If $\bar{v}$ and $\bar{E}$ are not time varying, the force line may be integrated over time to give the trajectory of the particle, or "particle line". If $\bar{v}$ and $\bar{E}$ are functions of time, the particle at each instant may find itself in a new set of force lines given by the

---

*Having b reflect the sign of the particle charge denotes a usage not standard in the literature, but quite convenient here for developing the equations of particle migration.

instantaneous values of $\bar{v}$ and $\bar{E}$, hence the force lines and particle lines are not equivalent in this case. Such a time varying situation would be typical in very turbulent wind flow, or in a pulsed or ac electric field where the fluctuations in $\bar{v}$ or $\bar{E}$ occur over a time comparable to or shorter than the transit time of the particle along its trajectory. Let us first consider the case of time invariant $\bar{v}$ and $\bar{E}$ and later amend the theorems as needed to accommodate time fluctuations. Thus "force line" becomes synonomous with "particle line" and "trajectory".

If the number density of a collection of particles all having the same mobility is given by "N" particles per m^3 of air, then (4.1) may be modified to describe the particle flux density $\bar{\Gamma} = N\bar{v}_p$ (particles/m^2-sec)

$$\bar{\Gamma} = N(\bar{v} + b\bar{E}) \tag{4.2}$$

These particles must be physically conserved, whence

$$\nabla \cdot \bar{\Gamma} + \frac{\partial N}{\partial t} = 0 \tag{4.3}$$

Combining these two equations yields

$$(\bar{v}+b\bar{E}) \cdot \nabla N + N \nabla \cdot (\bar{v}+b\bar{E}) + \frac{\partial N}{\partial t} = 0 \tag{4.4}$$

If we approximate the flow as incompressible, and neglect the perturbation to the imposed electric field by the charge on the particles themselves (or by any space charge present from

corona) then we may say

$$\nabla \cdot \bar{v} = 0$$

$$\nabla \cdot \bar{E} = 0 \tag{4.5}$$

in the volume of interest; whence:

$$(\bar{v} + b\bar{E}) \cdot \nabla N + \frac{\partial N}{\partial t} = 0 \tag{4.6}$$

What Eq. (4.6) says is that, if we move along the trajectory $\frac{d\bar{x}}{dt} = \bar{v} + b\bar{E}$, then

$$\frac{d\bar{x}}{dt} \cdot \nabla N + \frac{\partial N}{\partial t} = \frac{dN}{dt} = 0 \tag{4.7}$$

or, in other words, the density of particles N remains constant along the trajectory defined by $(\bar{v} + b\bar{E})$. A physical statement equivalent to (4.7) would be that, because $\bar{v}$ and $\bar{E}$ are both solenoidal, there may be neither a source nor sink of particles as we travel along a trajectory line. The particles are neither rarified by a divergence in air flow, nor by a self-repulsion from electric forces.

If the particle line terminates on a rigid boundary surface, where the normal flow $\bar{v}_{\perp}$ must physically always be zero, then the deposition of particles of mobility b on the surface, at the terminus of the trajectory, will be

$$-\bar{n} \cdot \bar{\Gamma} = -\bar{n} \cdot Nb\bar{E} \tag{4.8}$$

where $\bar{n}$ is an outward directed unit vector normal to the surface.

Thus, the rate of deposition of particles per unit area on the surface is simply given by the particle mobility, the inwardly directed normal electric field, and the number density of particles, which may be specified anywhere along the trajectory line. The value of N may thus be taken as some ambient far from the region where, for example, the presence of the insulator string distorts $\bar{v}$ and $\bar{E}$ from otherwise uniform or well known values.

Note that particle lines may also originate on the solid surface; they will do so where the vector $b\bar{E}$ is directed outward. These particle lines of course, do not originate at a source of particles N, hence no deposition takes place if $\bar{n}\cdot b\bar{E}$ is positive.

Equation (4.8), which describes the deposition of particles on a solid, rigid surface, may be generalized to describe the flux of particles through any designated surface where $\bar{\Gamma}$ is known. Note that $\bar{v}_{\perp}$ is no longer necessarily zero.

$$- \bar{n} \cdot \bar{\Gamma} = - [\bar{n}\cdot N\bar{v} + \bar{n}\cdot Nb\bar{E}] \qquad (4.9)$$

Several definitions now enter the deposition picture:

Critical points occur in the volume of interest where $(\bar{v} + b\bar{E}) = 0$; that is, where the electric and wind forces on the particle just balance. If the geometry of the region

is uniform in one dimension, critical points often become critical lines. Critical lines are important because the trajectories passing through them form the boundaries between regions where the trajectories may carry particles (i.e., originate within a source of particles), and regions where no particles may be carried (i.e., the trajectories originate on rigid solid surfaces).* The deposition free region bounded by trajectories that pass through the critical line or point may fall into one of two categories. The first and simplest is depicted in Fig. 4.4, where the force lines are everywhere outward from the solid surface on which deposition is being examined. An isolated, positively charged conducting sphere in the presence of positive particles, for example, would fall into this category. From the basic considerations of Eq. (4.8), namely that $\bar{n}\cdot b\bar{E}$ is everywhere positive, we expect no deposition on such a surface. The trajectories passing through the critical point form an "umbrella" of region shielded from the particle source at infinity.

The second category of deposition free region involves solid surfaces where the normal electric field may change sign on the same surface, as on a segmented electrode, or on a charge-free conducting sphere in a uniform electric field. Such a region is depicted in Fig. 4.5. Here, the trajectories passing through the critical line once again form an umbrella

---

*It is assumed here that any particles which may previously have been deposited on solid surfaces are not reentrained.

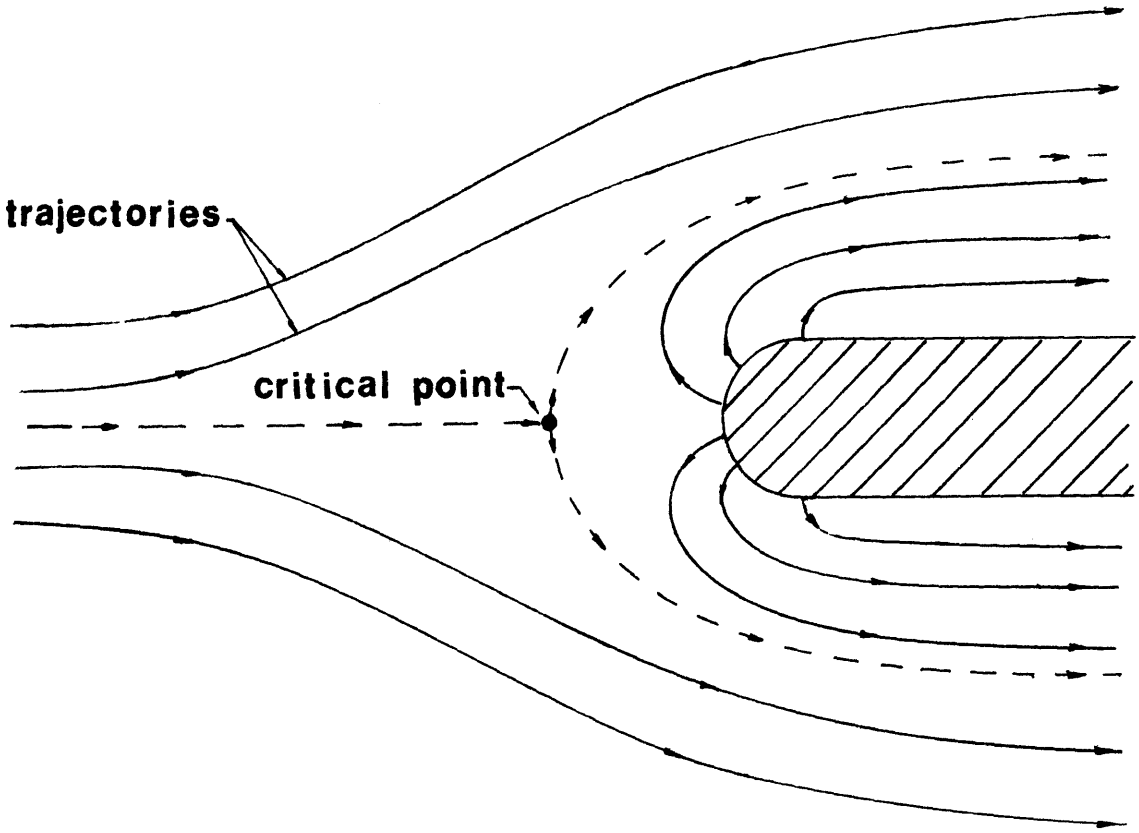

Figure 4.4 Flow Dependent Critical Point of the First Kind

shielding the surface of particles, so that if $b\bar{E}$ is inwardly directed at any points on the deposition free surface, then these points must represent the termini of trajectories also originating within the same deposition free region. We know this because the solenoidal particle lines cannot cross over each other, except at critical points where the total force is zero. Thus, the criteria $\bar{n}\cdot b\bar{E}$ = negative implicit in Eq. (4.8) is a necessary, but not sufficient condition for assuring deposition on a given surface. In general, each specific problem must be examined to determine whether deposition free regions bounded by trajectories passing through critical lines exist.

Boundaries formed where these critical trajectories encounter a rigid surface will be called demarcation lines. For all the categories discussed so far, where the critical lines or points appear in the volume above the rigid surface, the location of the demarcation lines will generally depend on the magnitudes of the field and flow, as well as the geometry of the rigid boundaries. If a critical line happens to coincide with the solid surface, it then also becomes a fixed demarcation line whose location is independent of the flow. We may see this very simply by noting that $\bar{n}\cdot\bar{v}$ is zero on such a "surface" critical line, hence it must coincide with the point where $\bar{n}\cdot b\bar{E}$ passes through zero on the surface. The location of this point is of course independent of the flow. Such a critical line is illustrated in Fig. 4.6.

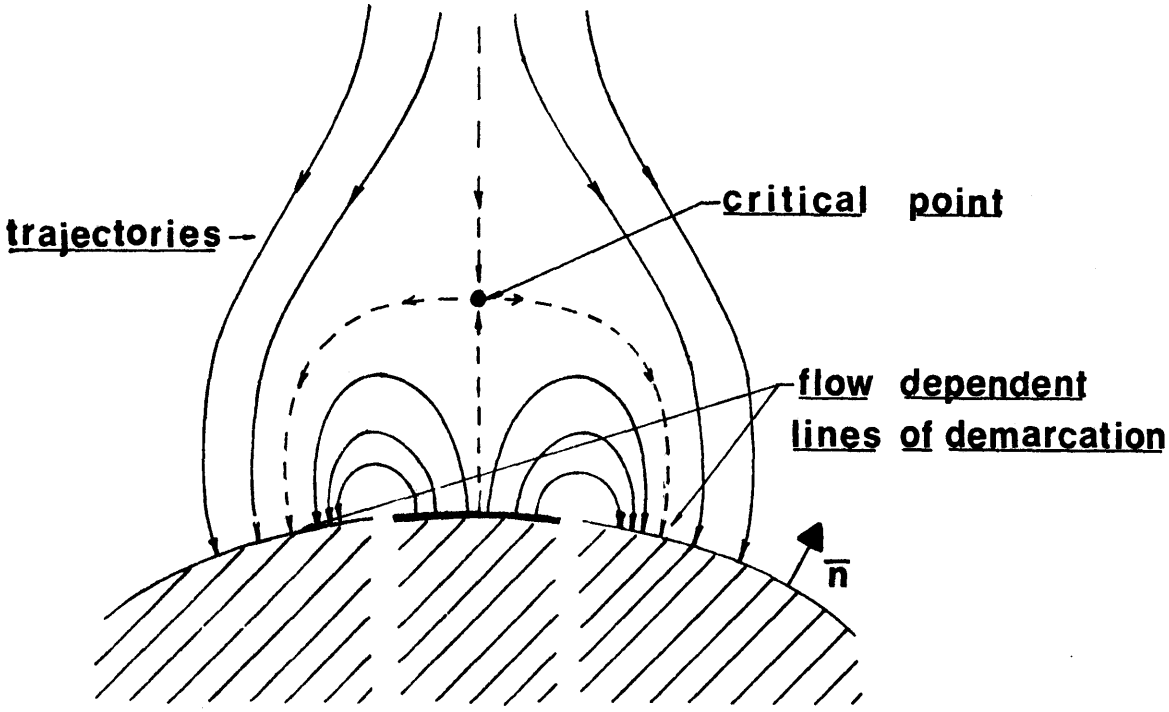

Figure 4.5 Flow Dependent Critical Point of the Second Kind

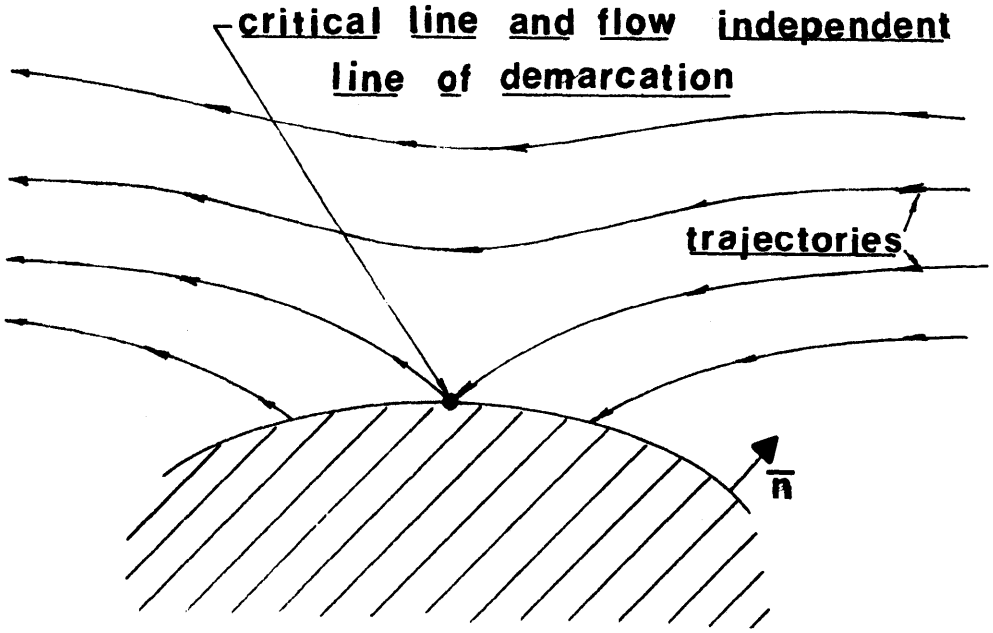

Figure 4.6 Fixed Demarcation Line

A homogeneous particle source is one which loads all force lines that enter the region of interest, but don't originate on rigid surfaces within the region, with the same density of particles N. Typically, the homogeneous source is located "at infinity" in one direction, far from the region of interest, where the force lines are predominantly composed of ambient wind carrying particles into the system. Typically, we will examine particle lines terminating on an insulator surface, and assume that all those lines originating from far away carry the particle density N to the insulator surface.

Slowly varying flows and fields occur when $\bar{v}$ or $\bar{E}$ are functions of time, but vary much more slowly than the time typical of particle transit. Hence, for a given particle, we may still equate particle trajectories with force lines calculated at the time of interest. This equivalence of time invariant and "quasi-steady" situations is valuable for dealing with slow changes in the ambient wind speed or changes in the electric field around the insulator caused by previously deposited contaminants. In systems where the flow and field are slowly varying, the critical lines and flow dependent demarcation lines might of course be slowly varying also.

Fluctuating flows are those in which the rate of change of force lines is so rapid that they may no longer be equated with particle lines. Usually, a statistical analysis is necessary to predict contamination when, say, the air flow is very turbulent.

One model for dealing with the inherently complicated turbulent situation has proven successful in the description of air pollution control devices. In the local mixing model, it is assumed that the stochastic process of fine scale turbulence, on the time average, distributes particles uniformly throughout the volume of interest. Hence, deposition simply takes place wherever $\bar{n} \cdot b\bar{E}$ is negative.

4.4 Macroscopic Fields

In developing a model for particle precipitation, it is practical to separate the field into a part relatively removed from the insulator string and conductor and a part in the immediate vicinity of the string. The former, termed the macrofield, is influenced by the average distribution of potential over the span of the insulator, but is relatively insensitive to the "bumpiness" of this distribution. The latter is a strong function of the units composing the string. The field distribution within this so called "microregion" is highly dependent on the specific unit design. The boundary separating the micro and macroregions may be selected with some latitude for each specific string configuration, but typically, the microregion will be selected so that the effect of the transmission line conductor can be ignored in computing the field and flow in the region. The macro-micro boundary on the insulator string used in the experiment will be chosen, for reasons that will become clear later, as a cylindrical surface

surrounding the outer edges of the insulator skirts. It is important to recognize that for this case, the macro-micro boundary is permeable to the wind. Thus, the particle flux equation (4.9) applies for macrotrajectories entering the boundary. For other insulator designs, for example a skirted post insulator, the macro-micro boundary may be relatively unpenetrated by the wind.

The purpose of this section is to obtain an approximation of the macrofield in the experiment so that particle trajectories can be examined. It is the field in the vicinity of the line conductor and insulator, say, on the order of up to several string lengths away, that is of interest, hence the details of the test chamber walls are not very important. Without the insulator string, the potential distribution around the conductor at sub-corona voltages is very nearly that of a conductor surrounded by a coaxial shell:

$$\Phi = V \frac{\ell n(\frac{r}{R_o})}{\ell n(\frac{a}{R_o})} \qquad (4.10)$$

Here, "a" is the radius of the conductor, "r", the radial distance from the conductor, V the voltage on the line, and R_o is an equivalent coaxial shell radius based on the average distance from the conductor to test chamber walls and plenum ducts. The potential distribution along the insulator string, as discussed in Appendix C, is basically

linear. The potential from the line conductor would like to be logarithmic in the space occupied by the insulator, and hence, distortion of the electric field associated with the logarithmic potential variation (4.10) is to be expected.

Sketches of the equipotentials and field lines, as measured in an electrolytic tank, are shown in Figs. 4.7 and 4.8 in the planes perpendicular and parallel to the line conductor respectively. In the electrolytic tank, the grounded chamber walls and plenum ducts where included in the test configuration. For comparison, the logarithmic equipotentials of Eq. (4.10) are plotted as dotted lines in the perpendicular plane for an equivalent coaxial radius R_o of 1 meter.

From this plot, we see that in radial directions other than along the insulator string, the potential distribution is essentially the same as a coaxial line; moreover, the choice of equivalent radius R_o seems to be a good one. The effect of the insulator string is to bend the equipotentials away from the conductor over the lower three-fourths of the string, and toward the conductor over the upper fourth. As shown in Fig. 4.9, where the logarithmic potential of (4.10) is plotted against the linear distribution of the insulator string, this "three-quarters" point occurs where the logarithmic potential begins to exceed the linear one in going away from the conductor, so the potential plot appears consistent.

In Fig. 4.8, we again see that beyond about a string length from the insulator in the parallel plane, the potential

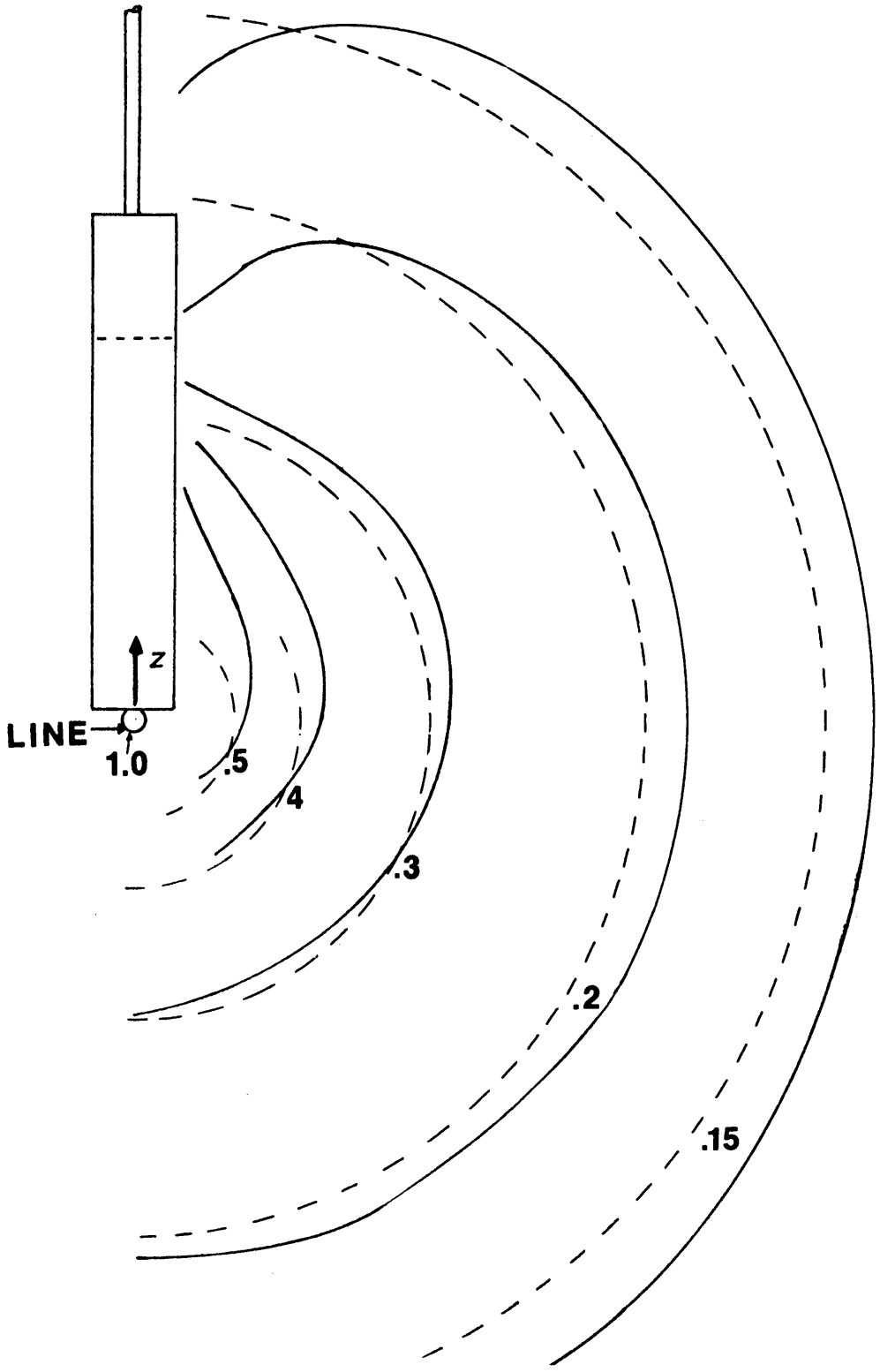

Figure 4.7 Equipotentials Around Insulator String in Plane Perpendicular to Conductor. Solid line were measured in electrolytic tank. Dotted lines are coaxial approximation.

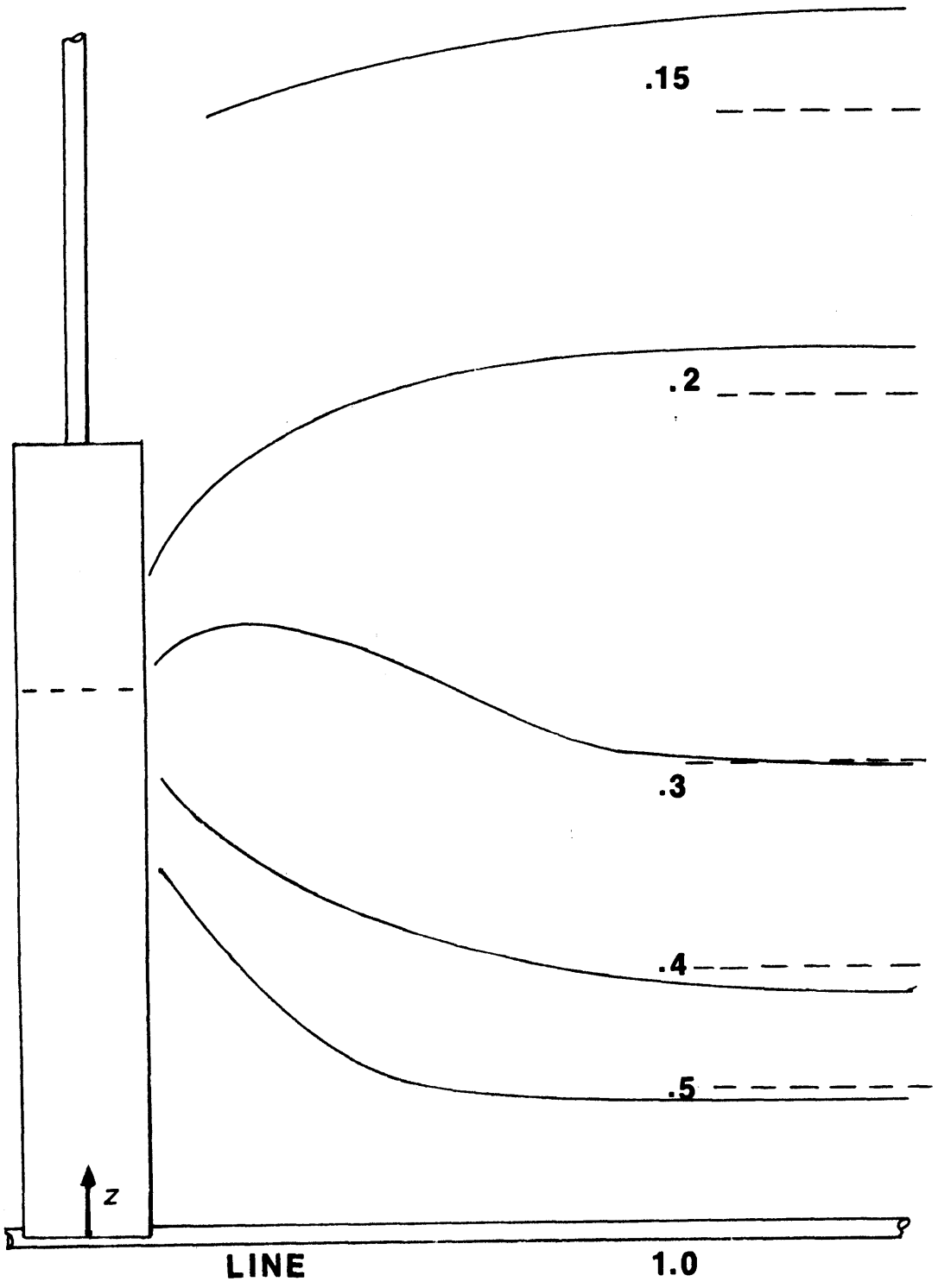

Figure 4.8 Equipotentials Around Insulator String in Plane Parallel to Conductor. Solid lines were measured in electrolytic tank. Dotted lines are coaxial approximation.

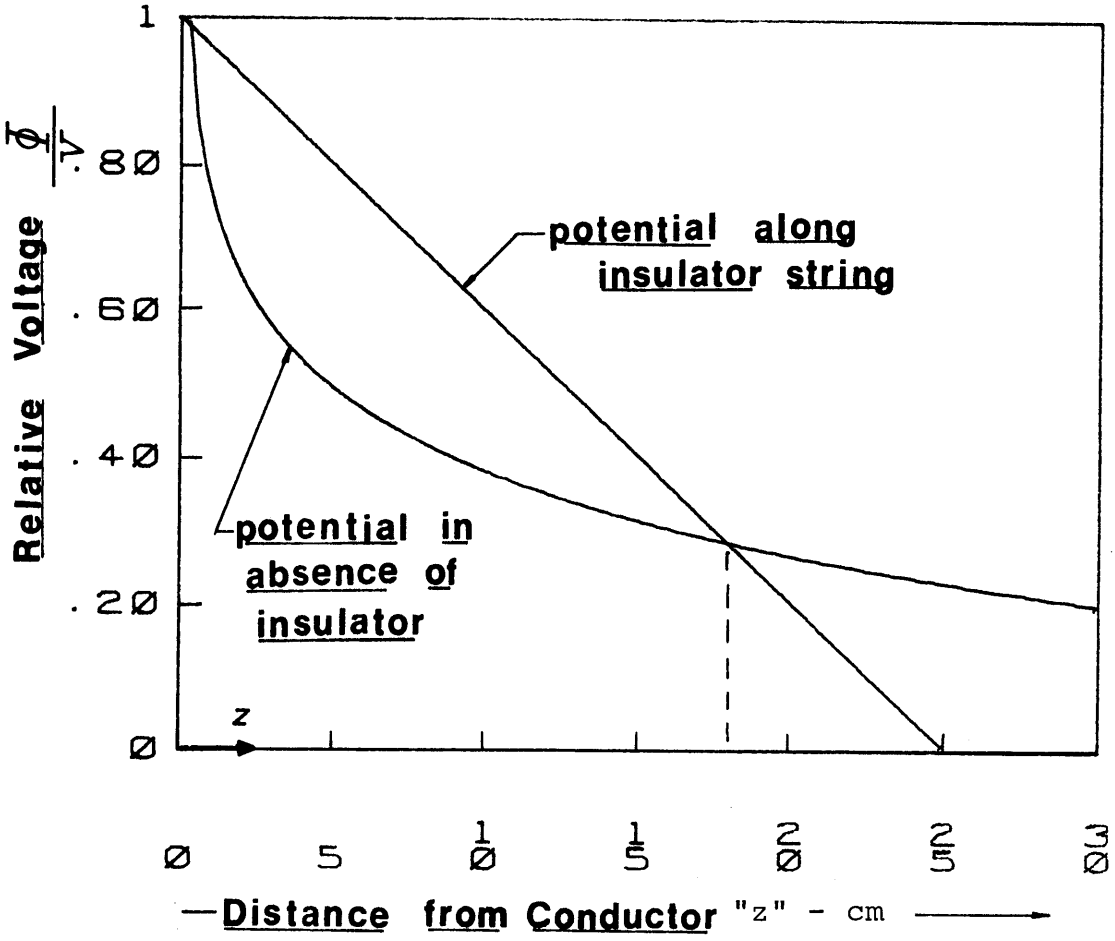

Figure 4.9 Potential Distribution Over Span of Insulator String Compared to Logarithmic Potential of Coaxial Conductor

is very close to the coaxial cylinder approximation, and within this region the insulator distorts the potential to match its own linear distribution.

The conclusion to be drawn from these measurements is that the potential seen in approaching the insulator string from the horizontal direction in the perpendicular plane is essentially just the coaxial approximation, until the very near proximity of the string is reached. This approximation leads to some important conclusions which will be clarified in Section 4.5.

A more detailed approximation to the electric field, which will later be useful for numerical trajectory calculations, can be obtained by the method of charge simulation[30]. In the general formulation of the charge simulation problem, an enclosed region is defined inside which the field solution is sought. The potentials on the surfaces bounding the region must all be specified. Fictitious charges are then judiciously placed outside the boundaries of the region, and their magnitudes adjusted such that the sum of potentials due to all the charges closely matches the actual potentials of the boundaries. The electric field interior to the bounded region is then approximately that due to the external charges. In practice, the potential due to all the external charges and the actual potentials of the boundaries can only be matched at a finite number of select points.

In this particular problem, the important chosen

boundary surface is an imaginary cylinder enclosing the insulator string and extending from the line conductor to some far away grounded shell coaxial to the conductor. Note that this surface is the same one that separates the macroregion from the microregion. Along the surface of the boundary cylinder, the potential is said to decrease linearly to zero in going from the conductor to the top of the insulator string, and to be zero thereafter in continuing toward the coaxial shell. A solution to the electric field is sought outside the cylindrical boundary surface, hence the fictitious charges are placed inside the cylinder, external to the solution region.

The exact formulation of the problem is depicted in Fig. 4.10, where ten charges of as yet unknown magnitude are uniformly spaced at locations z_n along the axis of the insulator string. Three more are placed along the axis of the ground post above the string. Note that the number of charges is here limited to thirteen by the computer routine used to obtain the solution, but in general an arbitrarily large number of external charges could be used. The potential of the line conductor is also included in determining the potential along the boundary surface. The potential along the cylindrical boundary surface becomes:

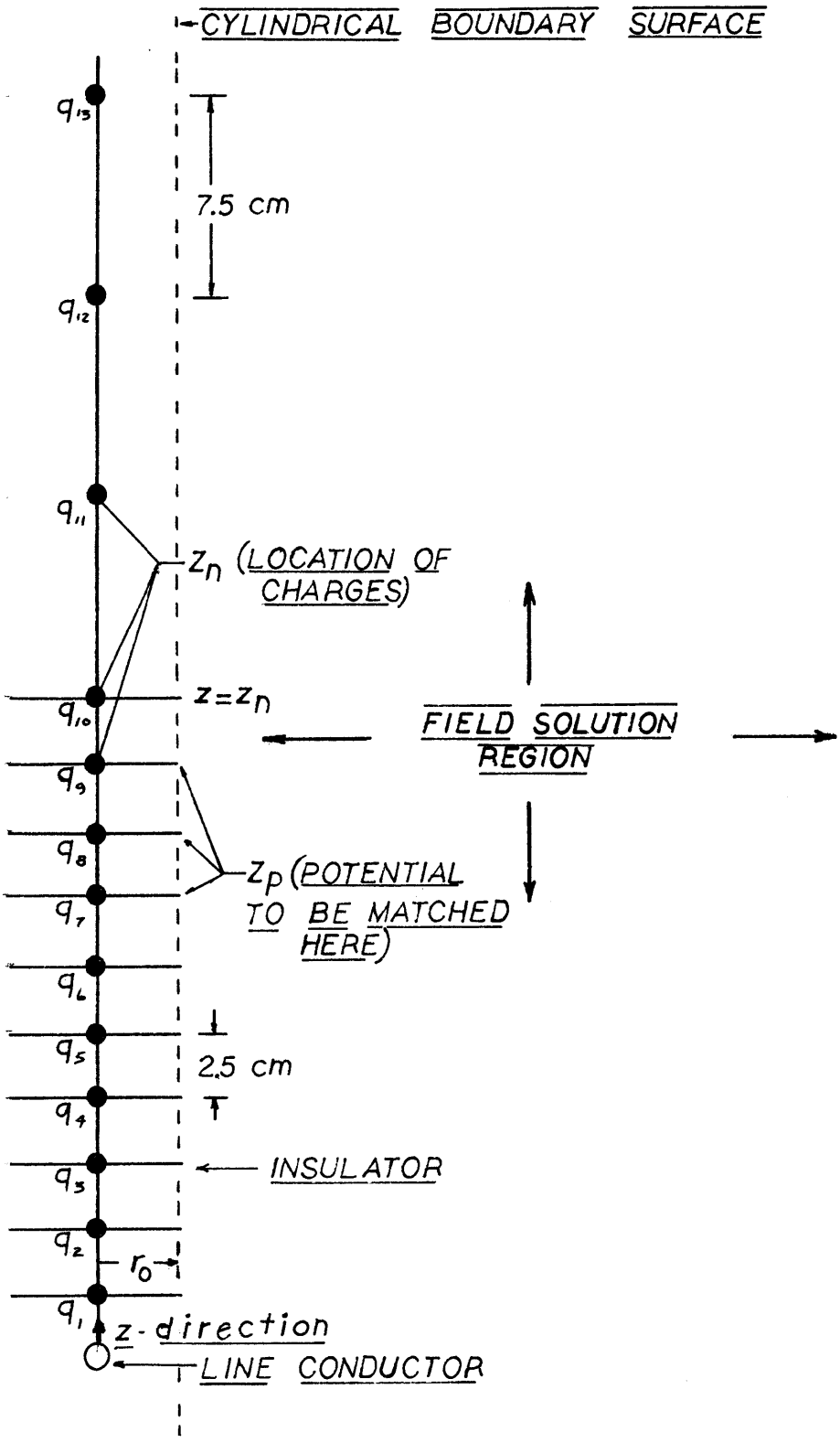

Figure 4.10 Charge Simulation Problem

$$\Phi_s = V \frac{\ell n \left[(z^2 + r_o^2 \cos^2 \theta)^{1/2}/R_o\right]}{\ell n \frac{a}{R_o}}$$

$$+ \sum_{n=1}^{N} \frac{q_n}{4\pi\varepsilon_o} \left[\frac{1}{[r_o^2 + (z - z_n)^2]}\right]^{1/2} \qquad (4.11)$$

where r_o = insulator radius ≡ radius of boundary surface, θ = angle around boundary surface (θ = 0 in the plane perpendicular to the line conductor), z = height above line conductor, z_n = location of the n^{th} charge q_n, N = total number of charges, and R_o, the radius of the remote coaxial shell, is again chosen as 1 meter. The first term in (4.11) represents the coaxial line potential, and the second term the superimposed potential from the N point charges. Ideally we would like (4.11) to match the assumed linear potential of the boundary surface, namely

$$\Phi_s = V \frac{(z_{10} - z)}{z_{10}} \qquad 0 \leq z < z_{10} \text{ (along insulator string)}$$

$$\Phi_s = 0 \qquad z_{10} \leq z < R_o \text{ (along ground post)} \qquad (4.12)$$

The potential due to the point charges, which have as yet to be computed, can be made approximately equal to (4.12) by picking N points on the cylindrical boundary surface at which the potential is to be exactly matched. Because we will

primarily be interested in the electric field in the plane perpendicular to the line conductor, these points, denoted z_p in Fig. 4.10, are positioned at $\theta = 0$ on the cylindrical boundary surface. So doing generates N equations in the q_n. The p^{th} equation, where p=1....N, becomes:

$$\sum_{n=1}^{N} \frac{q_n/V}{4\pi\varepsilon_o}\left[\frac{1}{[r_o^2+(z_p-z_n)^2]}\right]^{1/2} = \frac{z_{10}-z_p}{z_{10}} - \frac{\ell n[(z_p^2 + r_o^2)^{1/2}/R_o]}{\ell n \frac{a}{R_o}}$$

$$0 \leq z_p < z_{10}$$

$$= - \frac{\ell n[(z_p^2 + r_o^2)^{1/2}/R_o]}{\ell n \frac{a}{R_o}} \qquad (4.13)$$

$$z_{10} \leq z_p < R_o$$

where again, z_p is the location of the p^{th} point at which the potential is to be exactly matched. By judiciously selecting the locations of the z_p, the ideal potential (4.12) can be closely approximated by the computed external charges. The ten charges spaced evenly every 2.5 cm along the insulator string can match the linear potential fairly well. The locations of the remaining three charges along the ground post region were fitted by trial and error, and finally spaced 7.5 cm apart above the top of the insulator string, as shown in Fig. 4.10. For simplicity, the z_p are chosen to be equal to the z_n of the point charges. Note that so doing makes the

right hand side of the potential equation (4.13) equal to the "deficit" between the linear potential along the boundary surface, and the logarithmic potential due to the line conductor that would be present in the absence of the insulator string, as has already been discussed and depicted in Fig. 4.9. The potential equations (4.13) can be summarized by

$$\sum_{n=1}^{13} A_{pn} \frac{Q_n}{V} = B_p \qquad p = 1,\ldots,13 \tag{4.14a}$$

where

$$Q_n = q_n/4\pi\varepsilon_o$$

$$A_{pn} = [r_o^2 + (z_p - z_n)^2]^{-1/2} \tag{4.14b}$$

and

$$B_p = \text{"potential deficit"}$$

$$= \left[\frac{z_{10} - z_p}{z_{10}}\right] - \frac{\ell n[(z_p^2 + r_o^2)^{1/2}/R_o]}{\ell n \frac{a}{R_o}} \tag{4.14c}$$

↑ (omit this term along ground post)

The 13 simultaneous equations (4.14) were solved on a general library program of the Wang Model 600-14 desktop computer. The q_n so calculated are listed in Table 4.1. Figure 4.11 shows a plot of the potential due to the line conductor and 13 charges, taken along the cylindrical boundary surface in the plane perpendicular to the line conductor. The

Table 4.1

Solution for the Charges in the Charge Simulation Problem

Along Ground Post:	$q_{13} = -2.31 \times 10^{-10}$	coulombs/kV
	$q_{12} = -2.48 \times 10^{-10}$	
	$q_{11} = -3.37 \times 10^{-10}$	
Along Insulator String:	$q_{10} = -6.51 \times 10^{-10}$	
	$q_{9} = -.124 \times 10^{-10}$	
	$q_{8} = -.889 \times 10^{-10}$	
	$q_{7} = .170 \times 10^{-10}$	
	$q_{6} = .671 \times 10^{-10}$	
	$q_{5} = 1.33 \times 10^{-10}$	
	$q_{4} = 1.74 \times 10^{-10}$	
	$q_{3} = 2.95 \times 10^{-10}$	
	$q_{2} = 1.13 \times 10^{-10}$	
	$q_{1} = 8.55 \times 10^{-10}$	

(coulombs per kilovolt on the line conductor)

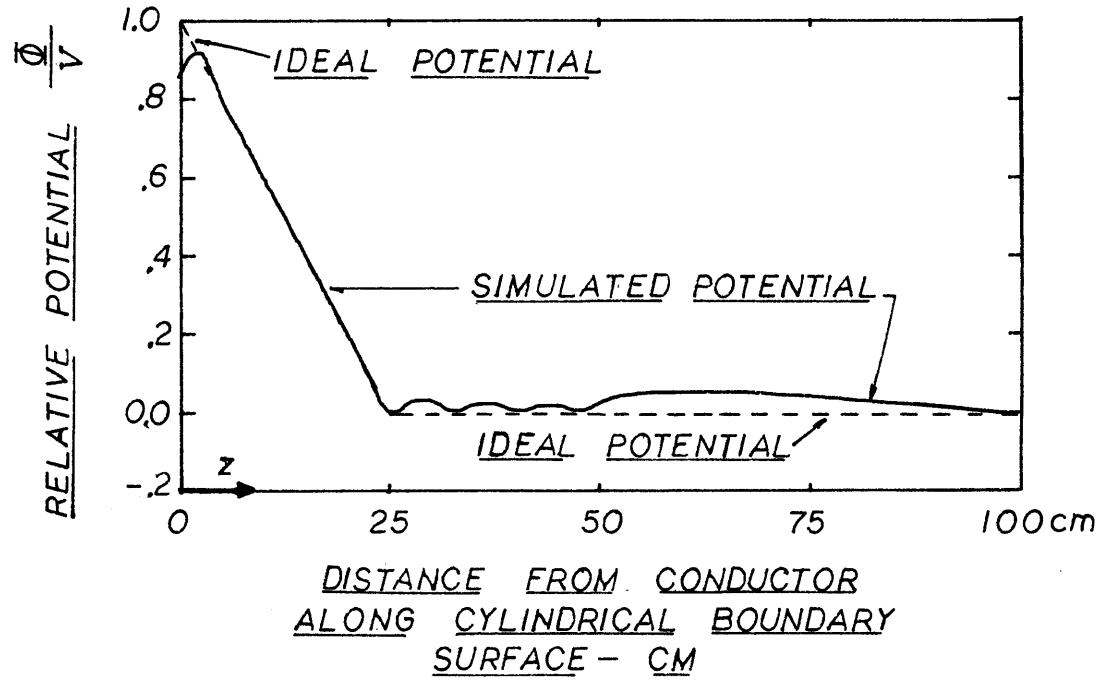

Figure 4.11 Potential Due to External Charges vs. "Ideal" Potential Along Cylindrical Boundary Surface

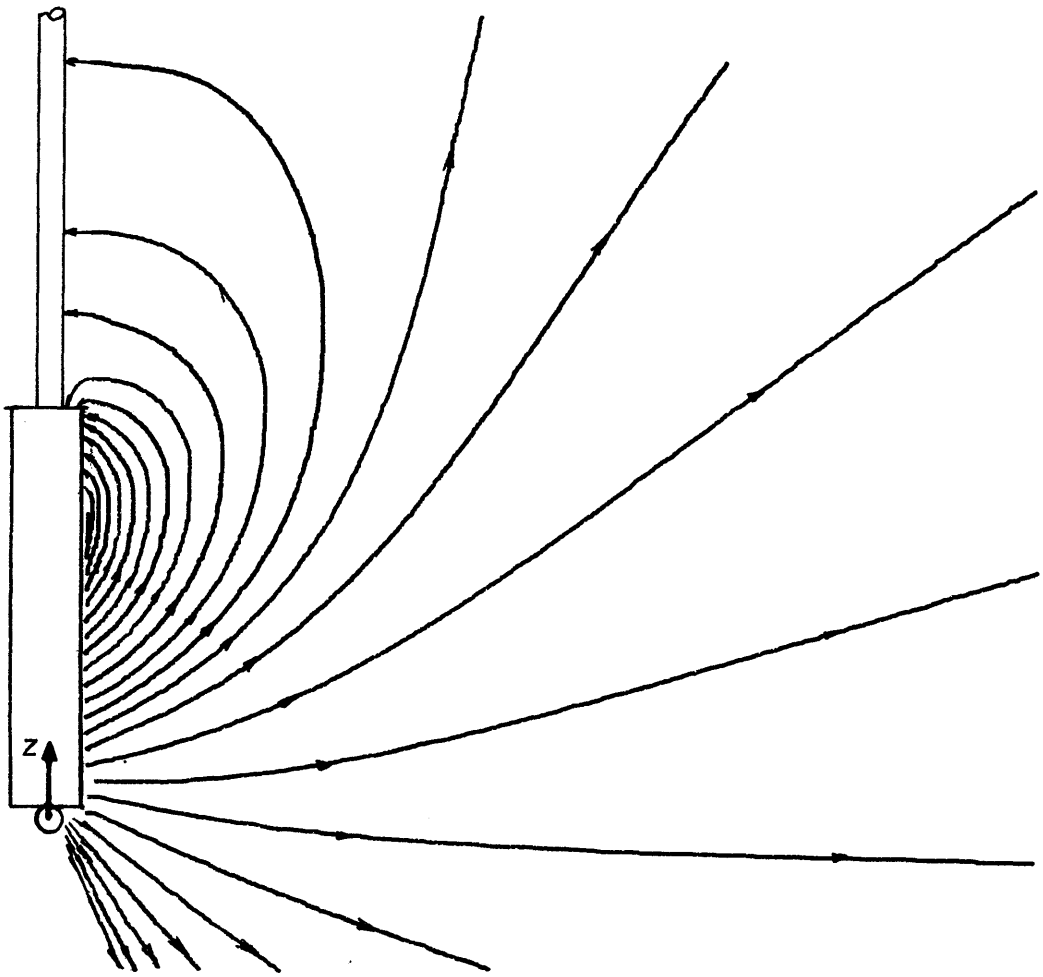

Figure 4.12 Field of External Charges and Line Conductor

dotted line shows what the "ideal" potential (Eq. 4.12) should be.

The associated electric field in the solution region, in the plane perpendicular to the line conductor, is shown in Fig. 4.12. A comparison between this field plot and the equipotentials measured in the electrolytic tank, Fig. 4.7, shows the field approximation to be a good one, especially around the region occupied by the insulator string. Again we see in Fig. 4.12 that roughly one insulator length away from the conductor, the field is predominantly radial and very close to the coaxial solution given by Eq. (4.10). This field solution computed by the method of charge simulation will be useful in the next section for computing macroscopic trajectories in the neighborhood of the insulator string.

4.5 Macroscopic Trajectories

In this section macroscopic trajectories are examined in the coordinate system of Fig. 4.13. A turbulence-free stationary flow is assumed so that force lines are equivalent to the particle trajectories. From the previous section, we see that a good zeroeth order treatment of the macroscopic particle motions can be gotten by simply using the coaxial approximation (4.10) for the electric field:

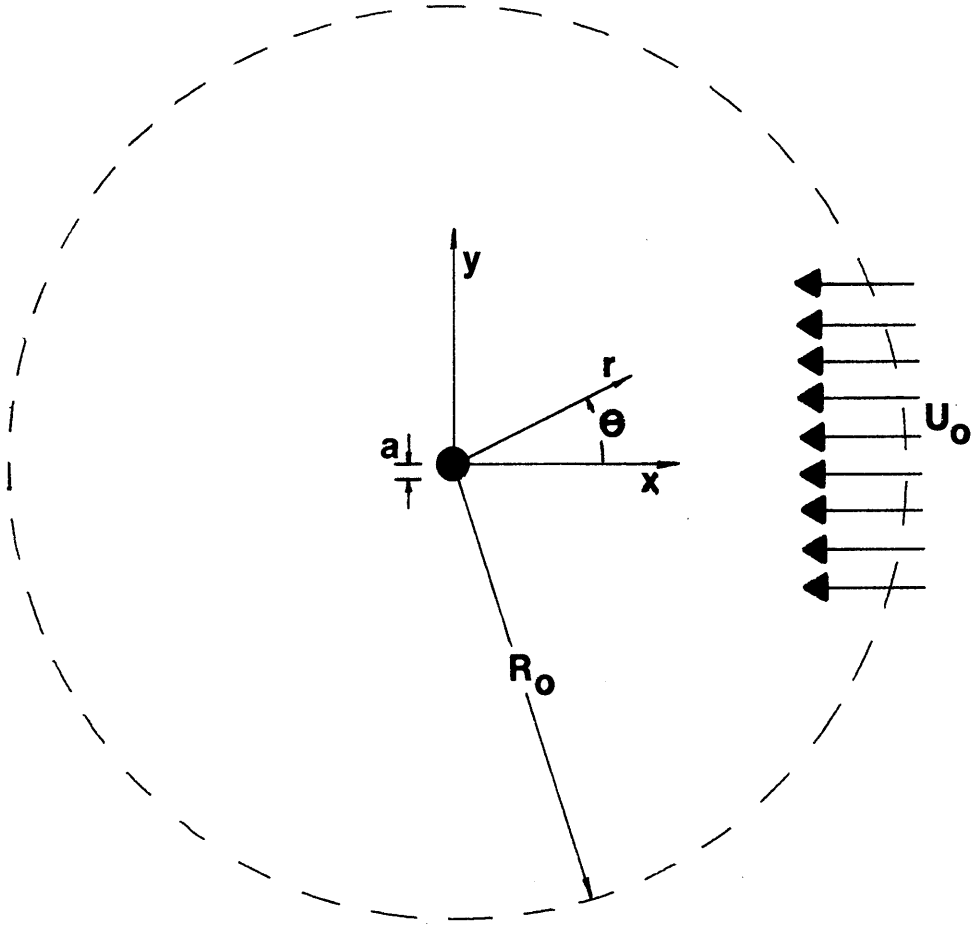

Figure 4.13 Coordinate System for Examining Macroscopic Trajectories

$$\Phi = V \frac{\ell n(\frac{r}{R_o})}{\ell n(\frac{a}{R_o})}$$

$$\bar{E} = \frac{V/r}{\ell n(\frac{R_o}{a})} \hat{i}_r \qquad (4.15)$$

Next is needed an expression for the air flow. With the insulator string absent, a uniform flow, such as that created by the wind generating system in the experiment, is perturbed only the line conductor, and can be written, for wind entering from the right in Fig. 4.13 as:

$$\bar{v} = -\left[U_o \left(1 - \frac{a^2}{r^2}\right) \cos\theta\right] \hat{i}_r + \left[U_o \left(1 + \frac{a^2}{r^2}\right) \sin\theta\right] \hat{i}_\theta \qquad (4.16)$$

where U_o is the ambient wind velocity.

This expression assumes the air to be inviscid, and neglects the boundary layer separation and turbulent flow around the wire. Several conductor diameters away, the flow given by (4.16) is almost uniform. The presence of the insulator string will of course distort the flow of Eq. (4.16), but if the insulator string is basically cylindrical, the flow around it will have the same general form of (4.16), and again the wind velocity will be almost uniform several equivalent cylinder diameters away from the insulator string. In the close proximity of the string the proposed coaxial approximation to the electric field in invalid anyway, hence solutions

for particle motions using (4.16) for the wind flow will be useful if we confine them to the regions where both the flow and field approximations are valid.

Let us examine the case of positive particles incident on a positive conductor, an example of what will hereafter be called "repelled particles". This problem can be solved analytically, but first a general physical description is in order. Particles entering from far away are carried toward the conductor by the wind. Because the line and particles are both positive, the particles tend to be repelled from the conductor -- those entering slightly above the θ=0 line will deflect upward, and those below the line will deflect downward. Particles entering exactly on the $\theta = 0$ line will eventually reach the critical point where the increasing $\bar{E}$-force just balances the $\bar{v}$-force. From this point, two calculable trajectories split to either side of the conductor, and form an "umbrella" under which no particles may go. Within the umbrella, all force lines originate from the conductor surface, and hence don't carry any particles. This system provides a good example of a flow-dependent critical line of the first kind, as described in Section 4.3.

The problem may now be examined analytically. The exact location of the critical line may be found by setting $\bar{v} + b\bar{E} = 0$. Because the $\bar{E}$-field has no θ-component, the critical line of zero force must occur where the θ-component of $\bar{v}$ is also zero:

$$U_o \left(1 + \frac{a^2}{r^2}\right) \sin\theta = 0$$

implies

$$\theta = 0, -\pi \tag{4.17}$$

The radial components of $\bar{v}$ and $\bar{E}$ must then just balance at the critical line. Physically, we know this can only happen at $\theta = 0$, where the two forces are in opposite directions. Thus, at $\theta = 0$:

$$-U_o \left(1 - \frac{a^2}{r^2}\right) + \frac{b\ V/r}{\ell n\left(\frac{R_o}{a}\right)} = 0$$

which may be solved for r:

$$r = \frac{b\ V/\ell n\ \left(\frac{R_o}{a}\right)}{2\ U_o} + \sqrt{\left[\frac{b\ V/\ell n\ \left(\frac{R_o}{a}\right)}{2\ U_o}\right]^2 + a^2}$$

$$\frac{r}{a} = \frac{\underline{V}}{2} + \sqrt{\left(\frac{\underline{V}}{2}\right)^2 + 1} \tag{4.18}$$

where

$$\underline{V} = \left[\frac{b\ V/\ell n\ \left(\frac{R_o}{a}\right)}{a\ U_o}\right]$$

With the $\hat{r}$ and $\hat{\theta}$ values of the critical line specified, we next need a way to trace the trajectories passing through it. First, let us express $\bar{E}$ and $\bar{v}$ as the curl of vector

potentials:

$$\bar{E} = \nabla \times \bar{A}_E$$

$$\bar{v} = \nabla \times \bar{A}_V \tag{4.19}$$

The reader may check that the vector potentials

$$\bar{A}_E = \frac{V\theta}{R_o} \hat{i}_z$$

$$\bar{A}_V = - U_o \left(r - \frac{a^2}{r}\right) \sin \theta \, \hat{i}_z \tag{4.20}$$

are the correct ones. Note that $\bar{A}_E$ and $\bar{A}_V$ both have just a $\hat{z}$-component for this two dimensional system.

It can be shown for flows of the type being considered here that along any trajectory path given by

$$\frac{d\bar{x}}{dt} = \bar{v} + b\bar{E}$$

the following relationship is true:

$$\bar{A}_V + b \, \bar{A}_E = \text{constant} \tag{4.21}$$

where the value of the constant depends on the particular trajectory being considered. (See Appendix B for the derivation of this theorem). For the trajectories passing through the critical point and falling to either side of the conductor,

the constant may be evaluated by using the r and θ solutions (4.17) and (4.18). Because $\theta = 0$, we get:

$$\bar{A}_V + b\,\bar{A}_E = 0 \qquad \text{for trajectory passing through critical line} \tag{4.22}$$

Next we select other values of θ, and solve (4.22) for the corresponding values of r. This is done in Fig. 4.14 for the parameters listed in the figure. Other trajectories that lie close to the critical line are also included in the plot. These are traced by evaluating (4.21) for large values of r, and following the particle in toward the conductor. Note in Fig. 4.14 that beneath the critical line, the trajectories originate on the conductor. These trajectories don't carry any particles, hence the two trajectories passing through the critical line form the "umbrella" over the conductor, under which no deposition takes place. The width of this umbrella projected onto the region normally occupied by the insulator string is found by solving (4.22) for $\theta = \pi/2$

$$\left(\frac{r}{a}\right)\Bigg|_{\theta = \frac{\pi}{2}} = \frac{\pi}{4}\frac{V}{\underline{\ }} + \sqrt{\left(\frac{V\ \pi}{\underline{\ \ 4}}\right)^2 + 1} \tag{4.23}$$

If we select values of V, b, a, and U_o that are typical for the experiment*, the ratio (4.23) becomes:

*V = 60 kV, U_o = .25 m/sec, b = 5 x 10^{-7} m^2/v-sec, a = .0024 m.

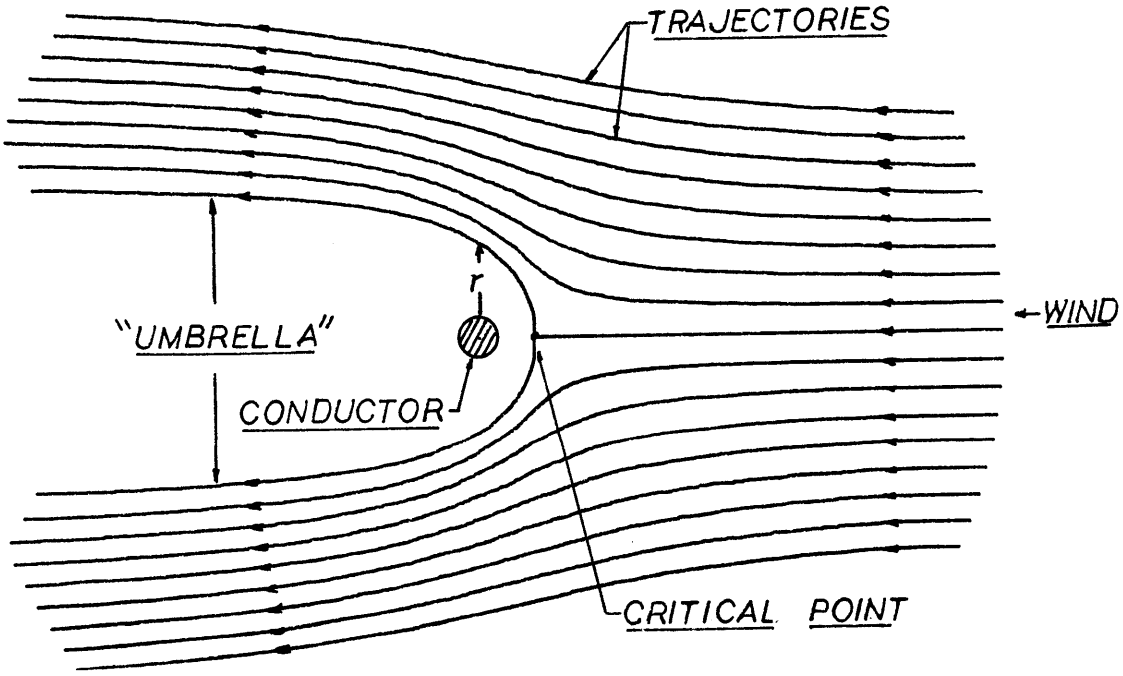

Fig. 4.14 Positive Particle Trajectories for a Positive Conductor in the Stationary Flow Case (Repelled Particles) U_o=.5, V=60 kV, b=5 x 10^{-7} m^2/vs a=.0024 m, $\underline{V} \simeq 4$.

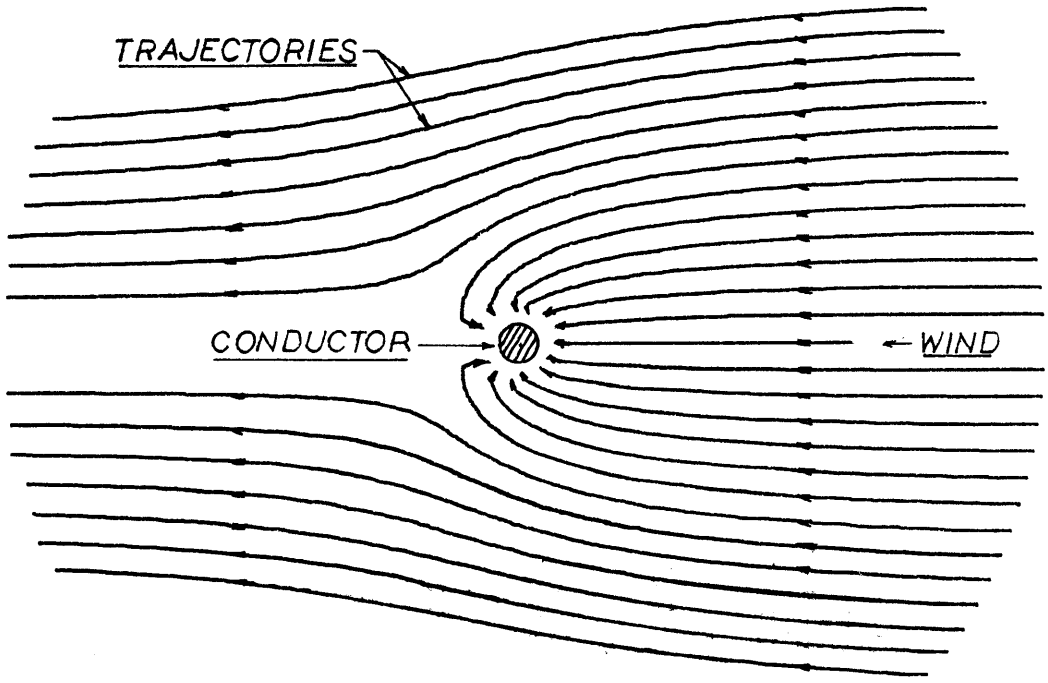

Fig. 4.15 Negative Particle Trajectories for a Positive Conductor in the Stationary Flow Case (Attracted Particles). Same Parameters as Fig. 4.14.

$$\left(\frac{r}{a}\right)\Big|_{\theta = \frac{\pi}{2}} \approx 13 \qquad (4.24)$$

or

$$r_{umbrella} \approx 3 \text{ cm}$$

This ratio represents an insignificant shielding of the insulator string by the repelling force of the line conductor. In fact, as is evident in Fig. 4.14, the wind entirely dominates the particle motion except in the very near vicinity of the conductor. The reader will remember that the model wind velocity of .25 m/sec represents an actual velocity of only .05 MPH, so that at more realistic wind speeds likely to be found in nature, the extent of the particle umbrella will be even smaller. The same calculations may be carried out for oppositely charged, or attracted, particles. The result is Fig. 4.15, in which we see that no umbrella appears at all, as is to be expected for this case.

The results of the analysis presented thus far are significant because they suggest that, except for a small region near the conductor in the case of repelled particles, all trajectories entering the microregions of the insulator string originate with the source of wind. Hence, as discussed in Section 4.3, they will carry particles of density N everywhere into the microregion. In physical terms, we may say that the particles experience no large-scale deflections as they travel

toward the insulator string.

As a check on the preceding trajectory analysis, the more accurate electric field solution obtained by charge simulation may be incorporated into the trajectory equation of Section 4.3:

$$\frac{d\bar{x}}{dt} = \bar{v} + b\bar{E} \qquad (4.25)$$

where $\bar{v}$ is the same air flow (4.16) around the conductor, and $\bar{E}$ is the field computed from the thirteen external charges plus line conductor. For this particular case, it is extremely cumbersome to solve for the trajectories using the vector potential method. Instead, the trajectory equation (4.25) may be solved by Newton's method, in which each component of the derivative is multiplied by Δt to arrive at a new location for the particle after the time increment. The value of Δt must be chosen sufficiently small to insure stable integration.

A plot of trajectories made this way for attracted particles, using the charge simulated field, is shown in Fig. 4.16. The plot was performed on the Wang 600 desktop computer. As expected, the trajectories differ little from those of Fig. 4.15 calculated from the coaxial approximation to the field. The wind continues to dominate the particle motions in the macroregion, and the occurrence of large scale particle deflection still found to be unlikely.

Figure 4.16 Macroscopic Trajectories of Attracted Particles Using Charge Simulated Field

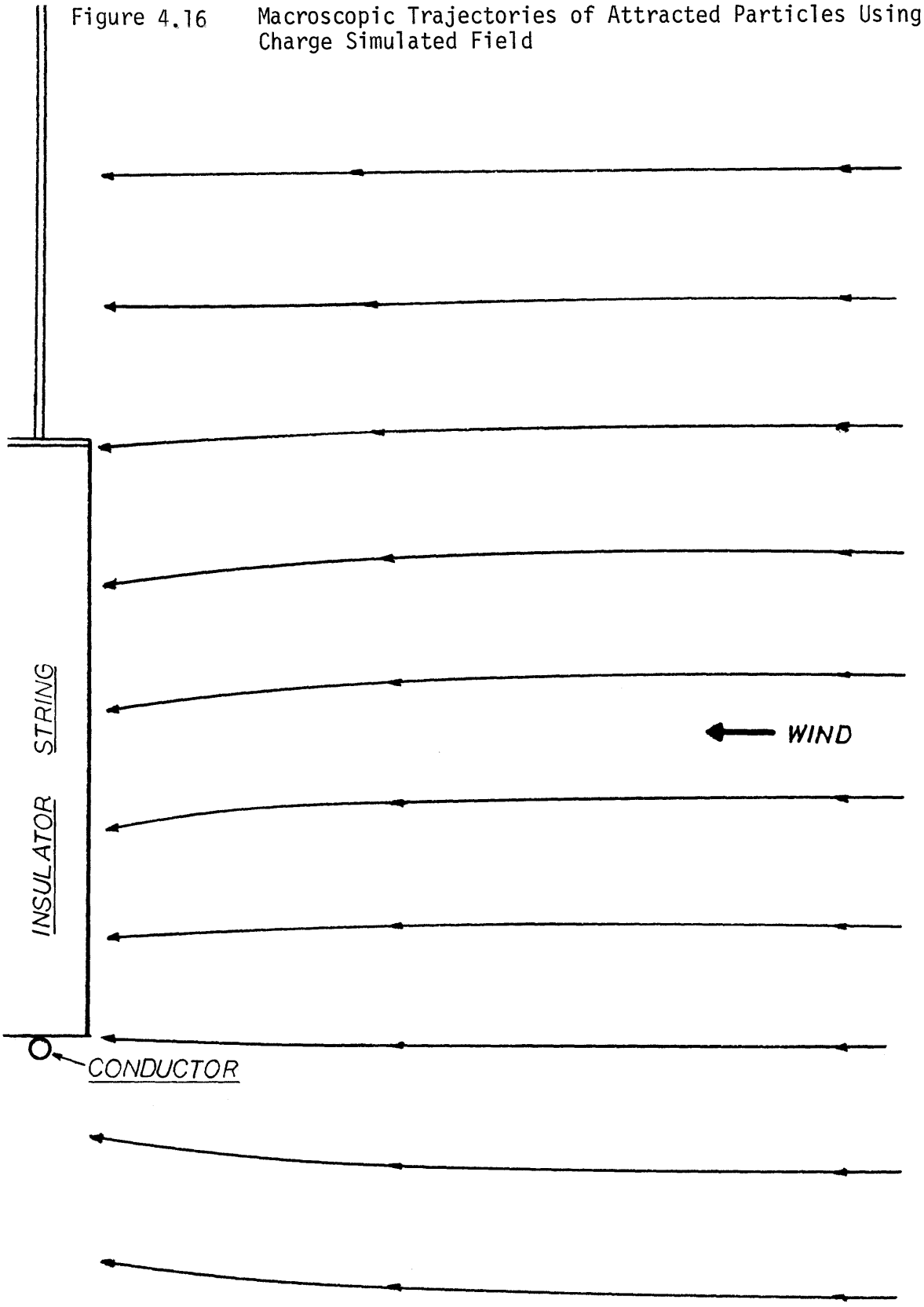

4.6 Microscopic Fields

The previous two sections of this chapter examined the motion of particles on a scale comparable to or larger than the entire insulator string. On the basis of these macroscopic models one can predict which regions of the string are accessed by force lines or particle lines originating on a particle source. The actual deposition process, which occurs on the microscale, is now examined.

When the general topic of contamination-flashover is considered, some detail in understanding the microdeposition appears worthwhile. For example, if contamination on a given insulator is nonuniform, as has been observed experimentally, the eventual flashover process may be effected. An understanding of the mechanisms leading to this nonuniformity is fundamental to an understanding of contamination. In this section, the electric field found between two insulator disks will be examined, to form the foundation for the subsequent sections on small scale deposition patterns. Suitable assumptions regarding the nature of the microfield lead to a solution that can be obtained without the aid of a computer.

Finding the potential distribution along the surface of an insulator in the sub-corona regime is essentially a conduction problem[15]. The resistance of glass-like insulating materials is usually dominated by a conducting surface layer[5,27], formed by adsorbed moisture and contaminants, which produce surface resistivities that can be several orders of magnitude

lower than the bulk substrate resistance. In a first order determination of the local field between two disk suspension insulators, it is useful to model them as perfectly insulating circular disks, surrounded by a thin, uniform conducting layer, as depicted in Fig. 4.17. This simplified picture neglects secondary effects that may lead to nonuniformity in the conducting layer. For example, surface resistivity may not be constant in time, but may increase after the voltage is applied and localized joule heating dries out some of the adsorbed moisture layer.[15] Similarly, surface, and bulk-to-surface migration of conducting ions may occur, thereby causing local changes in the surface resistivity at conductor interfaces. For the present purpose it is appropriate to model the surface conducting layer as being uniform.

The solution for the potential distribution along the uniform conducting layer is determined by current conservation. In terms of the coordinates defined in Fig. 4.18, the solution along the bottom surface of the upper disk may be written, in terms of the voltage, $\frac{V_o}{2}$, at the outer edge, r_o

$$\phi = \frac{V_o}{2} \frac{\ell n(r/r_i)}{\ell n(r_o/r_i)} \tag{4.26}$$

The field solution between two disks will be almost symmetric about the center plane between them. The presence of the line conductor at the bottom end of the insulator string will cause an asymmetric perturbation about this plane, but we will

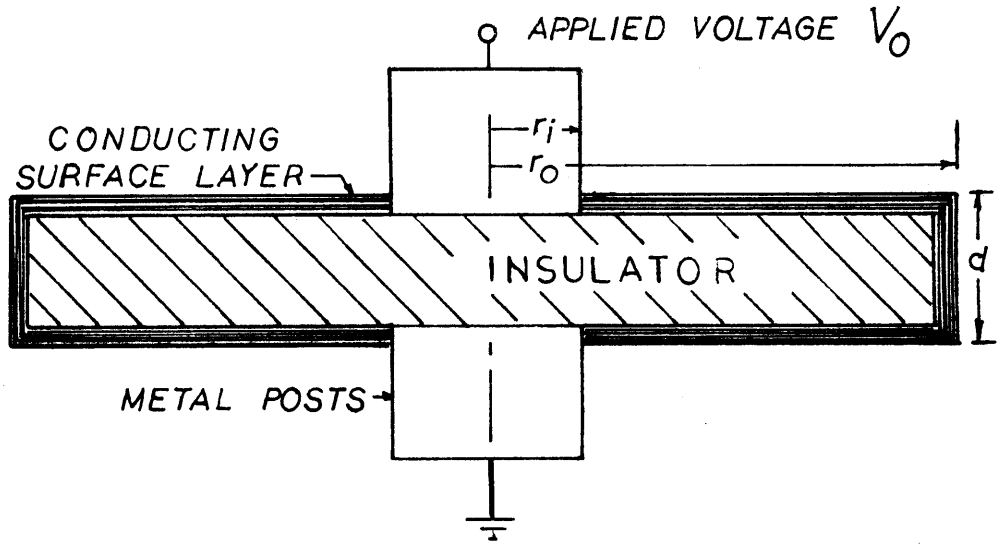

Figure 4.17 Idealized Insulator With Surface Conducting Layer

ignore the effect for now, so that the center plane may constitute a boundary surface of zero potential. The other necessary approximation that may add error to the field solution is the assumption that the potential changes linearly as one goes from the outer edge of the top disk straight down to the outer edge of the next disk. The closer together the two adjacent disks, the better this approximation. The remaining boundary condition makes the potential along the surface of the metal zero. The geometry and associated boundary conditions for this generalized solution are summarized in Fig. 4.18. The solution is confined, of course, to the region inside the stated boundary surfaces. Note the outer boundary surface coincides with the macro-micro boundary surface chosen in Section 4.4, and the potential assumed along this surface consistent with that used to calculate the charge simulated macrofield.

A convenient solution to Laplace's equation, which satisfies the assumed boundary conditions, can now be implemented in the stated region:

$$\phi(z,r) = \frac{V_o/2}{\ell n(\frac{r_o}{r_i})} \ell n\ (\frac{r}{r_i})\ (\frac{z}{\ell}) \qquad (4.27)$$

By picking a value of potential between $\frac{V_o}{2}$ and 0, the above equation may be solved for z(r) to give the associated equipotential surfaces:

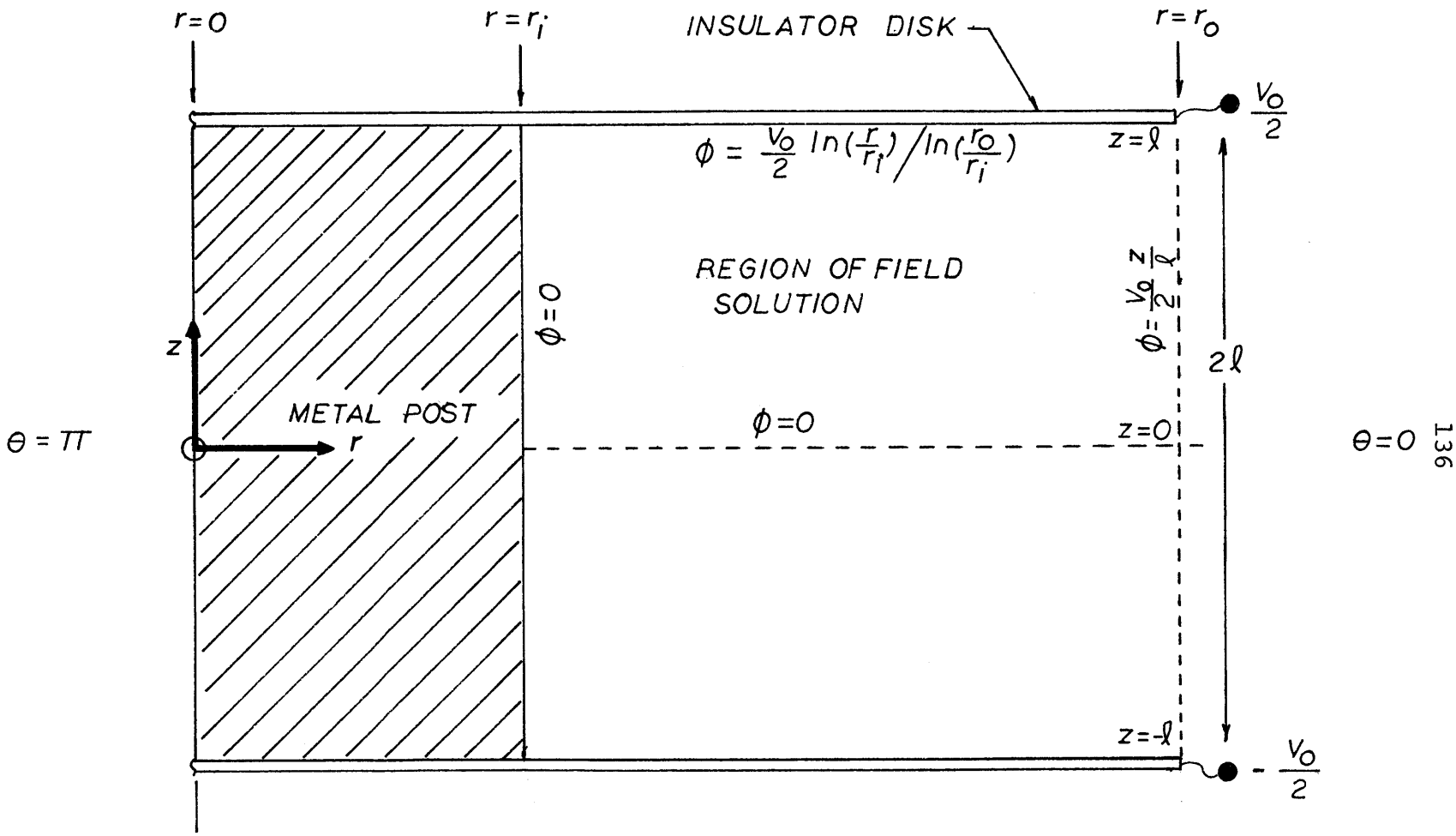

Figure 4.18 Coordinates and Boundary Conditions for the Field Solution Between Two Insulators

$$z(r) = \frac{\ell\,(2\phi/V_o)\ \ell n\ (r_o/r_i)}{\ell n\ (r/r_i)} \tag{4.28}$$

This equation is convenient to plot. The equipotentials are shown with field lines in Fig. 4.19.

The field lines are given simply by $E = -\nabla\phi$:

$$E_r = -\frac{V_o/2\ell}{\ell n(\frac{r_o}{r_i})}\ \frac{z}{r}$$

$$E_z = -\frac{V_o/2\ell}{\ell n(\frac{r_o}{r_i})}\ \ell n\ (\frac{r}{r_i}) \tag{4.29}$$

These equations (4.29) represent a generalized microfield solution, which, as written, reflect the field direction of a negatively energized insulator string. Their application to a specific problem must take into account the actual polarity of the line conductor, and the voltage actually existing at the edges of the insulator disks between which a solution is sought.

4.7 Microscopic Trajectories

The particle trajectory concept of Section 4.5 can be applied, together with the approximate field solutions of the preceding section, to the microregion between two disk suspension insulators. In the analysis that follows, the flow

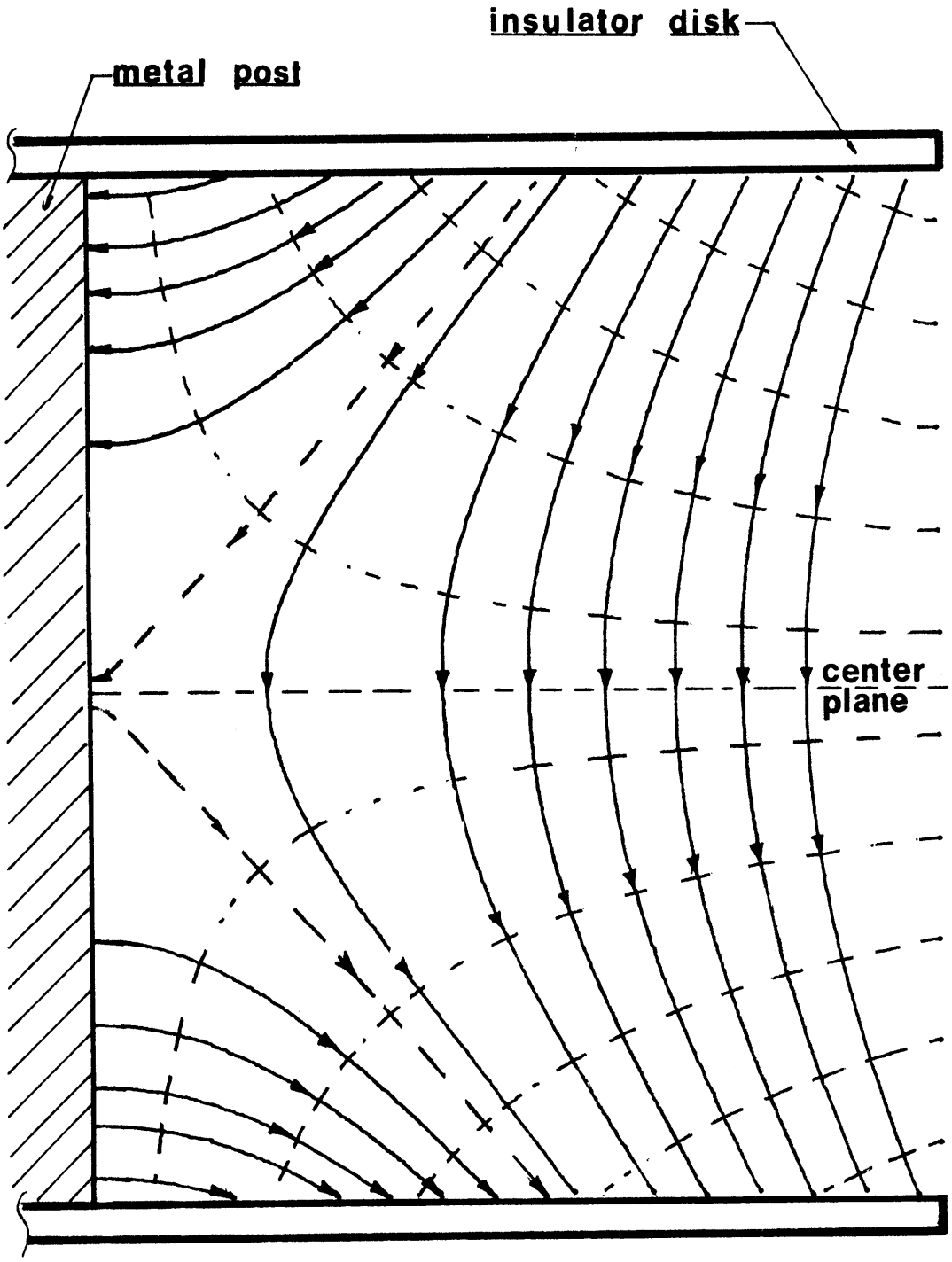

Figure 4.19 Equipotentials and Field Lines Between Two Insulators

is represented two dimensionally in the horizontal plane. Since the azimuthally symmetric field is represented in the r-z plane, it is again much more convenient to derive particle lines - also force lines for the assumed stationary flow case - by numerical computation, although in principle they may also be calculated in closed form using the vector potential method.

Let the flow, consistent with the geometry and coordinate axes of Fig. 4.18, be described by the potential flow solution subject to the boundary conditions of no normal flow at $r = r_i$, and uniform flow equal to the ambient wind velocity far from the insulator string, in polar coordinates:

$$v_r = - U_o \left[1 - \left(\frac{r_i}{r}\right)^2\right] \cos \theta$$

$$v_\theta = U_o \left[1 + \left(\frac{r_i}{r}\right)^2\right] \sin \theta \qquad (4.30)$$

where U_o is the ambient particle laden wind velocity, flowing from the $\theta = 0$ direction. The simplified expression (4.30) for wind flow, which is similar to the expression of Section 4.5, neglects the boundary layer separation around the back of the cylindrical post and the boundary layer formation at $z = \pm \ell$ along the solid surfaces of the insulator disks.

Although the details of the boundary layer are quite complex, a general rule of thumb for estimating its thickness can be gotten from the approximate solution for the laminar

boundary layer forming over the surface of a semi-infinite flat plate in a uniform wind at low Reynold's numbers. Suitable assumptions lead to the expression:[31]

$$\delta(x) = 4.65 \sqrt{\frac{\eta\, x}{U_o}}$$

where $\delta(x)$ is the boundary layer thickness, and x is the distance from the leading edge of the plate. Setting x equal to half the distance from the disk edge to metal post on a scale model insulator yields, for U_o = .2 m/sec,

$$\delta(x) \sim 4.65 \left[\frac{(1.83 \times 10^{-5})(.0254 - .0095)/2}{.2}\right]^{1/2}$$

$$\sim .004 \text{ m}$$

This value of δ may be compared to the disk separation

$$2\ell \tilde{=} .02 \text{ m}$$

Although not of insignificant thickness, the boundary layer is considered ignorable, with the understanding that any particles carried by trajectories to the outer boundary layer edge will be pulled across the layer by the normal electric field existing at the solid surface. Thus the conclusion that deposition will be determined only by the value of normal electric field at the surface will still be valid, even though the existence of the boundary layer requires that both the normal and tangential components of $\bar{v}$ be zero at the

solid surface. The error introduced in neglecting the boundary layer will appear only in the location of the endpoints of trajectories terminating on solid surfaces; i.e. the location of such an endpoint will be incorrectly predicted, if the boundary layer is neglected, by a distance at most on the order of the average wind velocity in the boundary layer times the transit time of the particle across the boundary layer:

$$\Delta x \sim \frac{\delta(U_\infty/2)}{b(V/2\ell)} \approx \frac{(.004)(.1)}{(5 \times 10^{-7})(2.5 \times 10^{5})} \simeq .003 \text{ m} \equiv 3 \text{ mm}$$

Typically, the error introduced will be much less.

If we ignore the inertia of the particles entering the system, as described in Section 2.5, we may once again conclude that at any point in time, the motion of a given particle may be described, as derived in Section 4.3, by:

$$\frac{d\bar{x}}{dt} = \bar{v} + b\bar{E} \qquad (4.31)$$

Remember that particle lines are again equivalent to force lines in this stationary flow case. The Eqns. (4.31) form a set of three coupled, nonlinear differential equations which, given the initial position of a particle, may be numerically integrated to find the particle trajectory.

Such an integration was performed, again using Newton's method, on the Wang plotter for the following values of

parameters, which include a range of wind velocities:

$V_o = -5$ kV	$V_o = -5$ kV	$V_o = -5$ kV
$U_o = .5$ m/sec	$U_o = .25$ m/sec	$U_o = .17$ m/sec
$b = 5 \times 10^{-7}$ m^2/v-s	$b = 5 \times 10^{-7}$ m^2/v-s	$b = 5 \times 10^{-7}$ m^2/v-s

dimensions = those of the scale model insulator

Figure 4.20 shows plots of the calculated trajectories in the r-z plane located parallel to the wind at $\theta = 0$ (wind entering from the right) for attracted particles entering the microregion at a variety of points. If the incident particles entering the microregion represent a homogeneous source, then we may expect deposition at the terminus of each of these trajectories. Clearly, a flow independent demarcation ring exists in this plane at $z = 0$ on the metal post, and a flow dependent demarcation ring on the lower insulator surface at the various denoted values of r_d.

The flow independent demarcation ring at $z = 0$ coincides with the experimentally observed clean band on the metal post. The deposition on the post in the band above $z = 0$ is also consistent with experimental observation, for this case of attracted incident particles.

The nature of these trajectory plots can be understood physically by examining the field solution of Fig. 4.19. In addition to the z-component of the field which drives the particles downward, there is an r-component which tends to

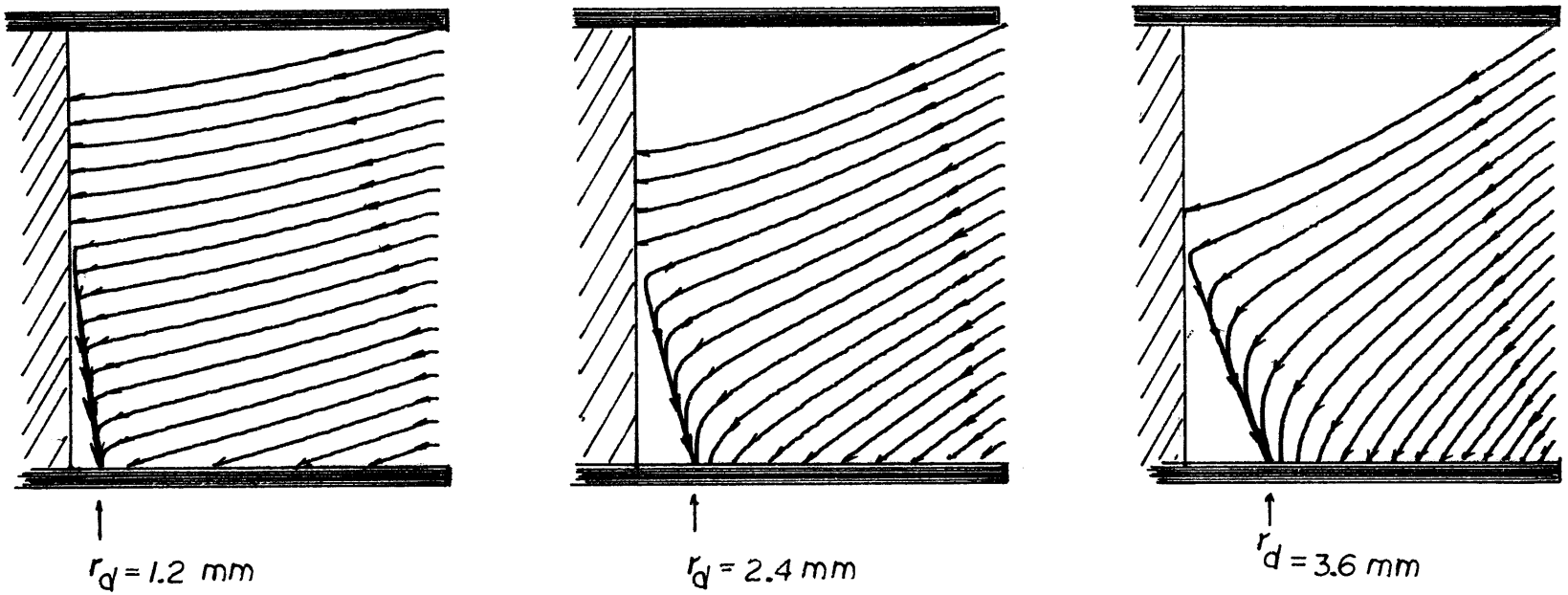

$b = 5.0 \times 10^{-7}$ m^2/v-sec

U_o = .5 m/sec

$b = 5.0 \times 10^{-7}$ m^2/v-sec

U_o = .25 m/sec

$b = 5.0 \times 10^{-7}$ m^2/v-sec

U_o = .17 m/sec

Fig. 4.20 Particle Trajectories in the θ=0 Plane for a Variety of Wind Velocities (attracted particles)

enhance the wind force above the center plane, and buck the wind below it. As the wind velocity becomes smaller for a given particle mobility, fewer particles are able to reach the upper portion of the post before being driven downward by the coulomb force into the region below the center line, where they are repelled from the post. Because the normal field points outward everywhere on this lower section of the post, no deposition may take place on it. The area on the post at $z = 0$ where $\bar{E} = 0$ and $\bar{v} = 0$ is of course a region where no deposition may take place regardless of the sign of the charged particles. The observed clean ring is thus explained.

The "turnaround" point for trajectories crossing below the centerplane and terminating of the lower disk occurs where $v_r = - bE_r$ i.e., the wind force just balances the $\hat{r}$-directed coulomb force. The prominent ring boundary at r_d formed by these "turnaround" trajectories agrees well with what is observed experimentally -- unfortunately its location is difficult to derive analytically from the field and flow expressions. Nevertheless, its appearance is one of the more interesting phenomena in the microregion.

What do the trajectories look like outside the $\theta = 0$ plane? Figure 4.21 shows the top view of several trajectories entering from various values of θ. Trajectories with the same initial values of θ, but different initial values of z, are stacked upon one another in the figure. The numbers at the end of a given trajectory signify the value of z at that

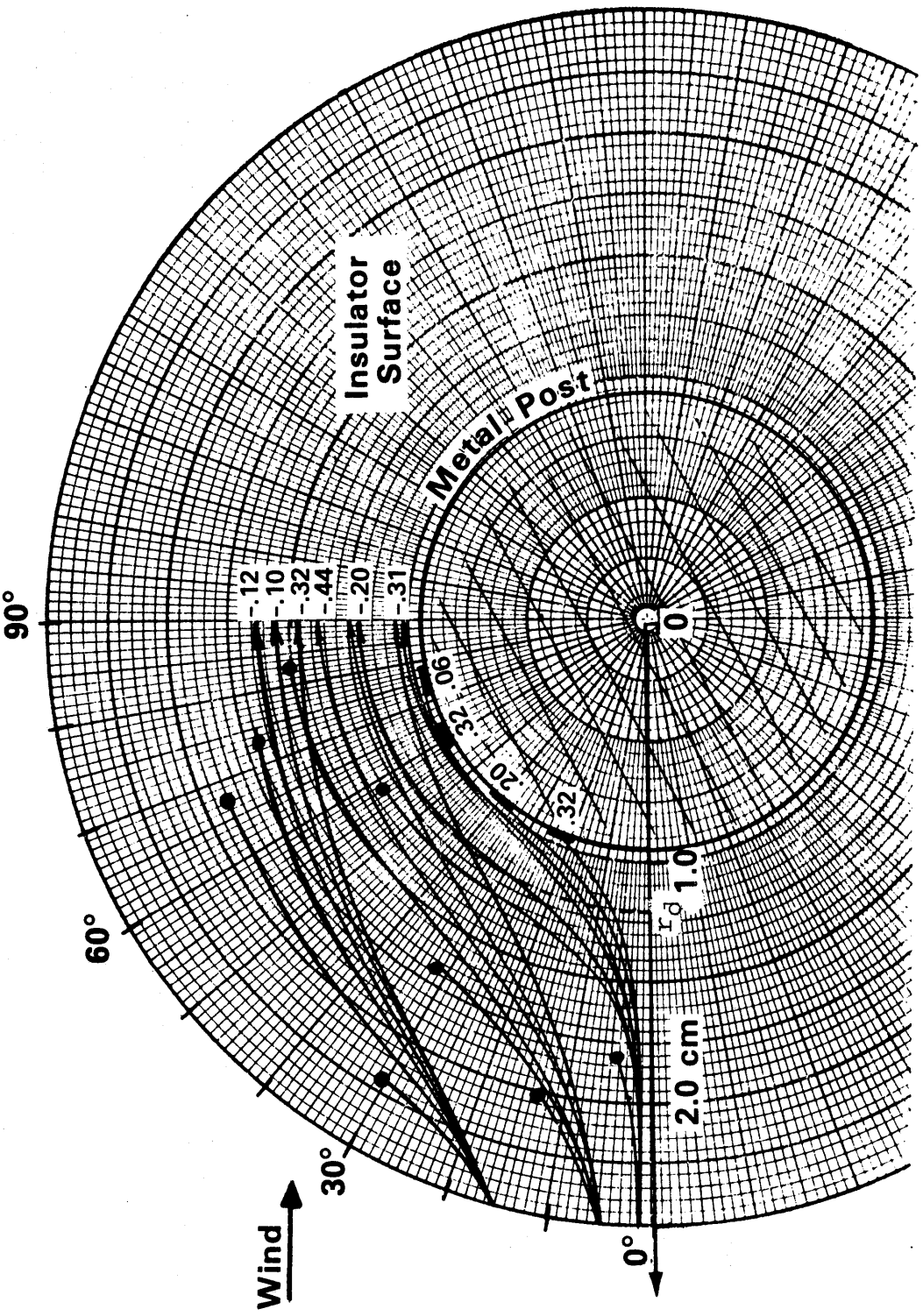

Fig. 4.21 Particle Trajectories from Top View (Attracted Particles). Numbers adjacent to trajectories signify value of "z". Dot and bar terminations signify deposition on the insulator and post surfaces respectively.

point, while dot and bar terminations signify deposition on the insulator and post surfaces respectively. Trajectories ending in arrowheads denote particles that blow past the insulator entirely. Evident in Fig. 4.21 is the fact that deposition on the post, even for nonzero values of θ, only takes place above z = 0. Likewise, no deposition takes place within the ring boundary anywhere on the disk. Many more trajectories must be computed to highlight lines of demarcation on the post and lower disk surface, but superimposing them on a single figure becomes cumbersome. It is much more efficient to examine the trajectory calculations by instructing the calculator to place a dot only at the endpoint of those trajectories terminating on the disk and post surfaces. Trajectories flowing completely past the insulator are ignored. In this manner the actual deposition process taking place on the insulator may be simulated. Figures 4.22 and 4.23 show the results of such a calculation for U = .25m/sec, $b = -5 \times 10^{-7}$ and -2.5×10^{-7} m^2/v-sec respectively, together with photos of actual insulator deposition patterns obtained in the test chamber. Agreement between the two generally appears good. Some discrepancy exists for both calculated mobilities in the deposition pattern on the post. The width of the calculated contamination band appears too thin in Fig. 4.22, but too wide in Fig. 4.23, as seen from the front view. The actual contamination band is more accurately replicated if the front view plots of Figures 4.22 and 4.23 are superimposed, so that

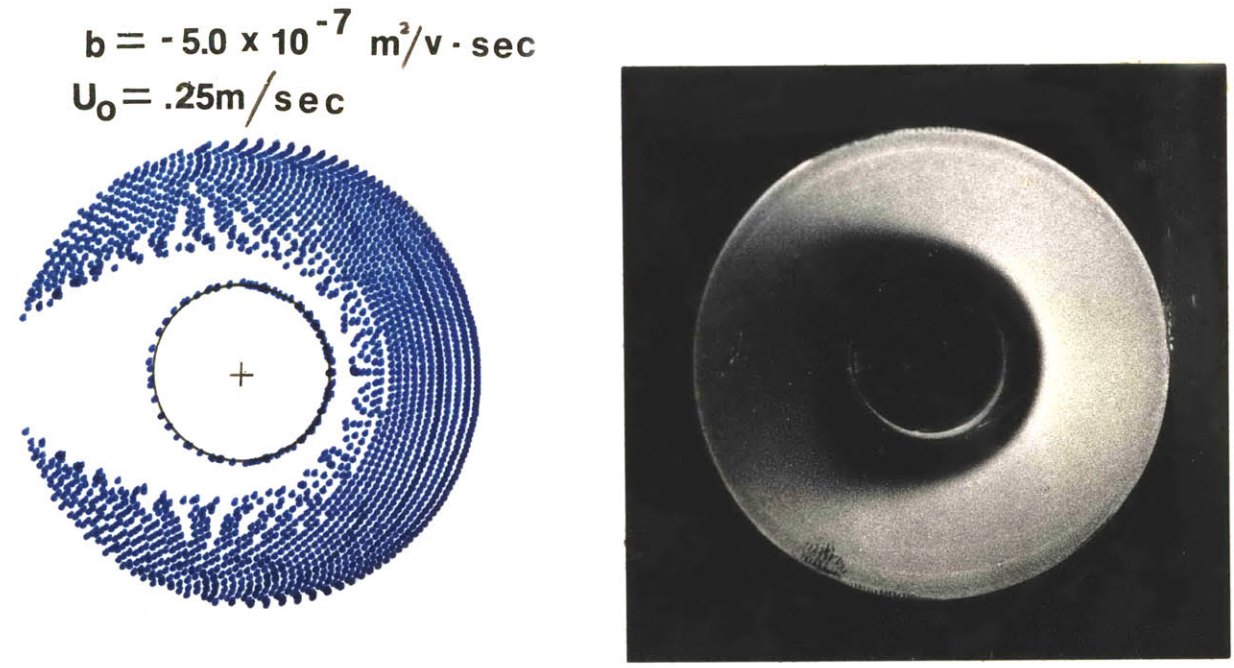

Fig. 4.22 Point Plots of Trajectory Calculations Compared to Actual Deposition Patterns. Wind is from the right. In the photos, illumination is uniform from all sides.

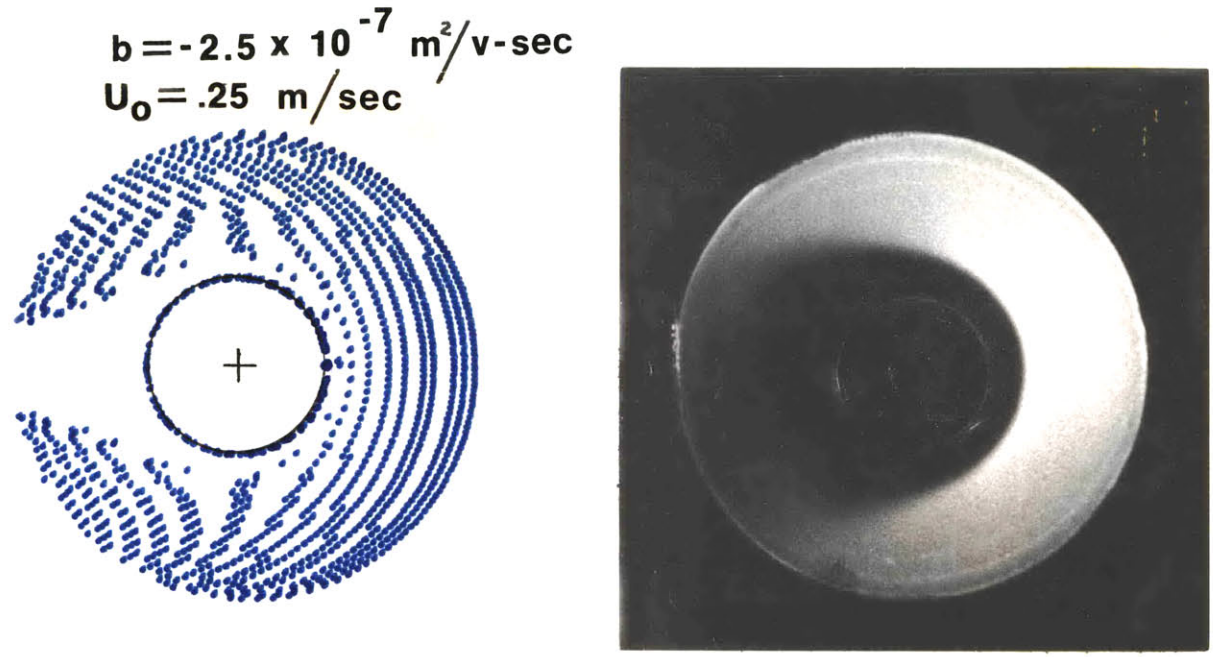

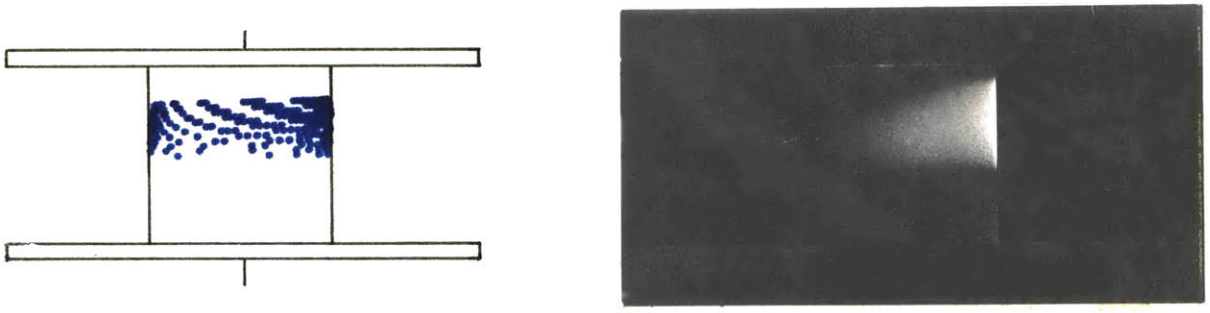

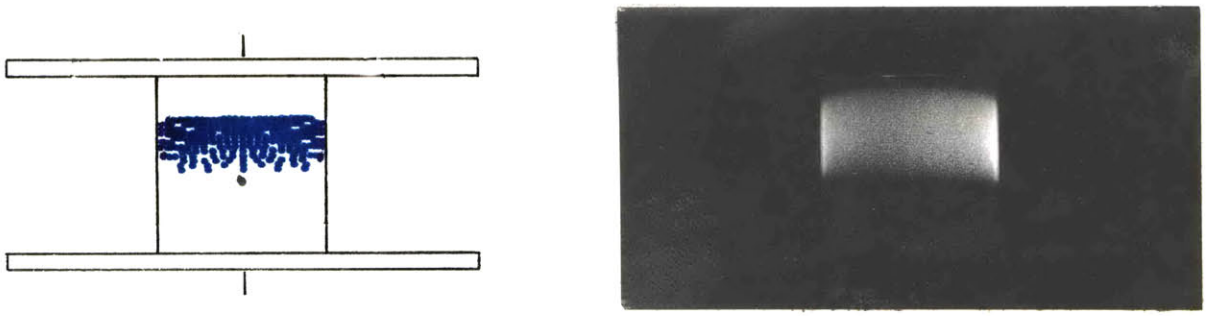

Fig. 4.23 Point Plots of Trajectory Calculations Compared to Actual Deposition Patterns. Wind is from the right. In the photos, illumination is uniform from all sides.

both mobilities are represented simultaneously. In the experiment, a spread of particle mobilities definitely exists, so this result seems reasonable.

In the experiment, the contamination band appears to taper to a triangular point toward the rear of the post, while the trajectory plots predict a much more rectangular formation. It must be remembered, however, that both turbulence and boundary layer separation from either the post or upper disk surface have been ignored. Any one of these phenomena could explain the observed tapering of the contamination band.

One final point must be emphasized in reference to Figs. 4.22 and 4.23. The density of dots on these plots does not denote the surface density of the contamination. The dots serve only to highlight the regions where deposition occurs, i.e., to outline the lines of demarcation. Within each shaded region, the flux of particles to the surface is given by $\bar{\Gamma} = -\bar{n}\cdot Nb\bar{E}$, so that the local surface mass density will be proportional to E_z. The density of dots changes in a given plot because it is related to the angle at which the contaminated surface intercepts the trajectory lines. For example, as the ratio of $\frac{U_o}{b}$ decreases in Fig. 4.20, the general angle of the trajectories to the horizontal increases also, so that for an array of particles with the same initial starting point spacing, the spacing of the intercepted points on the lower insulator surface gets smaller. Nevertheless, the net normal flux of particles to the surface is still the

same in each plot, and given by $-\bar{n}\cdot Nb\bar{E}$. What is different in each case is the speed with which the particles are transported to the surface: $|\bar{v} + b\bar{E}|$. Hence, in the case of the leftmost plot, for example, the intercept points are very spread out, but the particles arrive at a proportionately faster rate, so that the particle density along the trajectory lines, as stated by Eq. (4.7), does indeed remain constant.

Despite the minor discrepancies between predicted and observed deposition patterns, the trajectory model developed in this chapter successfully accounts for all of the observed microscopic deposition features, and can thus be viewed as a reasonably accurate description of the contamination process as it occurs on the microscale. This model will be used in the next chapter to justify a more practical, simplified contamination model that can easily be used in an engineering context.

CHAPTER 5

QUANTITATIVE COMPARISON BETWEEN THEORY AND EXPERIMENT

5.1 Confirming the Precipitation Model

The preceding chapter, in which the principles of particle motion were examined in detail, underlines one important conclusion: On a rigid solid surface, where the normal wind velocity must be zero, the deposition at the terminus of any particle line originating in a homogeneous particle source will solely be determined by the normal electric field and mobility and density of the incident particles. A careful examination of the deposition suggests that the normal electric field $E_\perp$ at the insulator surface is indeed a factor of major importance. The surface preference effect of Chapter 4, for example, is explained by the approximate field solution between two insulator disks found in Section 4.6. Suppose these insulators to be surrounded by a predominance of attracted particles -- say, negative particles around a positively energized line. The particles born by trajectories approaching the insulators would, upon reaching the solid surface, experience a coulomb attraction directed backwards against the field lines, thus depositing primarily on the top surface of the lower of the two insulators. A little thought will predict the same result for insulators energized with negative voltage, if the predominant particle charge is positive -- again an example of attracted particles.

The microtrajectory analysis of Section 4.7, and in particular the plots of Figs. 4.20 through 4.23, suggest that, except for minor variations in the radius of the clean ring and shape of the leeward wake, the deposition pattern on the insulator surface remains the same, as the ratio of the mobility-electric field product to wind velocity bE/U_o is changed. When contaminated insulators are measured by the UV detector, the minor variations that do occur in the deposition patterns are masked by the integrating nature of the detection method, leaving measurements representative of the average contamination on the insulator disk. If this average deposition depends only on the value of $\rho bE_\perp$ at the insulator surface, then two predictions result: The contamination should be proportional to the applied insulator voltage, but insensitive to changes in the ambient wind velocity. The preceding statements may be experimentally verified if one presumes the value of particle mobility to remain constant in the test chamber.

The results of a series of tests, in which varying line voltages were applied to the insulator string, are shown in Fig. 5.1. Note that changing the applied voltage by a given factor is tantamount to changing the normal electric field everywhere on the insulator surface by the same factor, because the electric field scales linearly with the voltage in the sub-corona regime. The particle mobility, wind velocity, and number of insulators on the string were all kept constant.

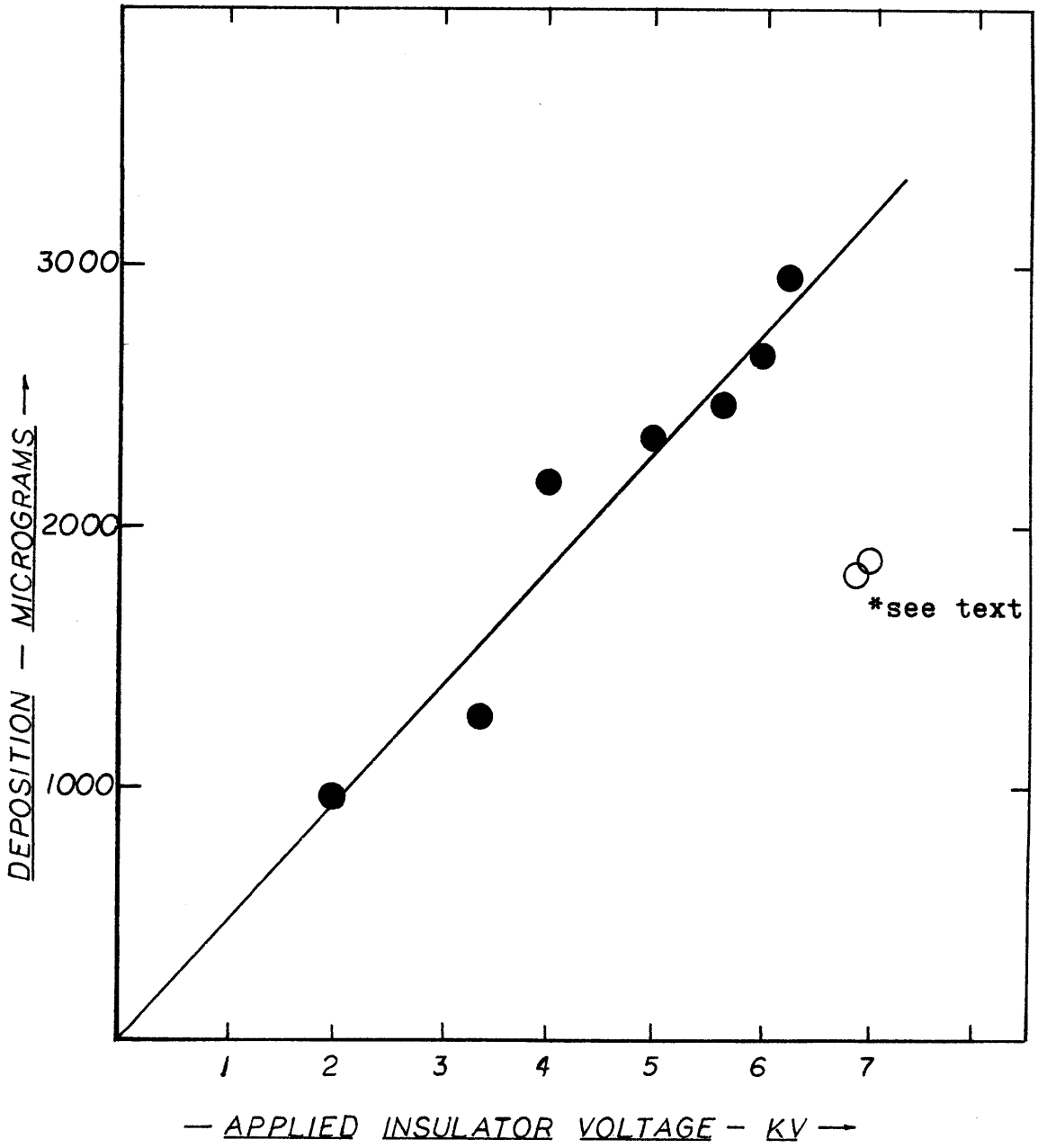

Fig. 5.1 Contamination vs. Applied Voltage
(Average Contamination per Insulator Disk)

Taken with negative particles and a positive line, these tests yielded only top surface deposition. The vertical axis in Fig. 5.1 represents the average deposition over all the insulators in the string, so that statistical variations, and the uneven distribution from the segregation effect, are smoothed out. Applied insulator voltage is taken as the line voltage divided by the number of units on the string. Deposition is also normalized to the standard calibration mass flow, as monitored by the filter paper method of Section 3.7.

Although the points in Fig. 5.1 form a less than perfect straight line, the expected trend is evident -- average contamination is indeed proportional to applied voltage. The obvious exception is the rightmost point, taken at a line voltage of 56 kV, or 7 kV per insulator. Because this data point was twice observed, statistical error is not a likely explanation. It is suspected that the onset of corona from the positive line or insulator disk edges, which could alter the charge on the negative particles, might be responsible for the decrease in contamination at this higher voltage.

The prediction that average contamination be insensitive to wind velocity was confirmed by running sets of identical tests at two different wind velocities, with the particle source panned to minimize any variations in contaminant distribution caused by source inhomogeneity. Plotted in Fig. 5.2 are the contamination distributions along the string taken at wind velocities of .2 and .4 m/sec. The contamination

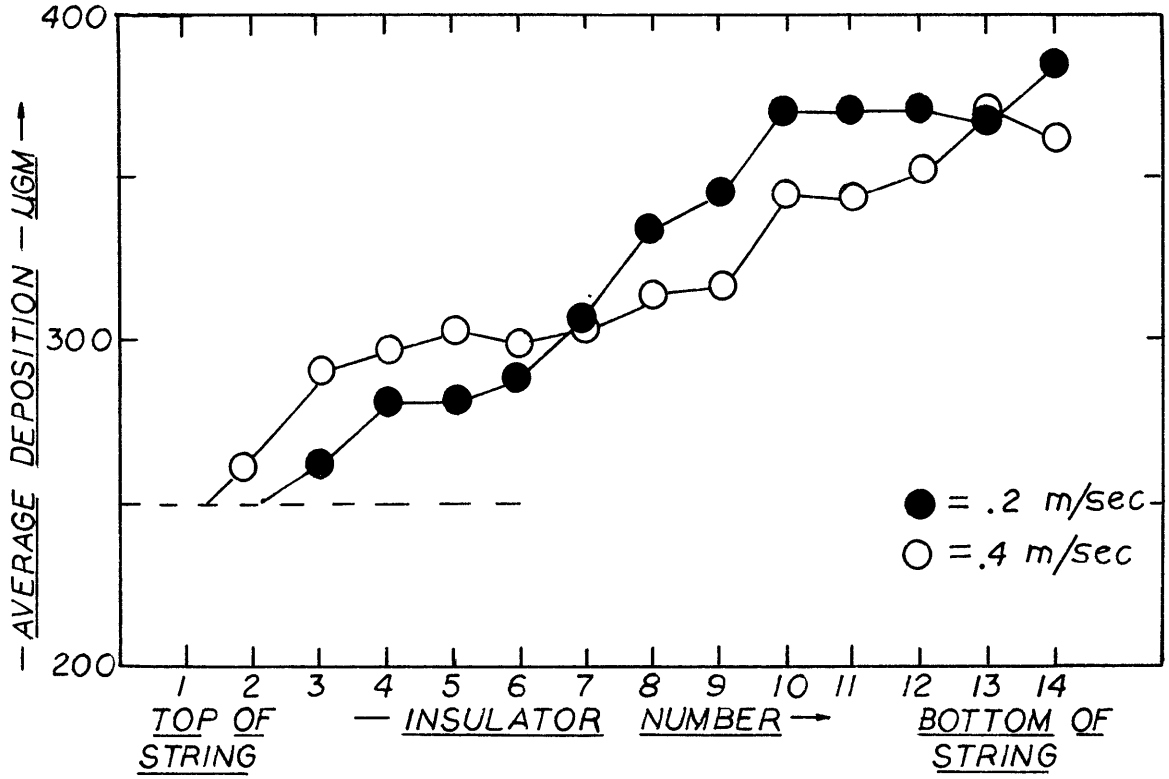

Figure 5.2 - Contamination Distribution for Two Wind Velocities

measurements on a given unit number are averaged over all tests taken at the same wind velocity. Although the two average contaminant distributions are not identical, their differences are slight--gross, major differences are not evident in the two plots of Fig. 5.2. We may thus presume, as predicted, that the contamination level is relatively insensitive to ambient wind velocity, provided that the velocity variations are not so great as to cause more than minor differences in the exact deposition patterns.

5.2 A Simplified Contamination Model

Data obtained in the test chamber can be used to verify what has now become a simplified contamination model. Suppose a given insulator is subjected to an ambient wind carrying particulate mass density ρ kg/m^3, where ρ is the mass of the particles contained in a cubic meter of air. Then, for a given surface area having a normal field $E_\perp$, the precipitation rate P per unit area will be given by:

$$P = \rho b E_\perp \quad \text{kg/m}^2\text{-sec} \tag{5.1}$$

where b is the mobility of the particles. Here, once again, the absence of contamination in the clean ring and leeward wake will be ignored when Eq. (5.1) is utilized to estimate the average surface contamination. It is convenient to average the normal field over the surface of the insulator to

obtain a representative precipitation rate. From the field solution of Section 4.6, we take the magnitude of the normal electric field E_z:

$$|E_z| = \frac{V_o}{2\ell} \frac{\ell n(\frac{r}{r_i})}{\ell n(\frac{r_o}{r_i})} \tag{5.2}$$

where V_o is the voltage across a given insulator. The average of $|E_z|$ over the insulator surface will be:

$$\langle E_z \rangle = \int_{r_i}^{r_o} \frac{|E_z|(2\pi r)\, dr}{\pi(r_o^2 - r_i^2)}$$

$$= \frac{\pi(\frac{V_o}{\ell})}{\pi(r_o^2 - r_i^2)} \int_{r_i}^{r_o} \frac{\ell n(\frac{r}{r_i})}{\ell n \frac{r_o}{r_i}} r\, dr \tag{5.3}$$

Note that the lower integral limit could be taken as the clean ring radius r_d if a more accurate estimate were desired. Performing the integral yields:

$$\langle E_z \rangle = \frac{\frac{V_o}{2\ell} r_i^2}{[\ell n \frac{r_o}{r_i}](r_o^2 - r_i^2)} [(\frac{r_o}{r_i})^2 (\ell n \frac{r_o}{r_i} - \frac{1}{2}) + \frac{1}{2}] \tag{5.4}$$

For $\frac{r_o}{r_i} = \frac{.0254}{.0095} = 2.67$, we get

$$\langle E_z \rangle = .654 \frac{V_o}{2\ell} \tag{5.5}$$

Thus, in terms of the total voltage V applied to the insulator string,

$$\langle E \rangle = .654 \frac{V}{2n\ell} \tag{5.6}$$

where 2ℓ is the separation between any two insulators and n is the number of insulators on the string.

Before the average electric field (5.6) and precipitation rate expression (5.1) can be applied to measurements taken in the test chamber, one must take note of the fact that the output of the fluidized bed particle injector is not constant in time. Rather, the value of ρ varies considerably both within a given test run, and also from test to test. This variation in ρ will likewise manifest itself in a variation in the precipitation rate P. It is therefore necessary to consider the time average precipitation rate:

$$\bar{P} = \frac{1}{T} \int_o^T \rho(t)\, bE_\perp \, dt \tag{5.7}$$

where T = collection time.

The above expression of course assumes b and $E_\perp$ to be constant in time. This time average precipitation rate

expression may now be put together with the surface averaged normal electric field, Eq. (5.6), to predict the average insulator contamination M (kg of deposition per insulator):

$$M = \bar{P} \cdot T \cdot A$$

$$= \left[\int_o^T \rho \, dt \right] \times .654 \, \frac{b \, V}{2n\ell} \, A \qquad (5.8)$$

where A = collection area of the insulator.

If one wishes to consider particles with a distribution of mobilities, the contamination may be computed by integrating over the spread of mobilities:

$$M = \int_o^T \int_{b_{min}}^{b_{max}} \rho(b,t) \, db \, dt \times .654 \, \frac{V}{2n\ell} \, A \qquad (5.9)$$

where $\rho(b,t)$ is now the time varying density of particles of a specified mobility "b". The mobility of the particles in the test chamber will be taken as single valued, although in any real situation a spread of mobilities will inevitably exist. Likewise, not every particle in nature will actually be charged, but for the laboratory experiments we assume each particle to be charged. From the measurements taken with the mobility analyzer, as summarized in Chapter 3, the average mobility may be estimated equal to 5×10^{-7} m^2/volt-sec.

The first expression in brackets in Eq. (5.8) will be

called the time average mass density-collection time product $\overline{\rho T}$. Its value in any given test can be inferred from the associated filter paper calibration mass, to which it is presumed proportional. This method of monitoring mass flow was described in Section 3.7, in which it was suggested that all contamination measurements be normalized to a standard calibration mass of 500 μgm. The Anderson inertial particle sampler may be used to measure the mass density-collection time product $\overline{\rho T}$ associated with the standard calibration mass. Let the volume sample rate of the Anderson be denoted "S" m^3/sec, and suppose at the end of a sampling run a mass "m" of particulate has been collected in the sampler. If the particle density is constant, then:

$$m = \rho TS \equiv \overline{\rho T} S$$

If ρ is not constant in time, then

$$m = \frac{1}{T} \int_0^T \rho(t)dt \; ST \equiv \overline{\rho T} S \qquad (5.10)$$

Table 5.1 lists the results of several particle samples taken with the Anderson sampler isokinetically in the plane of the insulator, and level with the neutralizer mouth through which the particles exit. Note that each sample reflects roughly the same particle size distribution, with the 4.7 and 3.3 micron sampling plates (plates 2 and 3) collecting the

Table 5.1

Measurements to Determine $\overline{\rho T}$ Product for Standardized Mass Flow

Trial	1	2	3	4	5	6
Collected Mass (Sum of Plates 2 and 3) - μgm	370	735	1490	2575	4795	6465
Actual Total Mass - μgm (all plates)	m = 635	1395	2795	4635	8290	11180
Normalized Total Mass - μgm (see text)	$\bar{m}$ = 3921	4337	4286	4113	3950	3951
Normalized $\overline{\rho T}$ product (in units of 10^{-3} kg-sec/m^3)	8.31	9.19	9.08	8.71	8.37	8.37

$$\text{Normalized } \overline{\rho T} = \frac{\bar{m}}{S} = \frac{\text{total mass collected}}{\text{sample flow rate}}$$

$$S = \text{Sample Flow Rate} = 1 \text{ CFM} = 4.72 \times 10^{-4} \text{ m}^3/\text{sec}$$

greatest mass of particles (to be expected with our nominal particle diameter of 4 microns). Unfortunately, most of the samples listed in the table were taken before the filter paper sampling method for monitoring mass flow was developed. Hence a much more roundabout method is needed to compute the standardized $\overline{\rho T}$ product from Eq. (5.10).

In Chapter 3, the ratio "α" of calibration mass to the sum of the collection weights in micrograms on plates 2 and 3 was determined to be $\alpha = .22$ (see Table 3.3). Hence, for the standard calibration mass of 500 μgm, one expects a total of 500/.22 = 2280 μgm on plates 2 and 3. The mass collection entries in Table 5.1 may thus be normalized to reflect any deviation from this value. The final entries for equivalent mass density-collection time product in the table are thereby also normalized to the standard calibration mass of 500 μgm, even though the actual calibration mass may have been very different had one been measured along with the Anderson particle sample. Based on the final data in Table 5.1, we may select the standard value for $\overline{\rho T}$ of 8.67×10^{-3} kg-sec/m^3.

This standard value for $\overline{\rho T}$ may now be put into the deposition equation (5.8) to predict the deposition per kilovolt on a given insulator for this simplified contamination model:

$$M = (\overline{\rho T})\ \frac{.654\ b}{2\ell}\ \frac{V}{n}\ A = (8.67\text{x}10^{-3})\ \frac{(.654)}{(.019)}\ (5\text{x}10^{-7})\ (1000)\ \pi\ (.0254^2 - .0095^2)$$

$$M \cong 2.60 \times 10^{-7}\ \text{kg/kV} \equiv 260\ \text{micrograms/kilovolt} \qquad (5.11)$$

The actual deposition per kilovolt observed in the test chamber may be inferred from Fig. 5.1 to be approximately 470 μgm. This value is a factor of 1.8 greater than that predicted by Eq. (5.11). The suspected source of error is twofold. First, the measurements of $\overline{\rho T}$ reflected in Tables 5.1 and 3.3 were performed with neutral particles, and without the line conductor energized. When charged particles are present in the test chamber, they must pass through the metallic honeycomb channels before depositing on the calibration filter paper disk, and some of them may self-precipitate on the honeycomb surface. In an insulator test, the calibration masses would thus underestimate the true value of $\overline{\rho T}$, resulting in erroneously high normalizations for the measured contamination.

Secondly, one must realize that two important components of Eq. (5.11), b and $\overline{\rho T}$, can each vary over orders of magnitude in the experiment, and precise measurements of them are normally exceedingly difficult to obtain. Hence agreement in this experiment between predicted and measured contamination to within better than a factor of two is to be considered satisfactory. As a tool for evaluating insulator performance on actual transmission lines, and for designing dc insulators where contamination estimates are sufficient, the simplified contamination model represented by (5.11) appears quite useful and accurate.

5.3 Origin of Observed Particle Segregation

In Section 4.5, the deflection of charged particles out of the airstream by the electric field was shown to be minimal for the values of b and U_o used in the scale model experiments. How likely is it that significant deflections will ever be encountered, either in the model experiments or in the real world? The electric field strengths in the vicinity of the model line conductor and insulator string are scaled to resemble those found around an actual line. Higher fields will seldom appear on either the model line or actual lines, because attempting to increase the field strength by very much more will result in corona discharge around the line conductor, which will limit the established field at the conductor surface to at most Peek's field $\sim 3 \times 10^6$ V/m. (23)

Values of particle mobility higher than those used in the experiment might in some situations be found around a real line. Particles of 4 micron diameter, for example, could in theory have a saturation charge* as high as $q_{sat-max} = 12\pi\varepsilon_o R_p^2 E_{peek}$, leading to a mobility on the order of 6×10^{-6} m^2/v-sec. Particles of larger diameter, although capable of accepting more charge before saturation, would also experience more wind drag, so that at saturation:

$$b_{max} = \frac{q_{sat\ max}}{6\pi\eta R_p} = \frac{12\pi\varepsilon_o R_p^2 E_{max}}{6\pi\eta R_p} = \frac{2\varepsilon_o}{\eta} R_p E_{max} \qquad (5.12)$$

*(See Appendix A for discussion of particle charging).

The theoretical maximum mobility thus increases with the radius for larger particles. For a 10 micron particle, representing the upper bound of particle size considered in this work, $b_{max} \sim 1.5 \times 10^{-5}$ $m^2/v\text{-sec}$. As discussed in Chapter 2, scaling such a particle in the model experiment requires a mobility l_a/l_m higher, i.e. 7.5×10^{-5} $m^2/v\text{-sec}$. This value of b exceeds the one used in the macroscopic analysis of Section 4.5 by a factor of about 100. Reference to Eqs. (4.18) and (4.23) shows that such particles approach the domain where large scale deflections might be observed.

More than likely, however, the values of mobility actually found around transmission line sites will be very much lower than such hypothetical absolute maximum values. The value of b used in the experiment is really more typical of natural mobilities, and significant large scale deflection should in most cases not be expected around actual transmission lines.

Nevertheless, even on the scale model system, where major deflections definitely do not take place, the segregation of attracted and repelled particles to lower and upper regions of the insulator string is consistently observed in the experiments. Figure 5.3, for example, shows the measured contaminant distributions for both attracted and repelled particles, taken for a typical set of test parameters. What mechanism could be responsible for this observed phenomena? The microfield analysis has heretofore assumed the electric

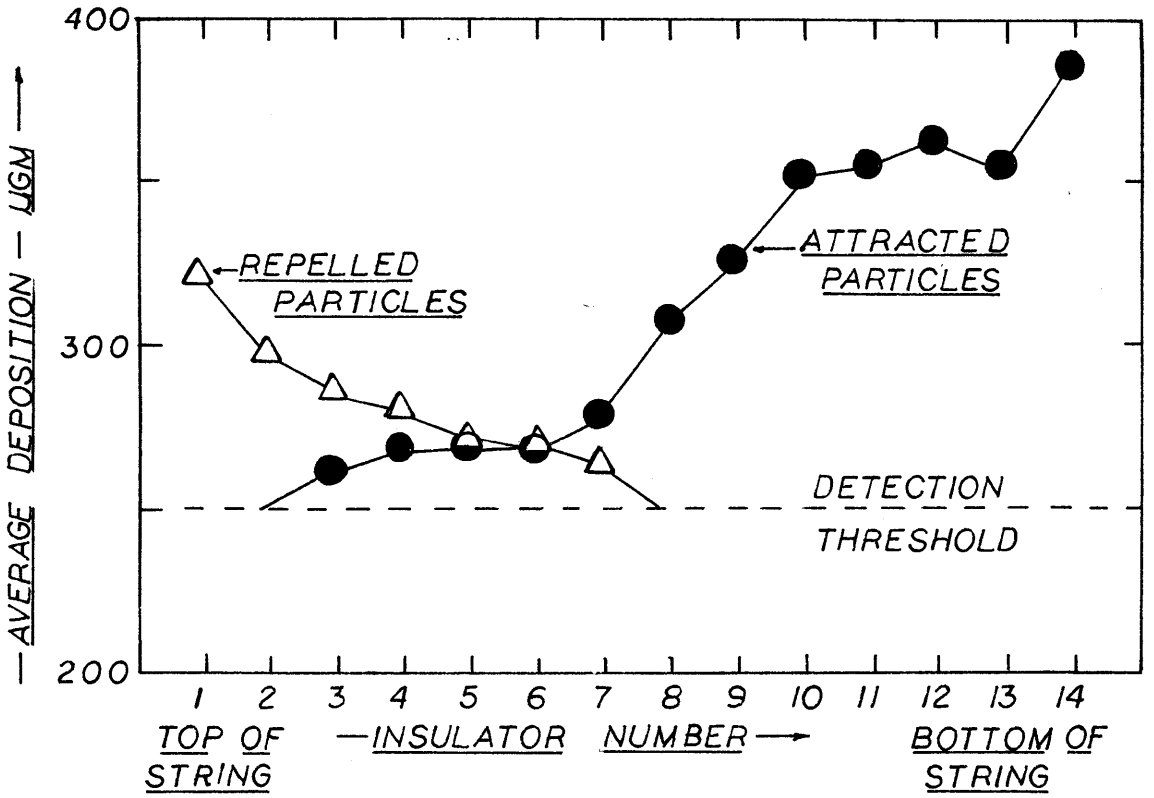

Fig. 5.3 Contamination Distributions for Attracted and Repelled Particles Measured in Test Chamber.
U_o = .2 m/sec b = 5 x 10^{-7} m^2/v-sec
Particle Source was Panned

field existing between any two insulator disks to be the same, regardless of the relative position of the insulators along the string. In fact, we know this assumption cannot be quite true. The macrofield analysis of Section 4.4, which models the insulator string as a solid cylinder with a linear surface potential distribution, demonstrates the existence of a component of electric field radial to the axis of the insulator string. Were the insulator string to actually be a solid cylinder, this radial component of electric field would simply terminate on the cylinder surface. The actual insulator string is not a solid cylinder, but nevertheless still imposes a linear potential distribution along its length; hence it will generally invoke a radial field component also. This radial field component, however, must now terminate on the insulator skirt edges. Because the insulator disks are thin, the concentrated fields at the edges may become high enough to significantly perturb the trajectories of nearby particles. At the same time, the magnitude and sign of these edge fields will vary as one goes from the upper end of the string to the lower end. An analysis of this situation is therefore in order.

The problem may first be approached qualitatively. In Section 4.4, the macrofield analysis identified the point along the surface of the solid cylinder where the imposed linear potential distribution of the cylinder crosses what would otherwise be the logarithmic potential distribution of

the line conductor. It was shown then that this crossover point, henceforth to be called "z_c", represents the critical point where the normal field component on the cylinder surface changes sign. If the insulator string were indeed a solid cylinder, particles could only deposit, as discussed in Section 4.3, where the sign of $\bar{n}\cdot b\bar{E}$ was negative. For repelled particles for example, the sign of $\bar{n}\cdot b\bar{E}$ would be negative above z_c, and positive below it. Hence repelled particles would only deposit above z_c. The reverse situation would be true for attracted particles - i.e. they would only deposit below z_c.

An examination of the distributions of Fig. 5.3 suggests that, even though the skirt edges do not constitute a rigid solid surface, the deposition follows the same trend expected of a solid cylinder, i.e. deposition of attracted and repelled particles is still generally limited to regions below and above z_c, respectively. One suspects that the radial field components (i.e. the fringing fields) that terminate on the skirt edges, which also change sign at z_c, perturb the microdeposition process to a degree sufficient to lead to particle segregation. Experimental evidence that the fringing fields are important is offered in the example of Fig. 5.4, which shows close-up sketches of the deposition of attracted particles, as actually observed at the edges of various disks along the insulator string. (Technical problems make the photographing of these edge depositions

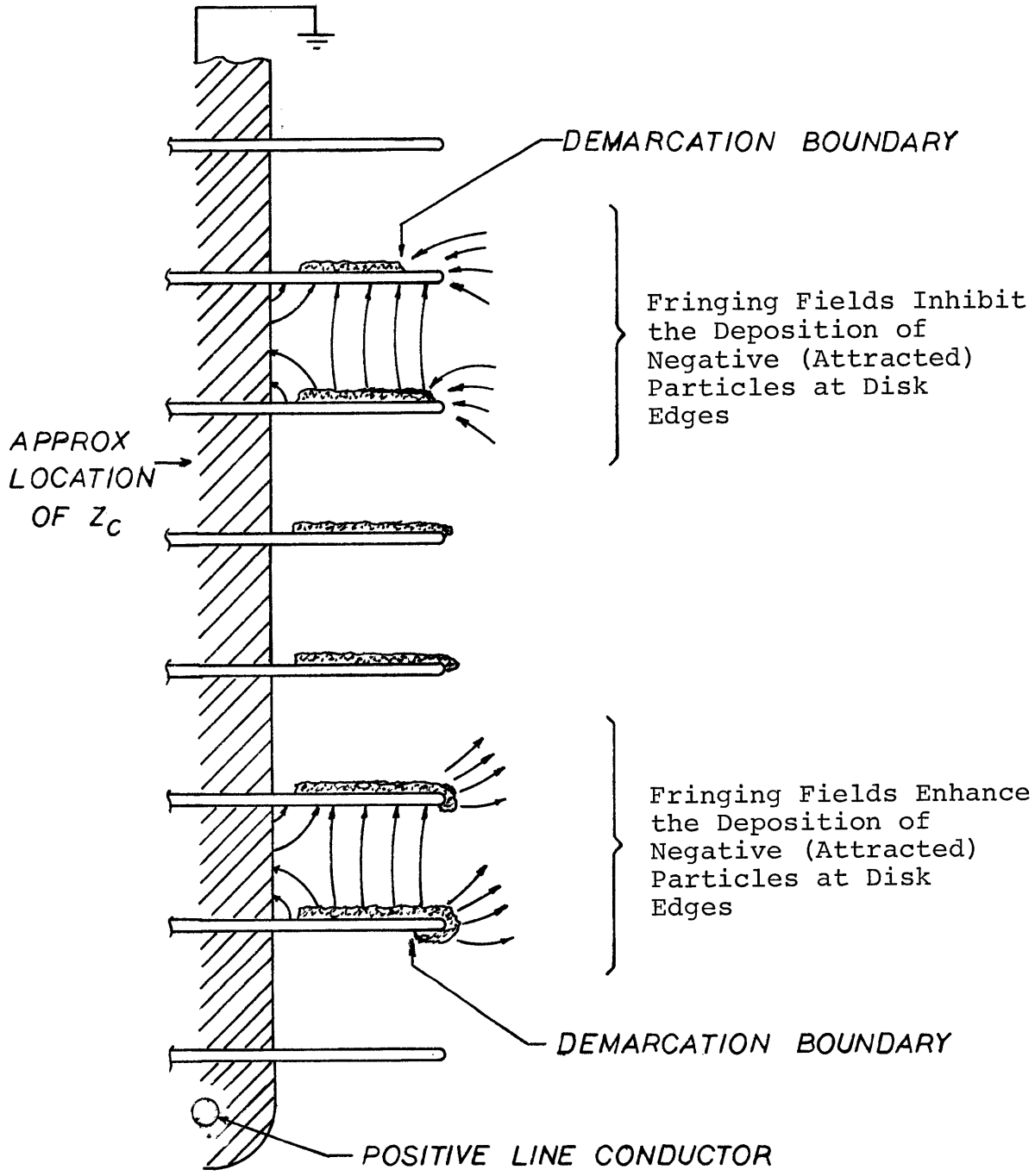

Fig. 5.4 Sketches of Deposition as Observed at Edges of Insulators. Negative Particles Around Positive Line Conductor (Attracted Particles).

difficult). As is evident by the observations sketched in Fig. 5.4, the outer demarcation boundary of the expected top surface deposition begins to curl under the disk edges of insulator units located below z_c. On insulators further up the string, the demarcation boundary begins to retract around the disk edge, eventually moving inside the microregion. The location of the demarcation ring boundary is determined by the place on the disk edge surface where the normal component of electric field passes through zero. Below z_c, the fringing fields enhance the microfield at the disk edges, so that this zero crossing point is extended over the disk edges. Above z_c, the fringing fields reduce or even reverse the microfield at the disk edges, thus inhibiting deposition on the disk edges. Clearly, the fringing fields have an effect on the deposition process; hence it is in order to seek a way to model these fields.

In Section 4.4, the charge simulation technique was used with point charges to approximate the macroscopic field. In principle this technique could also be used to model the entire field about the insulator string,including the macroregion, the microregion, and the fringing fields of the intermediate region. Such a simulation, however, would require an extraordinary number of external charges, and would be of questionable value. How well must we know the entire field distribution? Experimentally, the microdeposition patterns that do occur in a given situation appear identical to the

patterns of Section 4.7, suggesting that once inside a given microregion, a particle follows the trajectories described by the microregion analysis of Section 4.7 -- i.e., the fringing fields constitute only a perturbation at the macro-micro boundary, and not a major distortion to the microfield. A successful prediction of the segregation phenomena can thus be gotten by simulating the fringing fields as seen only on the macroscopic side of the macro-micro boundary (i.e. ignoring them inside the microregion), and examining how they limit or enhance entry of particles into the microregion at the various insulator locations.

One approach to the modeling of the fringing fields in this manner is to place charged toroids of appropriate potential at the outer edges of the insulator skirts, and to examine the fields at the macro-micro boundary. Qualitatively, one might argue that the small radius of these toroids should match the disk edge thickness; hence the toroids will have a small ratio of minor radius to ring radius. The fields from them will thus approach those of ring charges of the same large diameter.[20]

A detailed analysis[21,30] shows that, for a ring charge of radius r_q and total charge q, the potential and field components are given by:

$$\Phi(r,z) = \frac{q}{4\pi\varepsilon_o}\ \frac{2}{\pi}\ \frac{K(k)}{\alpha}$$

$$E_r = \frac{-q}{4\pi\varepsilon_o}\ \frac{1}{\pi r}\left[\frac{(r_q^2 - r^2 + z^2)\ E(k) - \beta^2\ K(k)}{\alpha\beta^2}\right]$$

$$E_z = \frac{q}{4\pi\varepsilon_o}\ \frac{2}{\pi}\left[\frac{z\ E(k)}{\alpha\beta^2}\right] \qquad (5.13)$$

where $\alpha = [(r + r_q)^2 + z^2]^{1/2}$

$$\beta^2 = [(r - r_q)^2 + z^2]$$

$$k = \frac{2\ \sqrt{r\ r_q}}{\alpha}$$

and K(k) and E(k) are the complete elliptic integrals of the first and second kind. The above expressions (5.13) are complicated, but not unwieldy, and likewise are in convenient cylindrical coordinate form.

If the magnitudes of these ring charges are appropriately chosen, a charge simulated macrofield very similar to the one obtained with external point charges can be obtained. In essence, this simulated macrofield will contain the information about the radial electric field components that we seek to model here. While the radial field components of the point-charge-simulated field cross the cylindrical boundary surface everywhere along the cylinder length, they will be concentrated at the insulator skirt edges when external ring

charges are used.

The current problem thus focuses on "splicing" the microregion to the macroregion, and appropriately selecting the cylindrical boundary surface separating them. Let a new cylindrical boundary surface be defined, as in Fig. (5.5), which just touches the edges of the insulators at the radius r_t of the hypothetical toroidal surfaces. By so displacing the old cylindrical boundary surface, the locations of the ring charges are never intersected. The potential of the new boundary surface is still assumed to vary more or less linearly in going from the bottom of the string to the top. Once again, thirteen external charges are selected to simulate the field. This time, however, the ten point charges located on the insulator axis are replaced with ring charges, whose proper magnitudes are selected by the same process used to compute the external point charges. The points z_p at which the potential is to be exactly matched are chosen as $z_p = z_n$ on the boundary surface at $r = r_q + r_t$, i.e., the outer edge of each torus where it touches the cylindrical boundary surface in the plane perpendicular to the line conductor.

Equation (4.12), which describes the "ideal" potential along the boundary applies to this ring charge simulation also. The linear equations (4.14a) are thus again to be solved:

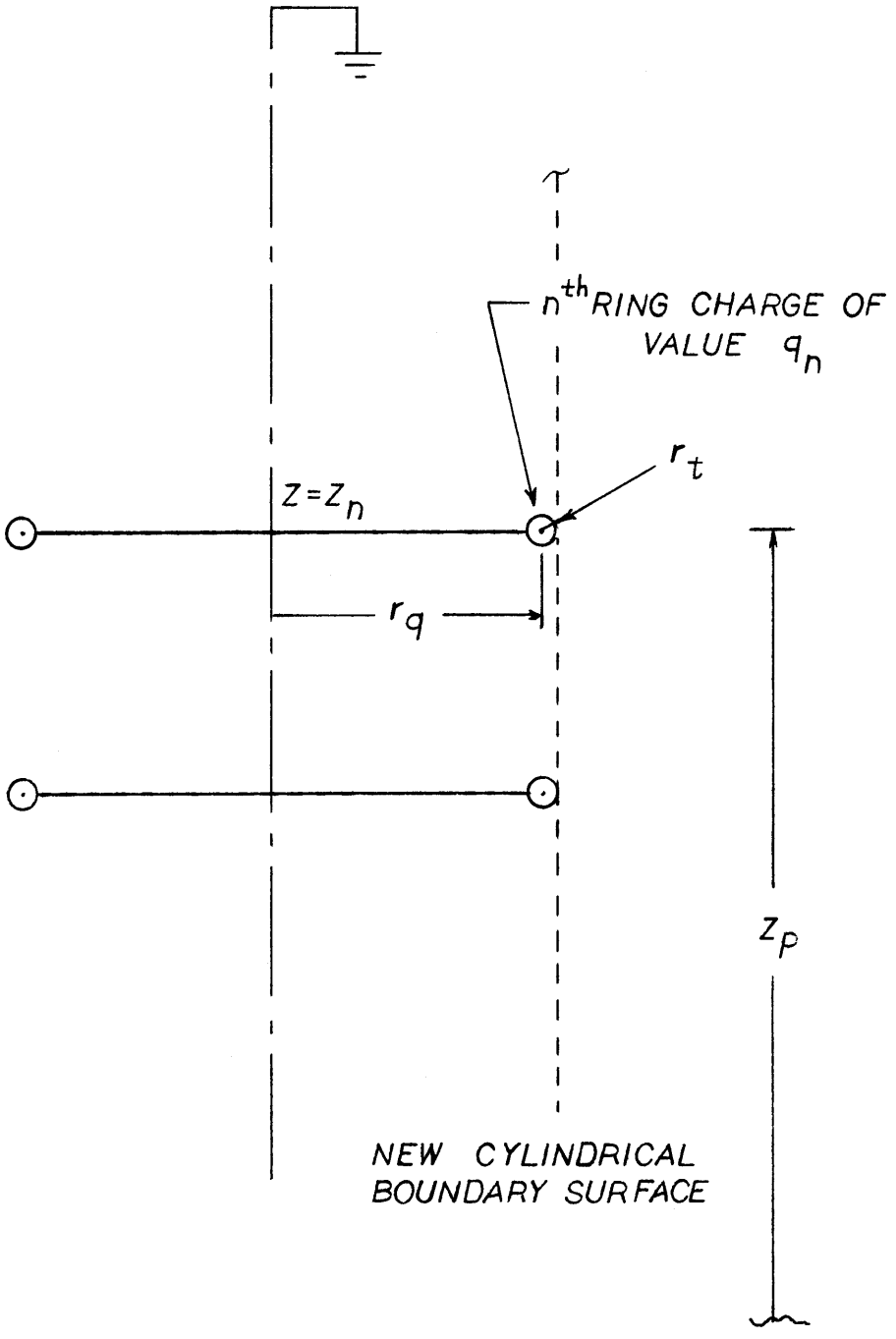

Fig. 5.5 Coordinate System for Ring Charge Simulation Problem

$$\sum_{n=1}^{13} A_{pn} \frac{Q_n}{V} = B_p \qquad p=1,\ldots,13 \qquad (5.14)$$

In this case, however, the first ten coefficients A_{pn} must now reflect the potential of the ring charges, rather than the point charges formerly located on the insulator axis:

$$A_{pn} = \frac{2}{\pi} \frac{K(k)}{\alpha} \Bigg|_{\substack{z=z_p \\ r=r_q + r_t}} \qquad p=1,\ldots,10 \qquad (5.15)$$

The remaining three A_{pn} still reflect the potential of point charges left along the ground post, and are given as before by Eq. (4.14c).

Solving the equations (5.14) leads to the values of q_n listed in Table 5.2. Figure 5.6 shows a plot of the potential due to the ten ring charges, plus three point charges and line conductor taken along the cylindrical boundary surface in the plane perpendicular to the line conductor. This plot is similar to Fig. 4.11, except that the simulated potential no longer matches the "ideal" potential in the intermediate space between each pair of insulators. This result is to be expected, given the field concentrations now being modeled at the disk edges.

It is important to note that the macrofield simulated by the ring charges listed in Table 5.2 is not valid inside

Table 5.2

Solution for the Ring Charge Values in the Ring Charge Simulation Problem

Point Charges:	q_{13}	=	-2.34	x 10^{-10}	coulombs/kv
	q_{12}	=	-2.53	x 10^{-10}	
	q_{11}	=	-4.06	x 10^{-10}	
Ring Charges:	q_{10}	=	-3.09	x 10^{-10}	
	q_9	=	-1.40	x 10^{-10}	
	q_8	=	-0.568	x 10^{-10}	
	q_7	=	.0738	x 10^{-10}	
	q_6	=	.649	x 10^{-10}	
	q_5	=	1.20	x 10^{-10}	
	q_4	=	1.73	x 10^{-10}	
	q_3	=	2.27	x 10^{-10}	
	q_2	=	2.84	x 10^{-10}	
	q_1	=	4.63	x 10^{-10}	

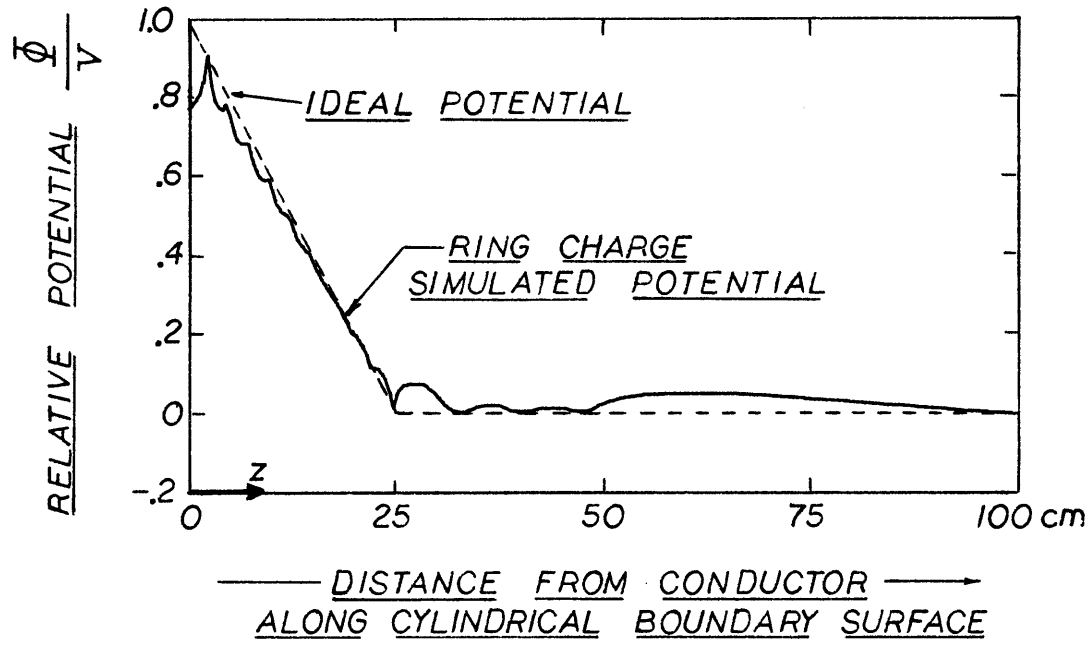

Fig. 5.6 Potential Due to External Ring Charges vs. "Ideal" Potential Along Cylindrical Boundary Surface

the cylindrical boundary surface, i.e. inside the micro-region. Although the potential distribution along the boundary surface is also assumed to be linear in the development of the microfield, a discontinuity in the field component radial to the insulator axis exists between the respective macro and microfield solutions. Hence simply combining the two solutions falls short of describing the total field around the insulator string.

With this shortcoming in mind, a useful model can nonetheless be developed for explaining how the particle trajectories are perturbed by the fringing fields. Figure 5.7 depicts the trajectories of repelled particles incident on the macro-micro boundary. In the upper plot, taken above z_c, the particles have the opposite sign of the ring charges, and are thus deflected toward the insulator disk edges. As is evident in the figure, all regions of the macro-micro boundary are thus accessed by trajectory lines and we should expect the contamination of these insulators to be very similar to that predicted by the simple microtrajectory analysis of Section 4.7. In the lower plot, on the other hand, the particles have the same sign as the ring charges, and are thus deflected toward the central area of the boundary between the disks before entering the microregion. The disk edges, in effect, establish two "umbrellas" which shield much of the microregion from the entering particles. The microtrajectory analysis of Section 4.7 shows that particles entering the

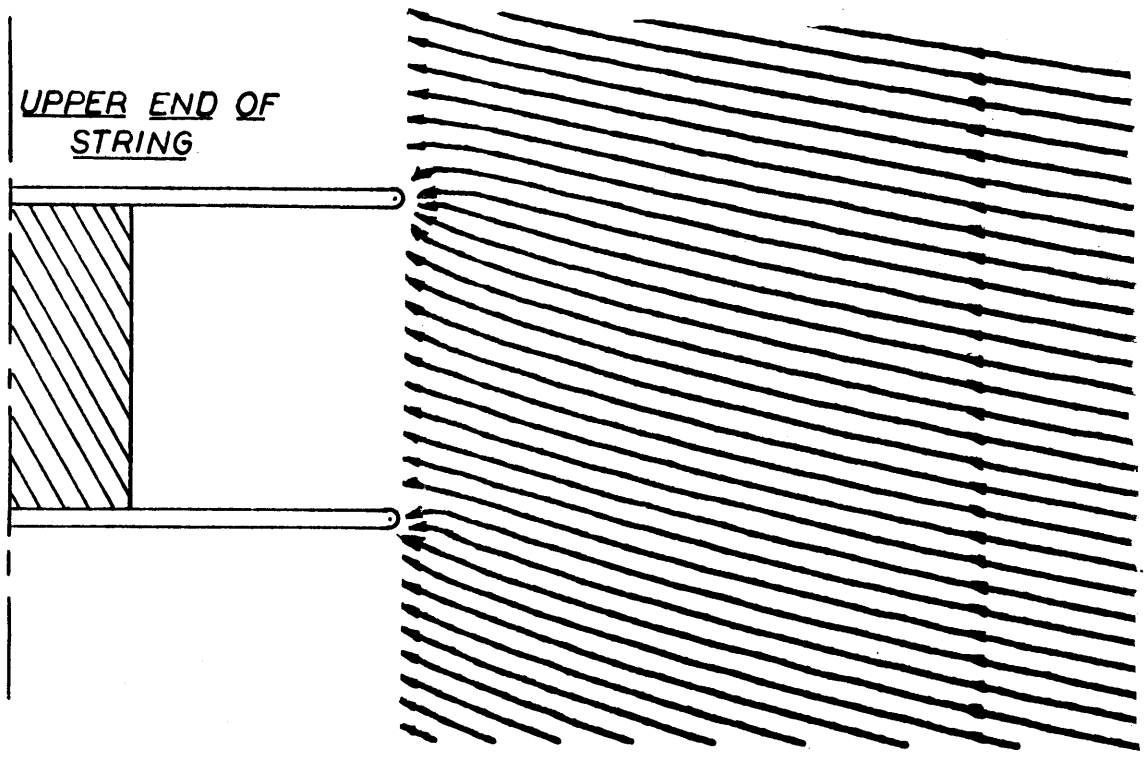

Fig. 5.7 Perturbed Trajectories for Repelled Particles

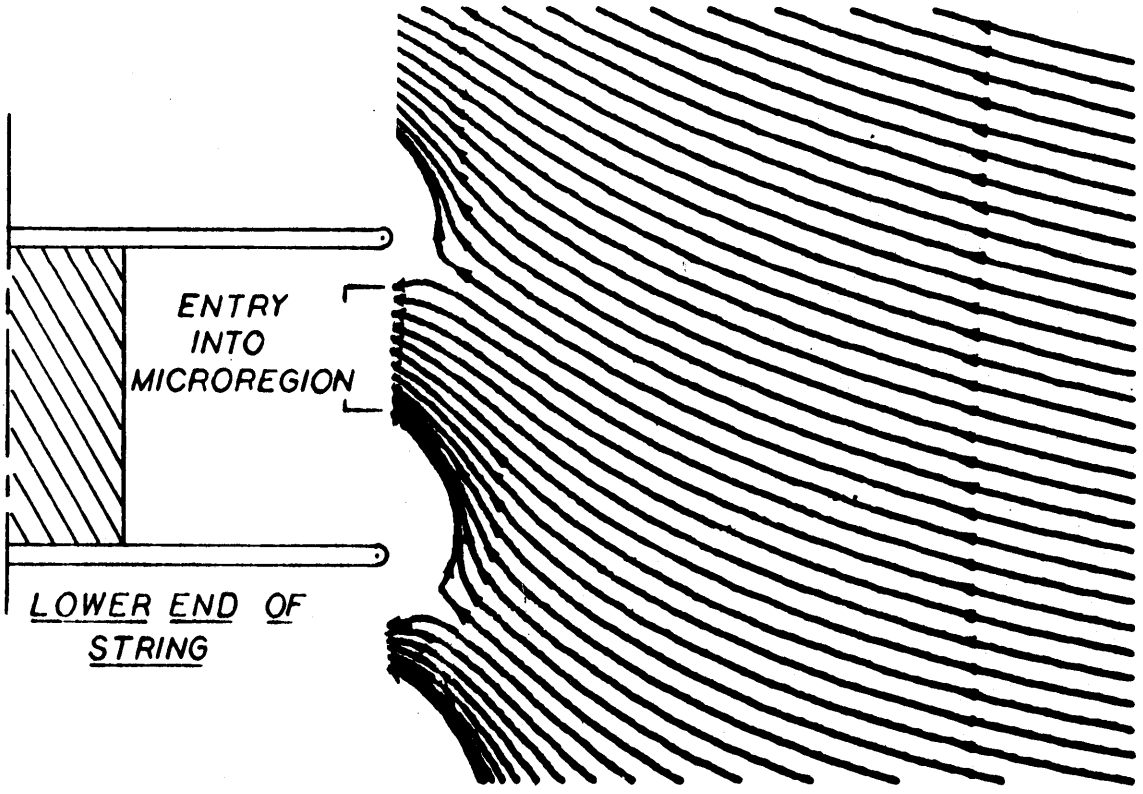

microregion in this central area tend to sweep past the insulator before experiencing enough downward deflection to hit the lower insulator surface. Particles entering the microregion close to the disk edges--regions which are shielded from particles in the lower plot--tend to deposit on the metal post and lower insulator surface, respectively. It is reasonable to expect, therefore, that the insulators in the lower plot in Fig. 5.7 will experience very much diminished contamination.

Figure 5.8 is similar to Figure 5.7, except that in this case the particles are attracted particles, and are thus repelled from the disk edges around the upper insulators. The ring charges representing the insulators above z_c are smaller in magnitude than those found closer to the line end of the string, so the widths of the shielding "umbrellas" are smaller, and more particles enter the microregion. Hence the degree to which these upper insulators will experience diminished contamination will not be quite as severe as in the case of the lower insulators of Fig. 5.7.

In the simulations represented by the plots of Figs. 5.9 and 5.10, the trajectories of particles initially in a uniform array far from the string were calculated up to the macro-micro boundary using the ring charge simulated macrofield and laminar wind flow expression (4.30). Inside the microregion, the particle trajectories were calculated as in Section 4.7, using as starting points the trajectory entry

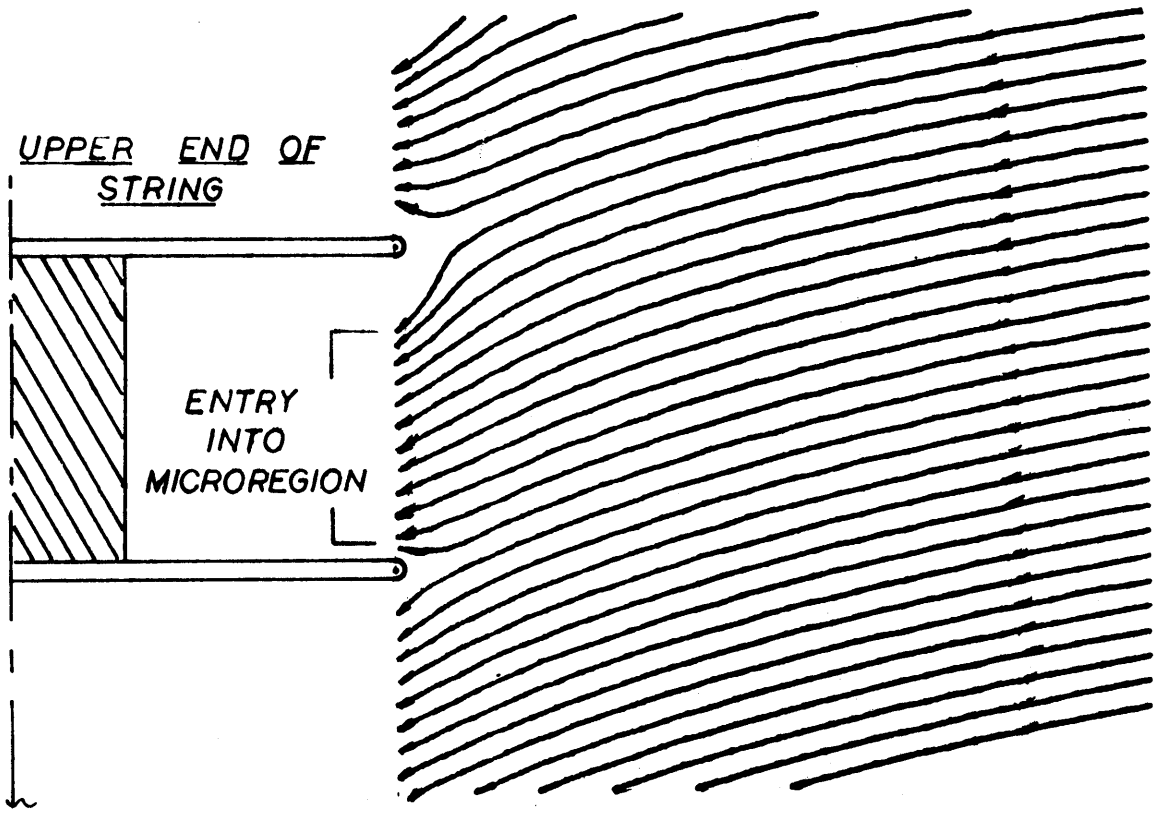

Fig 5.8 Perturbed Trajectories for Attracted Particles

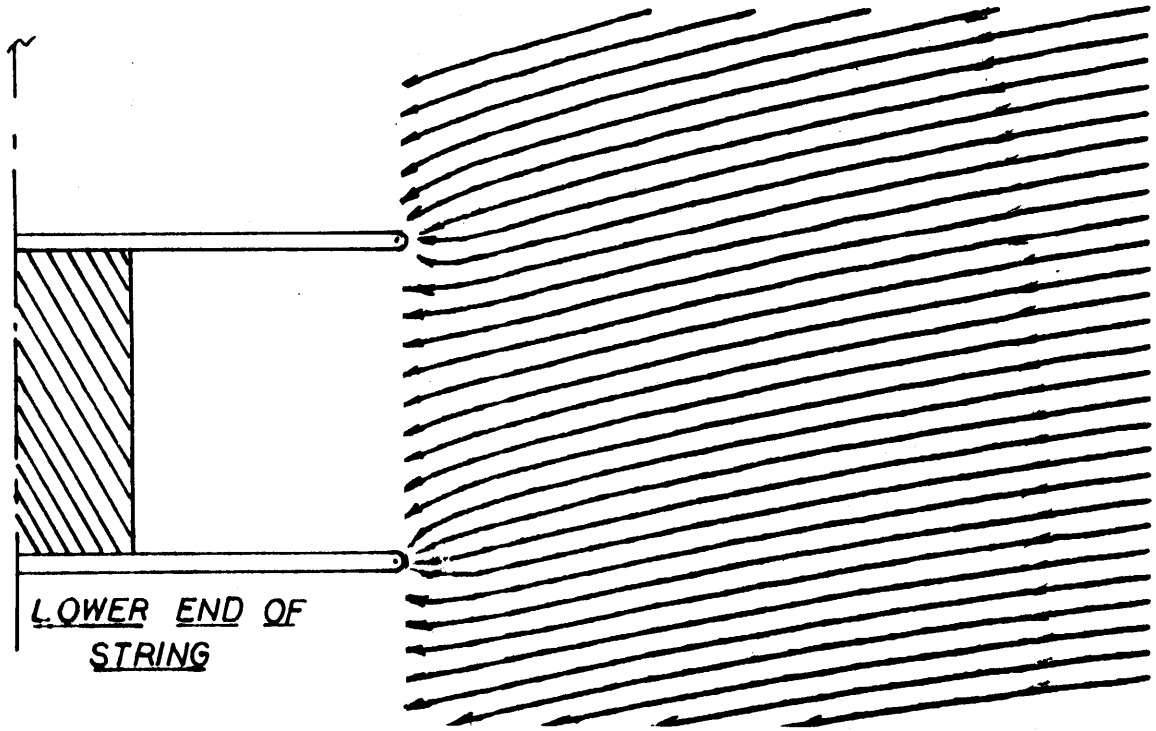

points from the macroregion. Once again, the dots in Figs. 5.9 and 5.10 signify the endpoints of trajectories terminating on the insulator surfaces.

A general trend is evident in these figures. In particular, the attracted particles of Fig. 5.9 show a marked decrease in contamination above z_c, while the repelled particles of Fig. 5.10 show a significant decrease in contamination below z_c. This trend is consistent with the experimental observations discussed earlier, and can be understood by again referring to the discussion of Figs. 5.7 and 5.8.

The plots of Figs. 5.9 and 5.10 can be used to quantify this observed trend. Each patch of dots denotes a region where trajectories terminate on the insulator surface, and the edges of the patches correspond to lines of demarcation on the insulator surface. The contamination flux on these areas is thus once again equal to $-\bar{n}\cdot Nb\bar{E}$, so that by estimating the area of each shaded region and the magnitude of E_z within it the net relative mass contamination on each insulator in the simulation can be computed. In practice this computation is performed on each individual plot in Figs. 5.9 and 5.10 by dividing the insulators into thin concentric rings, inside of which the local value of $E_z(r)$ for that radius is calculated from the microscopic field expression, Eq. (4.29). The angular fractions of all ring areas that are shaded are then multiplied by their respective values of E_z and added together to give the total relative

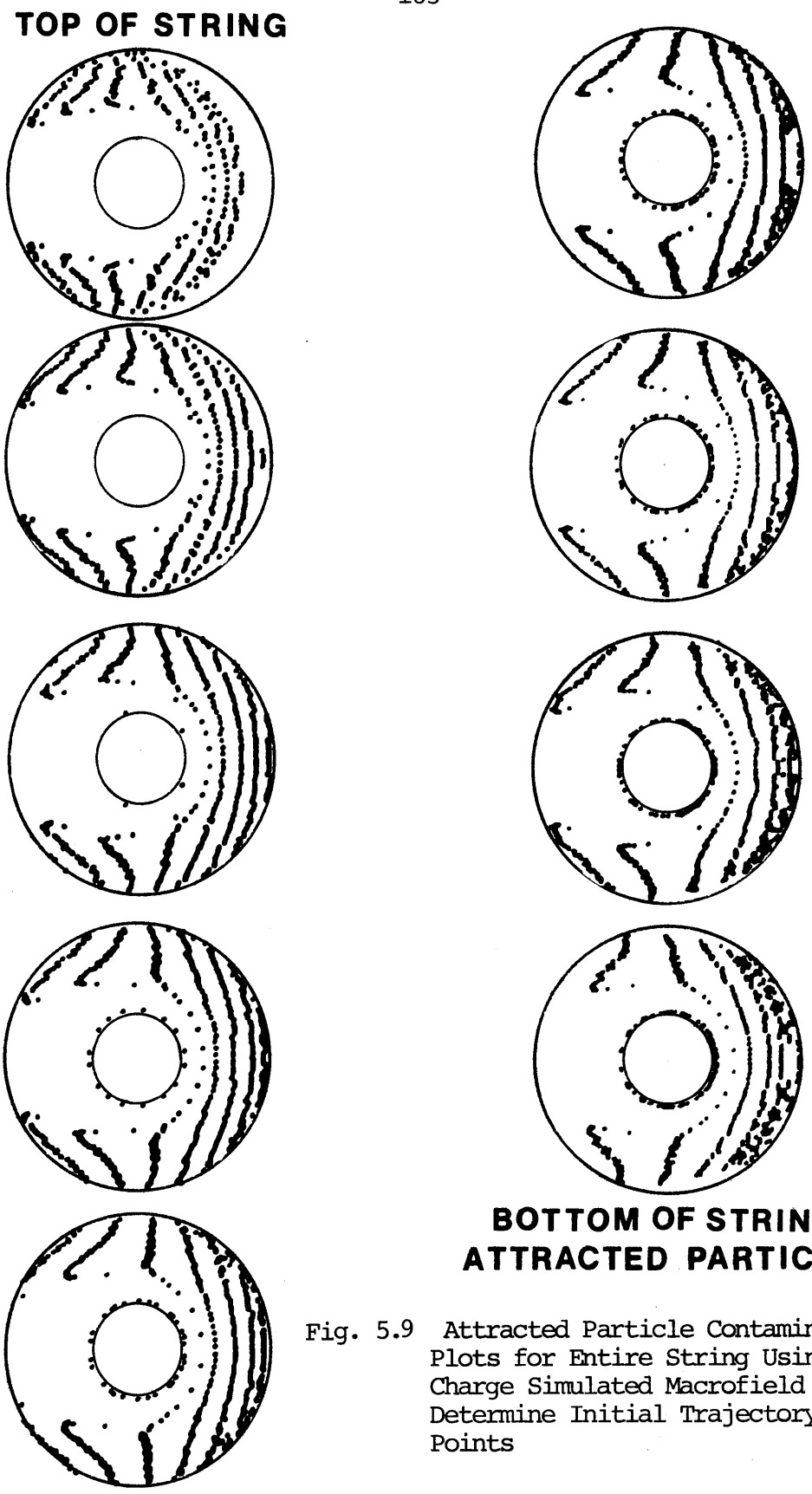

Fig. 5.9 Attracted Particle Contamination Plots for Entire String Using Ring Charge Simulated Macrofield to Determine Initial Trajectory Points

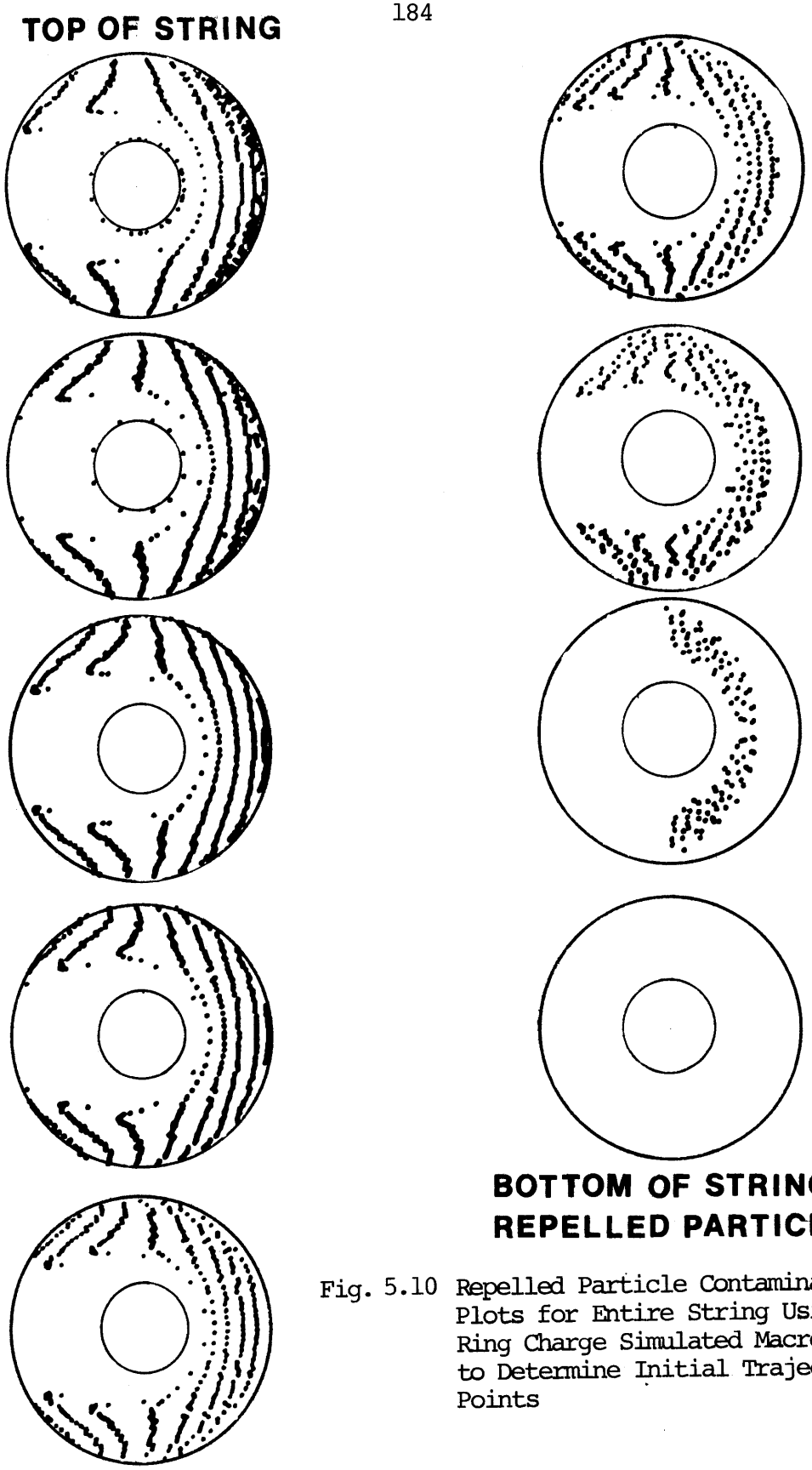

Fig. 5.10 Repelled Particle Contamination Plots for Entire String Using Ring Charge Simulated Macrofield to Determine Initial Trajectory Points

contamination on each insulator plot.

It should be emphasized once again that the density of dots on the plots does not signify a surface mass density--the dots are only useful for identifying the portions of the insulator surface, as delineated by demarcation lines, where contamination occurs at the rate $\bar{\Gamma} = -\bar{n}\cdot Nb\bar{E}$.

Figure 5.11 shows the results of such a computation, in comparison with the measured distributions of Fig. 5.3 (which are replotted here as part of Fig. 5.11). Agreement is reasonable, considering the relative simplicity of the model used to compute the trajectories. A more accurate computation of the field distribution, possibly including an extension of the edge fields into the microregion, would likely lead to even better agreement between theoretical prediction and measured contaminant distributions.

The simple segregation model, developed specifically in this section to explain the test chamber experiments, is of significant academic interest, but must be applied to an actual insulator string with caution. In the analysis, the insulators are appropriately modeled as thin, flat disks. The perturbations to trajectories entering the various microregions, caused by the macroscopic fringing fields at the disk edges, are calculated. In essence, the macroregion and microregions are clearly separated by the macro-micro boundary. A real insulator, however, is not a thin flat disk, but rather may offer a substantial part of its surface area for

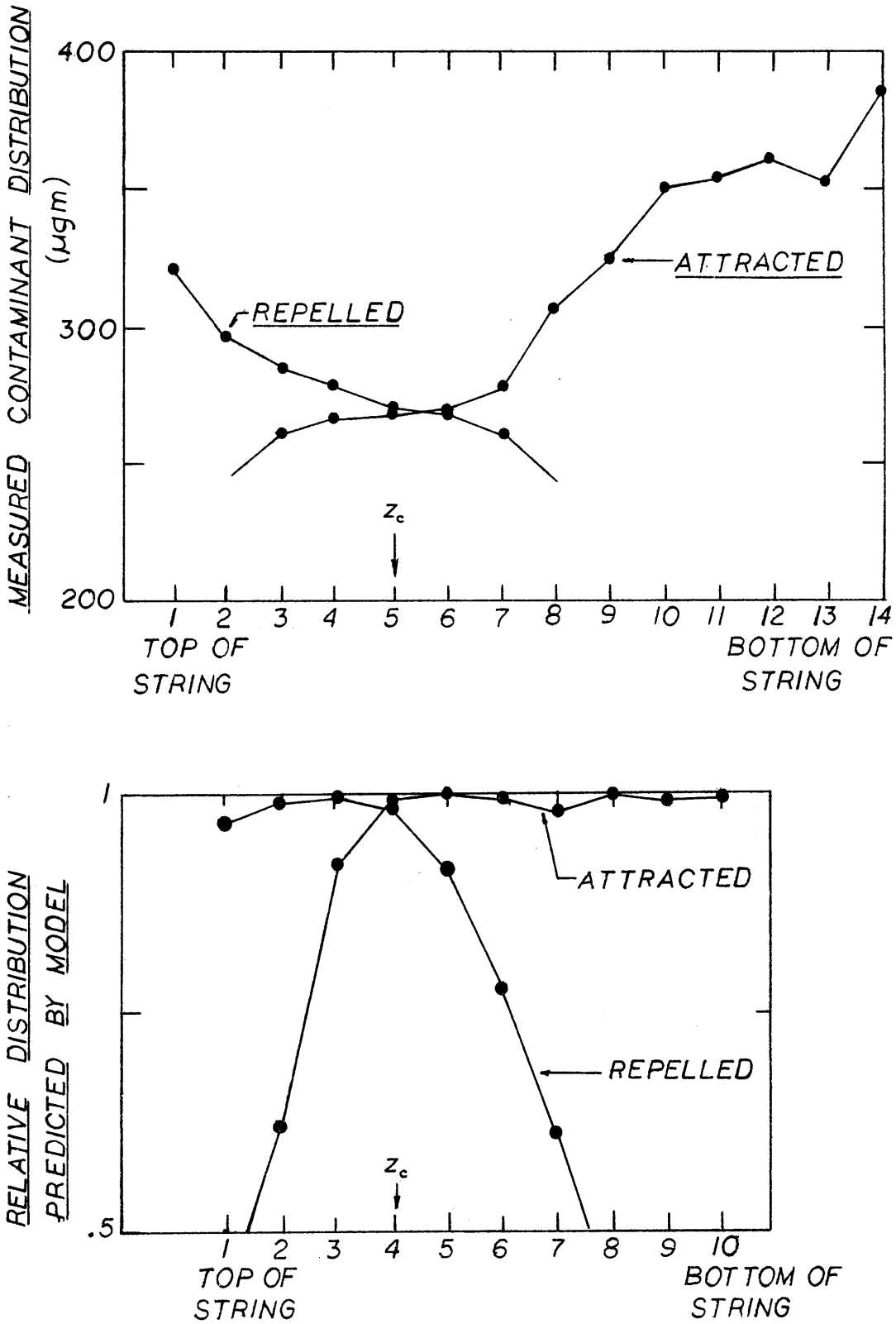

Fig. 5.11 Measured Contaminant Distributions (top figure) and Predicted Relative Contaminant Distributions (bottom figure) for Attracted and Repelled Particles

the termination of the radial fringing fields. A distinct boundary between the macro and microregions, at which the fringing field perturbations may be analyzed, may not exist. If one were to define a "range of applicability" for the segregation model of this section, at one extreme would be an insulator string composed of thin, flat, and closely spaced disks, in which the macro and microregions are clearly delineated, and the location of the perturbing fringing fields clearly defined. At the other extreme would be a rigid solid cylinder, for which no microregion exists at all, and for which the components of the macrofield radial to the insulator string axis may no longer be considered fringing fields, but rather terminate everywhere on the cylinder surface.

In the former case of thin, closely spaced insulator units, the segregation model is certainly applicable, but at the same time predicts that the segregation effect be gradually diminished at higher and higher ambient wind velocities. In the latter case of the solid cylinder, the existence of contamination on any given region of surface area will solely be determined by the sign of the component of electric field normal to the surface--hence we expect the segregation effect, carried to the limit of a solid cylinder, to be observed at any wind speed. In actuality, a real insulator string must fall somewhere between the two extremes described--exactly where will of course depend on the exact insulator design.

How important will the segregation issue be in the prediction of contamination of a real insulator string? Typically, predictions of contamination will be implemented so as to insure that contaminant levels on a given string will not exceed some maximum safety margin level. Most disk suspension insulator strings will not approach the limit of a rigid solid cylinder, and some degree of velocity dependent segregation can be expected. However, the multiplicity of fluctuating wind velocities and particle mobilities likely to be found around an actual line will tend to smear out the contaminant distributions observed for any one wind velocity and particle mobility. Hence, to what is a first order engineering approximation, it is practical to neglect segregation when predicting contaminant levels on a real line for the purpose of insuring that safety margin levels are not exceeded.

CHAPTER 6

CONTAMINATION ABOVE CORONA THRESHOLD

6.1 Introduction

The analysis of contamination presented thusfar has assumed the line conductor of the transmission line, and all associated hardware fittings, to be corona free. In reality, any practical transmission line may be expected to emit some corona. On test sections of BPA line, similar to the Pacific Intertie line, for example, average corona current levels as high as about 15 μa/meter have been reported under certain weather conditions.[2] An exact analysis of corona phenomena is exceedingly difficult, particularly when the corona current is not a distributed variable, but instead is emitted from isolated points on the line conductor and hardware fittings. A detailed study of corona on high voltage dc transmission lines could be the subject of a major investigation itself. In the context of the present discussion, we are only interested in the effects of corona on the contamination process. Therefore the purpose of the present chapter is to simply set down issues and physical principles which can be applied to more detailed studies of contamination phenomena above corona threshold.

6.2 Physical Laws and Scaling Above Corona Threshold

When corona current is emitted from the line conductor

of a high voltage transmission line, the simple electric field scaling law, Eq. (2.4):

$$\frac{V_m}{\ell_m} = \frac{V_a}{\ell_a}$$

no longer applies exactly. The presence of corona space charge will in general modify the macroscopic electric field distribution around the line conductor and insulator string, and the effect of the discharge and associated space charge on the field must be considered. Because the macroscopic field has a minor effect on the particle trajectories, however, primary interest in the above corona regime focuses on how the charge of incident particles is altered by the space charge. This latter consideration will be covered in the next section; the purpose of the current discussion is to examine the nature of the electric field when it is modified by corona space charge.

Most of the observed corona loss on real lines can be associated with isolated point discharges from conductor irregularities and hardware fittings. The bulk of the line conductor is below the threshold of glow corona. For the purpose of examining the effects of corona in the test chamber, some modification of this situation is in order. In particular, any corona that is experimentally established must be manageable and lend itself to analytical quantification. Corona from irregular points tends to be rather

unpredictable and nonuniform, hence when corona is desired in the test chamber a single smooth line conductor is operated in the much more stable glow discharge mode, just above the threshold of corona. This mode of corona has a calculable space charge in coaxial geometry, which can be used as an estimate of the space charge actually existing in the chamber for a given level of corona current.

One consequence of operating the line conductor above corona onset is that the electric field strength at the surface of the model conductor in corona remains relatively constant and independent of voltage on the line, and is given by Peek's law for coaxial geometry:[10,23]

$$E_c \equiv E_p = 3.1 \times 10^6 \left(1 + \frac{.0308}{\sqrt{a}}\right) \text{ V/m} \qquad (6.1)$$

where a = conductor radius, and E_c is the field strength at the inner conductor.

In corona work, only two geometries lend themselves easily to mathematical formulation: line-to-plane geometry, and coaxial geometry.[10] The theoretical i-v relation for coaxial systems which has historically agreed well with experiment is, for glow corona modes:[7,10]

$$V = \frac{1}{\xi} \left(R_o^2 + c^2\right)^{1/2} - \left(a^2 + c^2\right)^{1/2} - c \ln \left[\frac{a\left(c+\sqrt{R_o^2+c^2}\right)}{R_o\left(c+\sqrt{a^2+c^2}\right)}\right] \qquad (6.2)$$

where a = conductor radius

R_o = radius of outer coaxial shell

V = voltage between conductor and shell

b_{ion} = ion mobility $\sim 1.4 \times 10^{-4}$ m^2/v-sec in air

$$\frac{1}{\xi} = \left[\frac{i_c}{2\pi\varepsilon_o |b_{ion}|}\right]^{1/2} \qquad (i_c \text{ in amps/meter})$$

$$c = [a^2 (E_p{}^2 \xi^2 - 1)]^{1/2}$$

and $E_p \xi >> 1$, i.e. low levels of corona current.

The analysis of the glow corona mode, which leads to the above i-v relation, presumes all ionization activity in the gas to be confined to a thin sheath around the highly stressed inner conductor. The field solution within the coaxial electrode space is derived using the inner conductor as a boundary surface source of space charge ions.

In an effort to justify analyzing the test chamber corona in coaxial geometry, comparisons were made between experimental i-v corona data taken with a single, smooth conductor (without the insulator string attached), and the theoretical i-v curve predicted by Eq. (6.2). Figure 6.1 shows a plot of Eq. (6.2) superimposed on i-v data taken in the test chamber with a conductor radius of .238 cm. Reasonable correlation between the actual system and the theoretical coaxial system can be gotten by choosing R_o = 1 meter as the outer coaxial shell radius.

The space charge in the test chamber may thus also be approximated, for any level of i_c, by the equation derivable

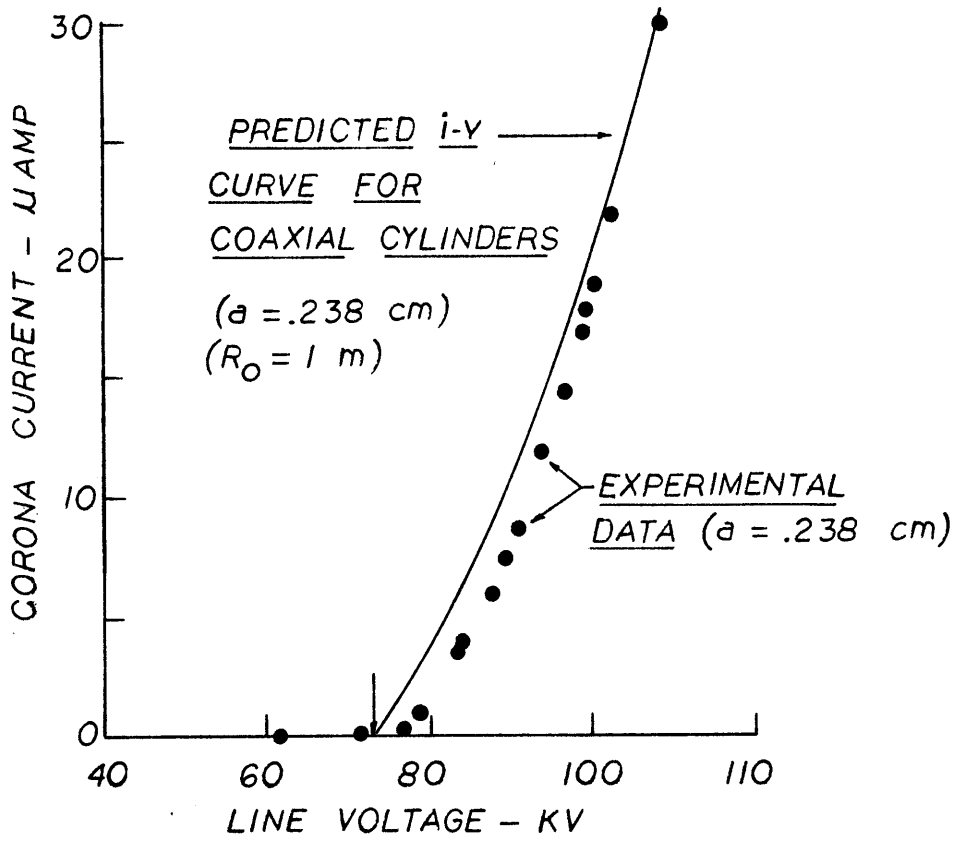

Fig. 6.1 Theoretical Corona i-v Curve Superimposed on Experimental Data

for the coaxial case:[10]

$$\rho_c(r) = \frac{i_c}{2\pi r |b_{ion}| E} \tag{6.3}$$

where here ρ_c = space charge density, and the electric field E(r), understood to have only a radial component, is given by:

$$E(r) = \left[\frac{1}{\xi^2} \left(1 - \frac{a^2}{r^2}\right) + \frac{a^2 E_c^2}{r^2} \right]^{1/2} \tag{6.4}$$

where E_c is again the field strength at the inner conductor.

The electric field expression (6.4) is exact for coaxial geometry, except for the thin sheath around the conductor where the gaseous ionization takes place. We may thus assess the deviation of (6.4) from the imposed field equation applicable to the sub-corona regime:

$$E(r) = \frac{V/r}{\ell n\ (R_o/a)} \tag{6.5}$$

The exact expression (6.4) equals the corona-free field (6.5) for line voltages below corona onset voltage V_c, since i_c is zero for voltages below V_c.

At the voltage V_c, the field at the conductor:

$$E_c = E(r)\Big|_{\substack{V=V_c \\ r=a}} = \frac{V_c/a}{\ell n\ (R_o/a)} \tag{6.6}$$

just equals Peek's field E_p . For conductor voltages higher than V_c, the conductor field remains at E_p, and corona current begins to flow, thus altering the gap field as per Eq. (6.4). At the outer extremities of the test chamber, corresponding to $r = R_o = 1$ meter in the field expression (6.4), very little corona current i_c is required to substantially alter the gap field. For example, just at onset, $i_c = 0$, and

$$E(R_o)\Big|_{\text{onset}} = \frac{aE_p}{R_o}$$

A space charge modified field of twice this magnitude will result if the corona current is further increased to the point where

$$E(R_o) = \frac{2a\,E_p}{R_o} = \left[\frac{1}{\xi^2}\left(1 - \frac{a^2}{R_o^2}\right) + \frac{a^2\,E_p^2}{R_o^2}\right]^{1/2}$$

or
$$\frac{1}{\xi^2} = \frac{i_c}{2\pi\varepsilon_o|b_{ion}|} = \frac{a^2\,E_p^2}{R_o^2}\left(\frac{R_o^2}{R_o^2 - a^2}\right)$$

$$\therefore \quad i_c = \frac{a^2\,E_p^2}{(R_o^2 - a^2)}\,2\pi\varepsilon_o|b_{ion}| \;\tilde{=}\; 1.1 \;\; \mu\text{amp/meter},$$

a rather modest corona current.

Closer to the insulator string, say at $r = .1$ meter, the current required to double the space charge free field is much greater:

$$i_c \;\tilde{=}\; 110 \;\; \mu\text{amp/meter}$$

In general, then, we may expect sizeable modifications to the existing macroscopic fields by space charge ions at the extremities of the test chamber, and lesser modifications closer to the insulator string.

By the same token, it may also be shown experimentally, by photographs of the corona discharge around the model line conductor, that the insulator string itself shields the short section of conductor just beneath its base, which consequently does not emit corona when the rest of the line does. The insulator string will thus be somewhat shielded from the space charge ions. Certainly, little if any space charge will find its way into the various microregions. Since we are interested primarily in duplication of the microscopic and fringing electric fields around the insulator string and section of conductor just beneath the string, the best field scaling, even in the above corona regime, will thus be achieved when:

$$\frac{V_m}{\ell_m} = \frac{V_a}{\ell_a} \tag{6.7}$$

For situations where the field far from the conductor in corona is important, the modifications to the field caused by the space charge and Peek's law can be taken into account. For the purposes of recreating the coulomb attraction felt by contaminant particles in the microregion, however, the unperturbed fields should be sufficient. Note that space

charge is not being overlooked here as a means by which contaminant particles may be charged. What is being neglected is simply the scaling of the effect of the space charge on the field far away from the insulator string.

The magnitude of space charge itself is in fact of prime importance in scaling the temporal development of the particle charging process that takes place in the corona flux. If the contaminant particles are modeled as conducting spheres, the primary mechanism for particle charging can be described once again by the charging model developed in Appendix A. The accumulation of charge on a particle in a uniform electric field and positive ion flux, where the drift velocity of the ions is everywhere very much greater than the ambient wind velocity, can be approximated by the equations (A.10) through (A.12):

$$q = \text{constant} \qquad q > q_{sat} \qquad \text{(A.10)}$$

$$q = 3\pi R_p^{\,2} E\, \rho_c |b_{ion}| \left[\frac{t}{\frac{\rho_c |b_{ion}|}{4\varepsilon_o} t + 1} \right] \qquad -q_{sat} \leq q \leq q_{sat} \qquad \text{(A.11)}$$

$$q = q_o \exp - \left[\frac{\rho_c |b_{ion}|}{\varepsilon_o} \right] t \qquad q < -q_{sat} \qquad \text{(A.12)}$$

where q is the accumulated particle charge, and q_{sat} is the saturation charge at "$t = \infty$", equal to $12\pi\varepsilon_o R_p^{\,2} E$. Similar equations can be derived for a negative corona flux by

appropriate changes of sign. The charging equation (A.11) is characterized by the hyperbolic time constant $4\varepsilon_o/\rho_c|b_{ion}|$, and (A.12) by the exponential time constant $\varepsilon_o/\rho_c|b_{ion}|$.

Since the wind dominates the macroscopic particle motion, and hence the speed and transport time of the particles, the ratio of charging time constant to wind transport time should, for the purposes of scaling, be kept the same in the real and model systems. So doing assures us that the dynamics of the charging process, i.e. how long a particle spends in a certain region of field strength and ion flux, for example, and what fraction of q_{sat} it accumulates, will be preserved. This time constant constraint determines the ratio of corona space charge densities in the actual and model systems:

$$\text{i.e.} \quad \frac{\text{charging time}}{\text{wind transport time}} = \frac{\varepsilon_o/\rho_c|b_{ion}|}{\ell/U} = \text{constant} \qquad (6.8)$$

implies

$$\frac{\varepsilon_o/\rho_{c\ m}|b_{ion}|}{\ell_m/U_m} = \frac{\varepsilon_o/\rho_{c\ a}|b_{ion}|}{\ell_a/U_a} \qquad (6.9)$$

In light of the previously determined ratio (2.3) for U_m/U_a:

$$\frac{U_m}{U_a} = \frac{\ell_a}{\ell_m} \qquad (6.10)$$

the expression (6.9) simplifies to:

$$\frac{\rho_{c\,m}}{\rho_{c\,a}} = \frac{U_m}{U_a} \qquad \frac{\ell_a}{\ell_m} = \left[\frac{\ell_a}{\ell_m}\right]^2 \tag{6.11}$$

Note here that the actual transmission line is not in coaxial geometry, so one cannot hope to model accurately everywhere the magnitude of corona space charge as specified by Eq. (6.11). Nevertheless, the relation (6.11) tells us, for a given scaling ratio ℓ_m/ℓ_a, how big to make the charge density in the test chamber, in order to model a given level of charge at a specific point of interest in the actual system, where an order of magnitude approximation to ρ_c is appropriate.

In practice, altering i_c, and hence ρ_c in the test chamber is accomplished by adjusting the line voltage above onset, and/or the line conductor diameter.

In the sub-corona regime, it was possible to scale the particle mechanics by way of a general mobility constraint, Eq. (2.10):

$$\frac{b_m}{b_a} \equiv \frac{\dfrac{q_m}{6\pi\eta\, R_{pm}}}{\dfrac{q_a}{6\pi\eta\, R_{pa}}} = \frac{\ell_a}{\ell_m} \tag{6.12}$$

in which only the ratio $\frac{q}{R_p}$ was of importance, and the exact values of q and R_p arbitrary. In the present case, where we have modeled the time dependence of the particle charging dynamics, to which q and R_p are intimately related, the ratio $\frac{q}{R_p}$

should still be scaled to preserve the particle mechanics, but the exact values of q and R_p will no longer be arbitrary.

The particle charge q will at any given moment be some fraction of the local value of q_{sat}*, which in turn depends on both R_p and the local value of E.

If the time dependence of the charging process is accurately scaled, via Eq. (6.8), then the fraction of q_{sat}, g(t) to which a particle is charged will be equal in the model and actual systems. Maintaining the scaling of particle mechanics via the mobility constraint (6.12) therefore requires:

$$\left.\frac{b_m}{b_a}\right|_{\substack{\text{at any}\\ \text{instant}}} \equiv \frac{\left[\dfrac{g(t)\ q_{sat\ m}}{6\pi\eta\ R_{pm}}\right]}{\left[\dfrac{g(t)\ q_{sat\ a}}{6\pi\eta\ R_{pa}}\right]} = \frac{\ell_a}{\ell_m} \qquad (6.13)$$

or

$$\frac{(12\pi\varepsilon_o\ R_{pm}^{\ 2}\ E_m)(6\pi\eta\ R_{pa})}{(12\pi\varepsilon_o\ R_{pa}^{\ 2}\ E_a)(6\pi\eta\ R_{pm})} = \frac{\ell_a}{\ell_m}$$

$$\therefore \quad \frac{R_{pm}}{R_{pa}} = \frac{E_a}{E_m}\ \frac{\ell_a}{\ell_m} \qquad (6.14)$$

In the close proximity of the conductor and insulator string, where the effect of corona space charge on the field

---

*Except, of course for particles charged to $q > q_{sat}$, which follow the charging law (A.10), and for which charging dynamics do not apply. The charge of such particles will remain fixed, and the general mobility constraint (6.12) adequate for scaling their particle mechanics.

is negligible, $E_m \approx E_a$, so:

$$\frac{R_{pm}}{R_{pa}} = \frac{\ell_a}{\ell_m} \tag{6.15}$$

At the chamber extremities, the exact ratio of the space charged perturbed fields E_a/E_m should be computed, but this ratio will not be constant as a function of position. Since a charging particle will acquire most of its charge, and hence its final value of mobility before participating in the precipitation process, near the conductor and string, the expression (6.15) is the more accurate.

The particle size scaling (6.15) restricts somewhat the size of particles that can be modeled in the test chamber, because the test particles, now larger than the actual particles by a factor $\frac{\ell_a}{\ell_m}$, must still be smaller than about 10 microns, so that the inertialess approximation to the particle motion, as outlined in Chapter 2, will still be valid.

6.3 Particle Trajectories in the Presence of Corona

The particle trajectory equation of Chapter 4:

$$\frac{d\bar{x}}{dt} = \bar{v} + b\bar{E} \tag{6.16}$$

holds true even when the field $\bar{E}$ is modified by the presence of corona space charge. However, the statement:

$$\frac{dN}{dt} = 0 \tag{6.17}$$

if it is to hold true along any trajectory line, requires that

$$\nabla \cdot b\bar{E} = 0 \tag{6.18}$$

which will not be globally satisfied when corona is present. According to the calculations of the previous section, for example, the component of $\nabla \cdot b\bar{E}$ associated with the space charge density ρ_c may be substantial. In general, the derivation of Chapter 4 which led to (6.17) must be reexamined. Equation (4.4) becomes:

$$\left[\frac{\partial N}{\partial t} + (\bar{v} + b\bar{E}) \cdot \nabla N\right] + N\bar{E} \cdot \nabla b + Nb\, \nabla \cdot \bar{E} = 0$$

$$\frac{dN}{dt} = -N\left[\bar{E} \cdot \nabla b + \frac{b\, \rho_c}{\varepsilon_o}\right] \tag{6.19}$$

where the field due to the charge on the particles has been ignored, and Gauss' law has been invoked in deriving the last term on the right. The above expression yields:

$$\frac{dN}{N} = -\left[\bar{E} \cdot \nabla b + \frac{b\, \rho_c}{\varepsilon_o}\right] dt \tag{6.20}$$

which describes the change in particle number density N along any trajectory line given by Eq. (6.16). The changing particle density may be attributed to two causes. The second term on the right in (6.20) describes the divergent nature of the space charge modified field, which may bunch or rarify a

given incremental volume of particles. The first term on the right accounts for the change in the accumulated charge on a particle as it travels along a trajectory line. The change in particle charge, as manifest in a value of particle mobility that changes with position, may cause a net divergence of particles into or out of a given incremental volume.

The particle density equation (6.20) is complex, but must be solved for any specific line geometry and insulator configuration if exact and accurate estimates are desired for the value of N at the termini of trajectories ending on the insulator surfaces. On the other hand, a good engineering approximation to the change in N can be gotten by both estimating the relative magnitude of the $\bar{E}\cdot\nabla b$ term, and by assuming ρ_c to be relatively constant over a region of space surrounding the line conductor. This latter assumption is not, in fact, unreasonable for the coaxial-like geometry of the test chamber.

In the next section it will be shown that an initially neutral particle incident upon a corona flux may acquire enough charge to attain mobilities comparable to the highest naturally occurring mobilities. For estimation purposes, then, we may expect values of b to be on the order of $\frac{b}{\ell}$, where ℓ is a scale length typifying a trajectory path. Similarly, $\bar{E}$ may be chosen as some average $\langle E \rangle$ encountered by the particle over most of its journey, and the average value of mobility may be taken as $\frac{b}{2}$.

Hence, if ρ_c is assumed to be approximately constant, Eq. (6.20) may be integrated to yield:

$$\ell n \frac{N}{N_o} \cong -\left[\frac{\langle E\rangle b}{\ell} + \frac{b \rho_c}{2\varepsilon_o}\right] t$$

$$N \cong N_o \exp -\left[\frac{\langle E\rangle b}{\ell} + \frac{b \rho_c}{2\varepsilon_o}\right] t \quad (6.21)$$

A valid time scale of interest is the wind transport time ℓ/U, applicable whenever the wind dominates the macroscopic particle motion, hence:

$$N \cong N_o \exp -\left[\frac{\langle E\rangle b}{\ell} + \frac{b \rho_c}{2\varepsilon_o}\right] \frac{\ell}{U} \quad (6.22)$$

For the purpose of an engineering estimation of contamination, one concludes that $N \cong$ constant along any trajectory line, provided that

$$\frac{b}{U}\left[\langle E\rangle + \frac{\rho_c \ell}{2\varepsilon_o}\right] << 1 \quad (6.23)$$

Since $\rho_c \ell/\varepsilon_o$ typifies the space charge correction to the imposed field, we note that the inequality (6.23) will be met if the wind velocity dominates both the electric drift velocity due to the imposed field, and the drift velocity attributable to the space charge modified portion of the electric field.

Even when the space charge field correction is much

smaller than the externally imposed field, the wind must dominate the particle motion if the approximation $N \approx$ constant is to hold true. Otherwise, the rarefaction of particles due to changing mobilities may be substantial, depending on the degree of particle charging taking place.

In the test chamber, the wind does dominate the macroscopic motion, where typical magnitudes of ρ_c, $\langle E \rangle$, b, and U are:

$$\langle E \rangle \sim 1 \times 10^5 \text{ v/m}$$
$$b = 5 \times 10^{-7} \text{ m}^2/\text{v-sec}$$
$$U = .25 \text{ m/sec}$$
$$\rho_c = 1 \times 10^{-6} \text{ coul/m}^3 \text{ maximum}$$
(based on 10 μamp/m of corona current)

Hence we find, for ℓ = 1 meter:

$$\frac{N}{N_o} \cong \exp - \left[\frac{(5 \times 10^{-7})}{(.25)}\right] \left[(1 \times 10^5) + \frac{(1 \times 10^{-6})(1)}{(2)(8.85 \times 10^{-12})}\right] \approx .73 \qquad (6.24)$$

Although a change in N may thus be expected in any exact solution of the particle density equation (6.20) in the test chamber, the result (6.24) indicates that to a first approximation the assumption $N \approx$ constant should still be made in this case, as N will not vary by orders of magnitude as the particles pass from injection point to insulator surface.

6.4 Dynamics of Particle Charging in a Corona Flux

The particle charging equations developed in Appendix A presume the particle to lie in a uniform electric field, with ion trajectories originating in a homogeneous, uniform source of ion space charge density ρ_c. In actuality, neither the field nor space charge are constant, but are rather functions of position, as specified, for example, by Eqs. (6.3) and (6.4). Nevertheless, the fate of contaminant particles encountering a line in corona may still be examined using the charging equations (A.10) through (A.12), because these expressions will be valid if $\bar{E}$ and ρ_c are relatively uniform over a distance of several particle diameters--about the distance required for the field solution embodied in (A.3) to revert to the ambient field strength. The necessary requirement implicit also in the derivation of the particle charging equations:

$$\nabla \cdot \bar{E} = 0 \tag{6.25}$$

will again not be globally satisfied when corona is present, but as long as (6.25) is approximately met over the span of several particle diameters in the vicinity of the particle, the trajectory principles used to derive the particle charging equations will be valid, and applicable to the flow of ion space charge around a contaminant particle. For example, the field expression (6.4) may be expanded about the location of a given particle at r:

$$E(r + \Delta r) \approx E(r) + \frac{\Delta r}{r}\left[\frac{\frac{a^2}{\xi^2 r^2} - \frac{a^2 E_c^2}{r^2}}{E(r)}\right] + \left(\frac{\Delta r}{r}\right)^2 \quad \ldots(6.26)$$

The magnitude of the numerator of the second term in brackets will always be less than $[E(r)]^2$, so that for Δr equal to several R_p, $\frac{\Delta r}{r} << 1$, and the correction terms above will be negligible, i.e.

$$E(r) \approx \text{constant} \qquad (6.27)$$

in the vicinity of the particle. Similarly,

$$\nabla\cdot\bar{E} = \frac{1}{r}\,\frac{1}{\xi^2 E(r)} \qquad (6.28)$$

so that on the scale of interest $\frac{\Delta r}{r} << 1$, and for practical levels of corona current such that $\frac{1}{\xi} << E_c$,

$$\frac{(\nabla\cdot\bar{E})\Delta r}{E(r)} = \frac{\Delta r}{r}\,\frac{1}{\xi^2 E(r)^2} << 1 \qquad (6.29)$$

We may thus, according to (6.27) and (6.29), apply the particle charging equations locally at a given particle location. The macroscopic field E(r) and space charge density ρ_c may vary greatly over the confines of the test chamber, hence both q_{sat}, and the time constants $\frac{4\varepsilon_o}{\rho_c|b_{ion}|}$ and $\frac{\varepsilon_o}{\rho_c|b_{ion}|}$ will be functions of position, and the charge

accumulated by an initially neutral particle will depend greatly on how much time the particle spends in various locations around the line and insulator string.

The interdependence of particle charge and position assures that the model system be a dynamic one. Calculations show that for typical corona fluxes and wind velocities, one cannot always assume simplifications like a "constant particle charge" over the time it takes the wind to transport the particle, or "immediate charging" to the local value of q_{sat}. One must instead solve the complete set of differential equations for a given set of system conditions.

The equations developed in Chapter 4 governing the macroscopic particle trajectory motion may be coupled with the particle charging equations to yield a composite set of dynamic particle charging equations. For simplicity, the equations are presented below for particles incident on a simple coaxial conductor in the stationary flow case--very analogous to the first macroscopic trajectory analysis of Section 4.5, but with the particle charge determined in this case by the particle charging equations. The analysis to follow is quite elementary, but the principles embodied in it could be applied to more complicated cases incorporating, for example, the presence of the insulator string. In the coordinate system of Chapter 4, summarized by Fig. 4.13, and with the understanding that $\bar{E}$ has a radial component only, the equations become:

$$\frac{dr}{dt} = \frac{q}{6\pi\eta R_p} E - U_o\left(1 - \frac{a^2}{r^2}\right) \cos\theta \qquad (6.30)$$

$$\frac{d\theta}{dt} = U_o\left(1 + \frac{a^2}{r^2}\right) \frac{\sin\theta}{r} \qquad (6.31)$$

$$\frac{dq}{dt}\begin{cases} = 0 & q > q_{sat} \\ = 3\pi R_p^2 \rho_c |b_{ion}| E \left(1 - \frac{q}{q_{sat}}\right)^2 & |q| \leq q_{sat} \\ = -\frac{\rho_c |b_{ion}| q}{\varepsilon_o} & q < -q_{sat} \end{cases} \qquad (6.32)$$

where, as before:

$$q_{sat} = 12\pi\varepsilon_o R_p^2 E \qquad (6.33)$$

$$\rho_c = \frac{i_c}{2\pi r |b_{ion}| E} \qquad (6.34)$$

$$E = \left[\frac{i_c}{2\pi\varepsilon_o |b_{ion}|}\left(1 - \frac{a^2}{r^2}\right) + \frac{a^2 E_c^2}{r^2}\right]^{1/2} \qquad (6.35)$$

The objective here is to numerically integrate the above equations to estimate the change in mobility of particles, as reflected in the amount of charge they accumulate when they encounter the line conductor. The conclusion of Chapter 4, namely that the macroscopic trajectories are dominated by the wind motion, will prevail for most particles

experiencing charging. As suggested by the discussion of Section 5.3, only for the rare cases of very high initial particle mobility will the coulomb force have any major effect on the macrotrajectories. Such highly naturally charged particles, if carried to the transmission line site by some means, would typically be charged well above the maximum values of q_{sat} existing anywhere around the conductor.

Integrating the system equations (6.30) through (6.35) is best accomplished using a Runge-Kutta technique, rather than Newton's method. The particle charging process is exponential for $q < -q_{sat}$, and even when $|q| \leq q_{sat}$, the hyperbolic charging function may be rapid. The equations (6.30) through (6.35) were thus numerically integrated according to the flowchart of Fig. 6.2, for a variety of test parameters. The levels of corona space charge simulated were chosen to model in magnitude the average corona levels on the Pacific Intertie line, although, as discussed previously, the actual line does not operate in the glow mode.

The results, summarized in Figs. 6.3 through 6.6, depict particles injected into the airstream at the outer bounds of the test chamber at r = 1 meter, and at a height corresponding to the midsection of the insulator string location. The plots trace the horizontal distance of the particle from the plane of the line conductor. As expected, no vertical deflection of particles occurs in any of the simulations. Once again, the plots reflect a positive line conductor, but

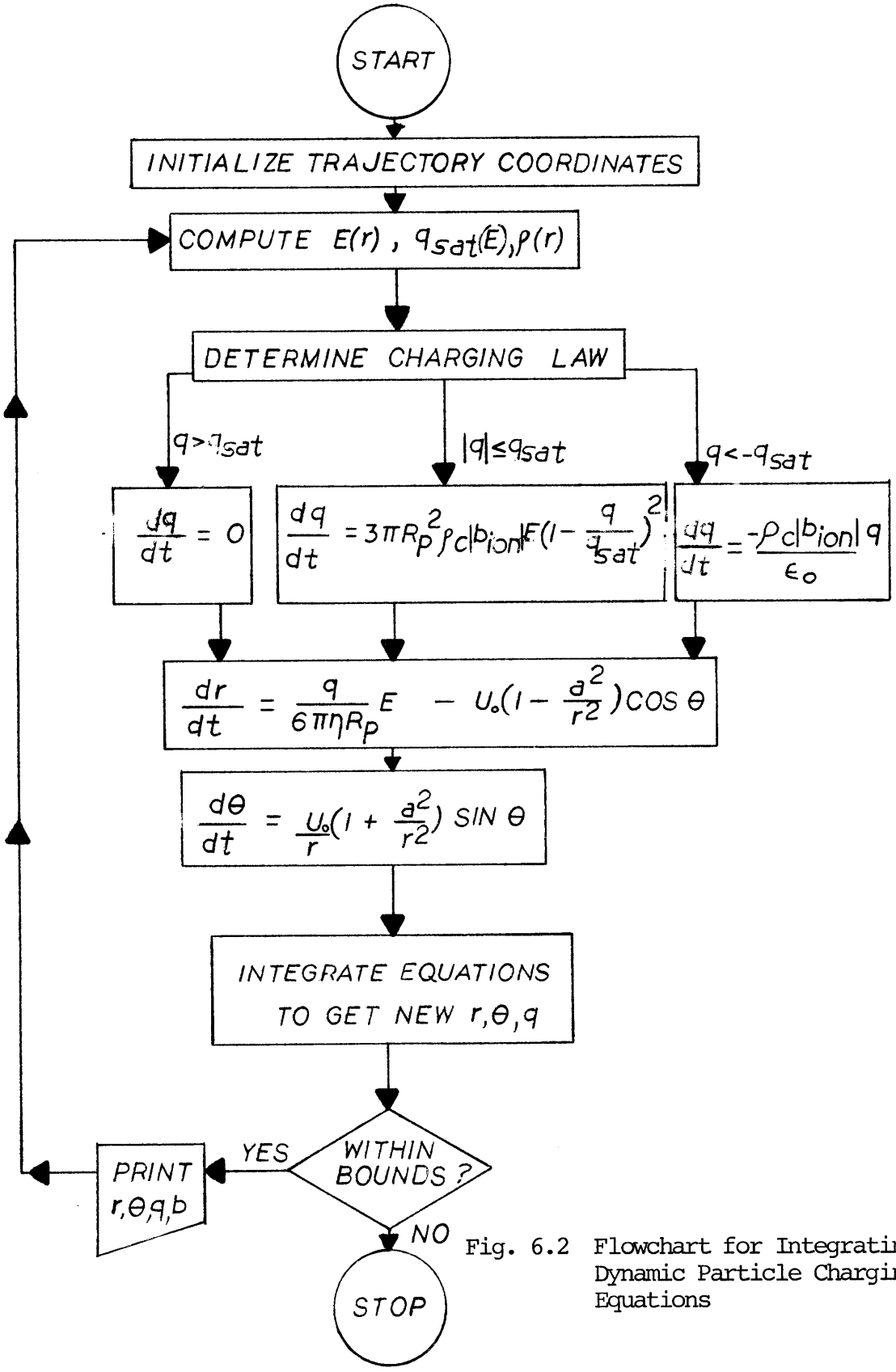

Fig. 6.2 Flowchart for Integrating Dynamic Particle Charging Equations

the results apply equally well for a negative line conductor if appropriate sign changes are made.

The first plot, Fig. 6.3, underscores the dynamic nature of the particle charging process. Shown in the plot are the accumulated charges and equivalent mobilities of initially neutral 4 micron particles entering at various wind speeds, and incident upon a conductor emitting 10 μamp/meter of corona current. Note that all the final charge values are substantial, but for no wind speed considered does the particle reach the saturation charge. As expected, the final values of accumulated charge decrease with increasing wind velocity, since the particle spends a smaller amount of time in the charging flux as it passes toward the insulator string. Figure 6.4 shows the accumulated charges of 4 micron particles entering at .2 m/sec, for a variety of corona current levels. Again, as expected, the higher currents yield more highly charged particles--an effect attributable to faster particle charging time constants at the higher current levels.

Of particular interest are the two plots of Figs. 6.5 and 6.6, for which i_c = 10 μamp and 1 μamp, respectively, and U = .2 m/sec. Shown in comparison in each plot are an initially neutral particle, and a particle with a substantial initial negative charge. In the case of Fig. 6.5 (i_c = 10 μamp) the initially negative particle discharges almost instantly, and thereafter behaves as a neutral particle.

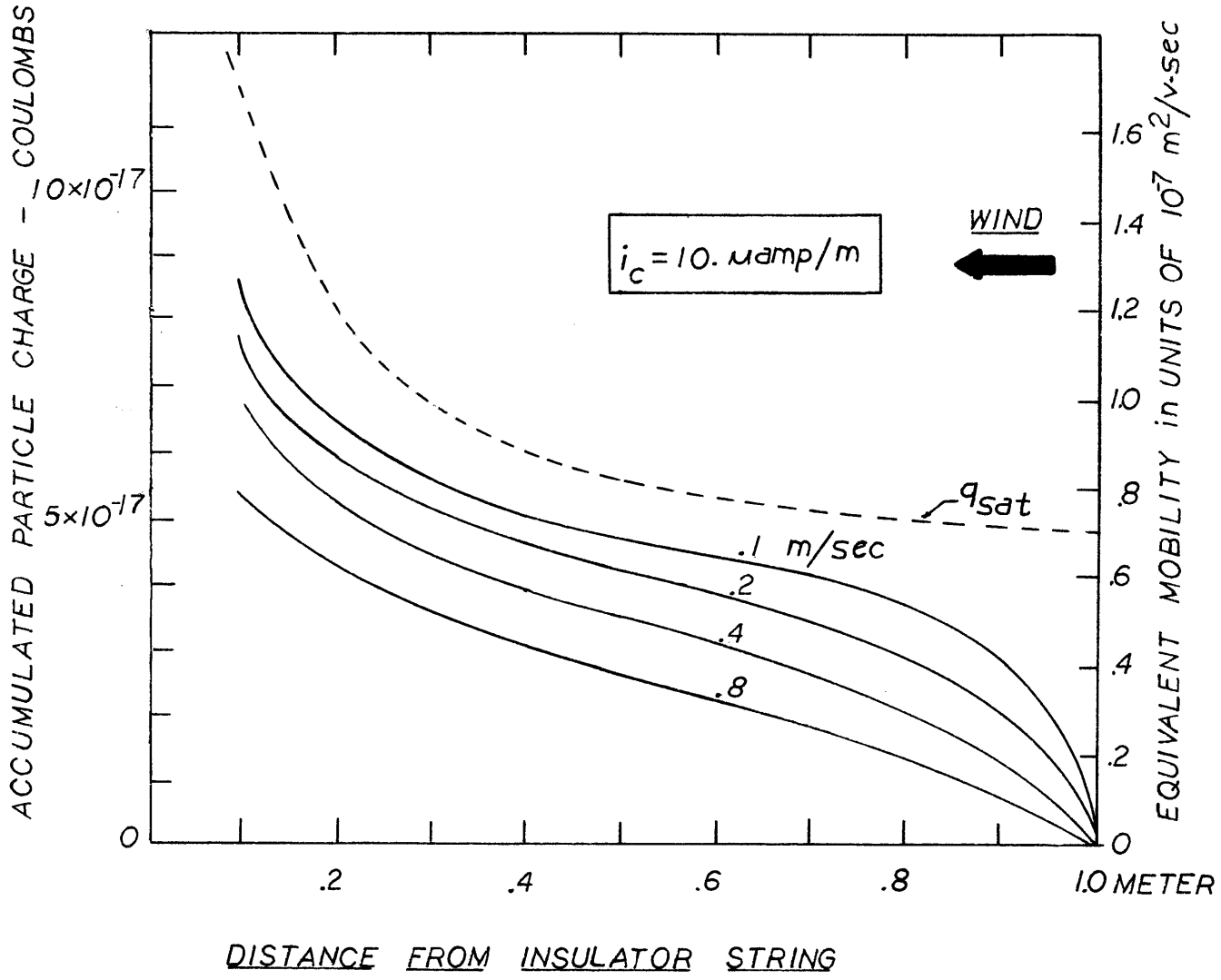

Fig. 6.3 Accumulated Charges for Intially Neutral Particles Entering at Various Wind Speeds.

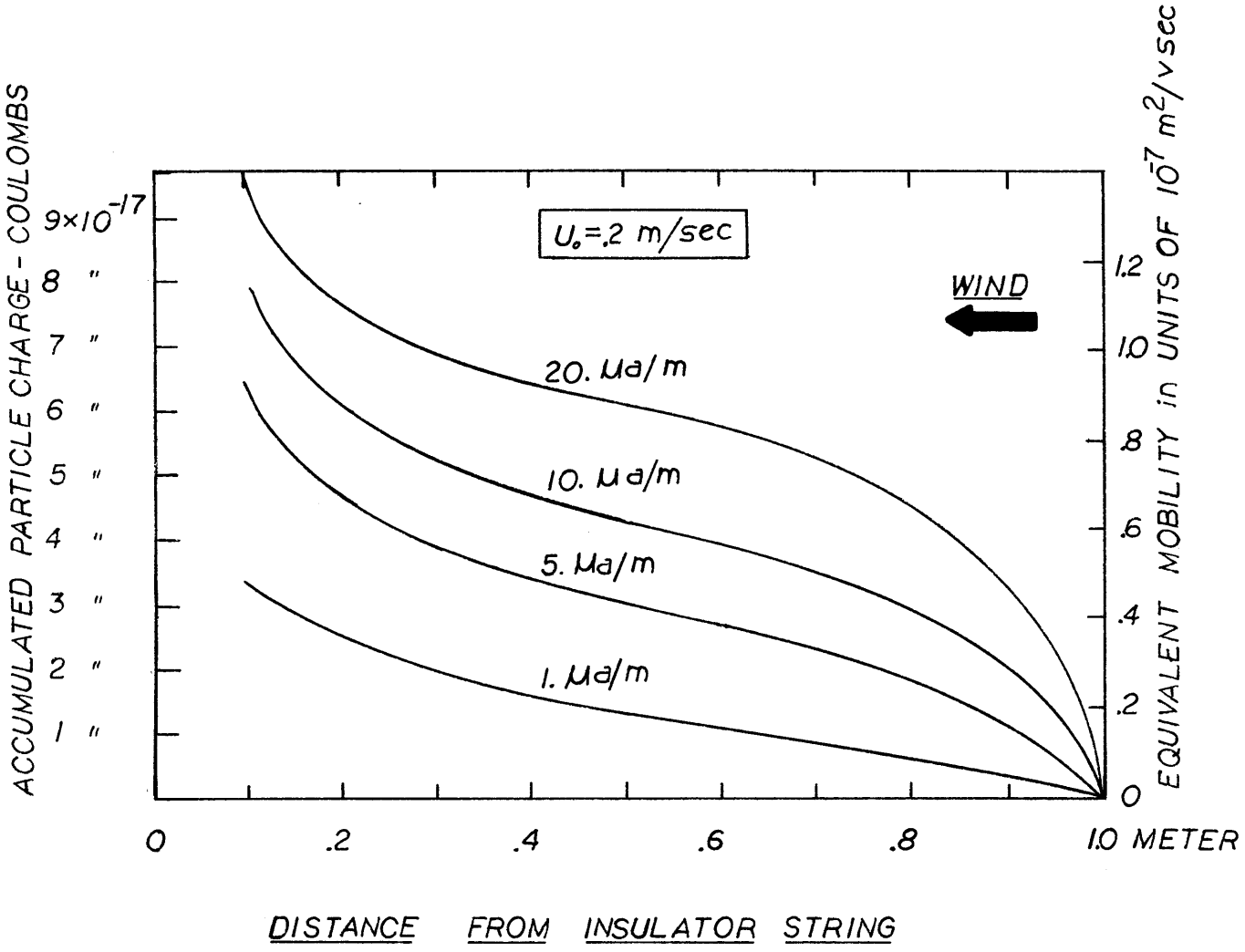

Fig. 6.4 Accumulated Charges for Initially Neutral Particles Entering at .2 m/sec, and Encountering Various Corona Fluxes

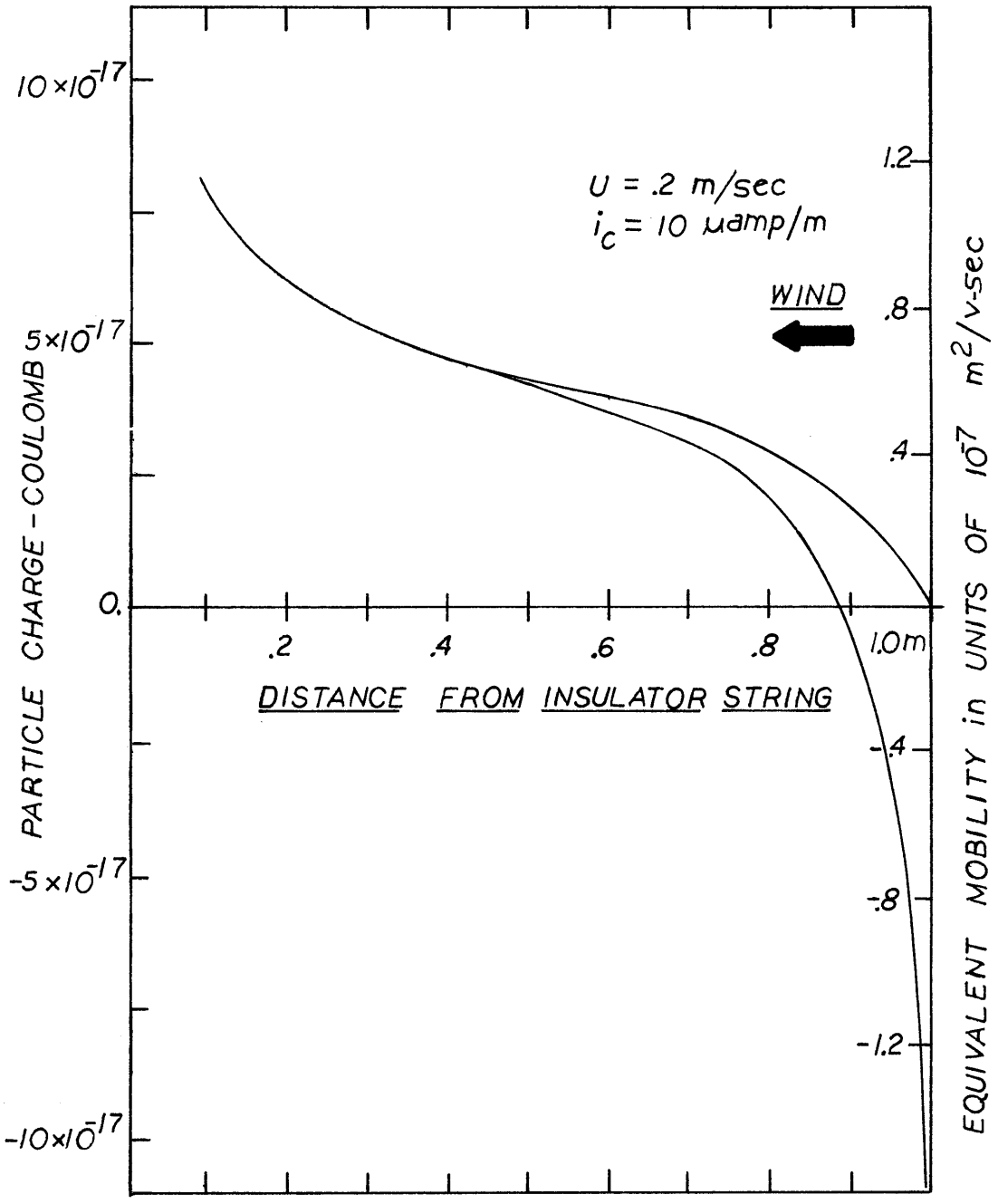

Fig. 6.5 Initially Negative and Initially Neutral Particles Encountering a Positive Corona Flux of 10 μamp/m. U = .2 m/sec

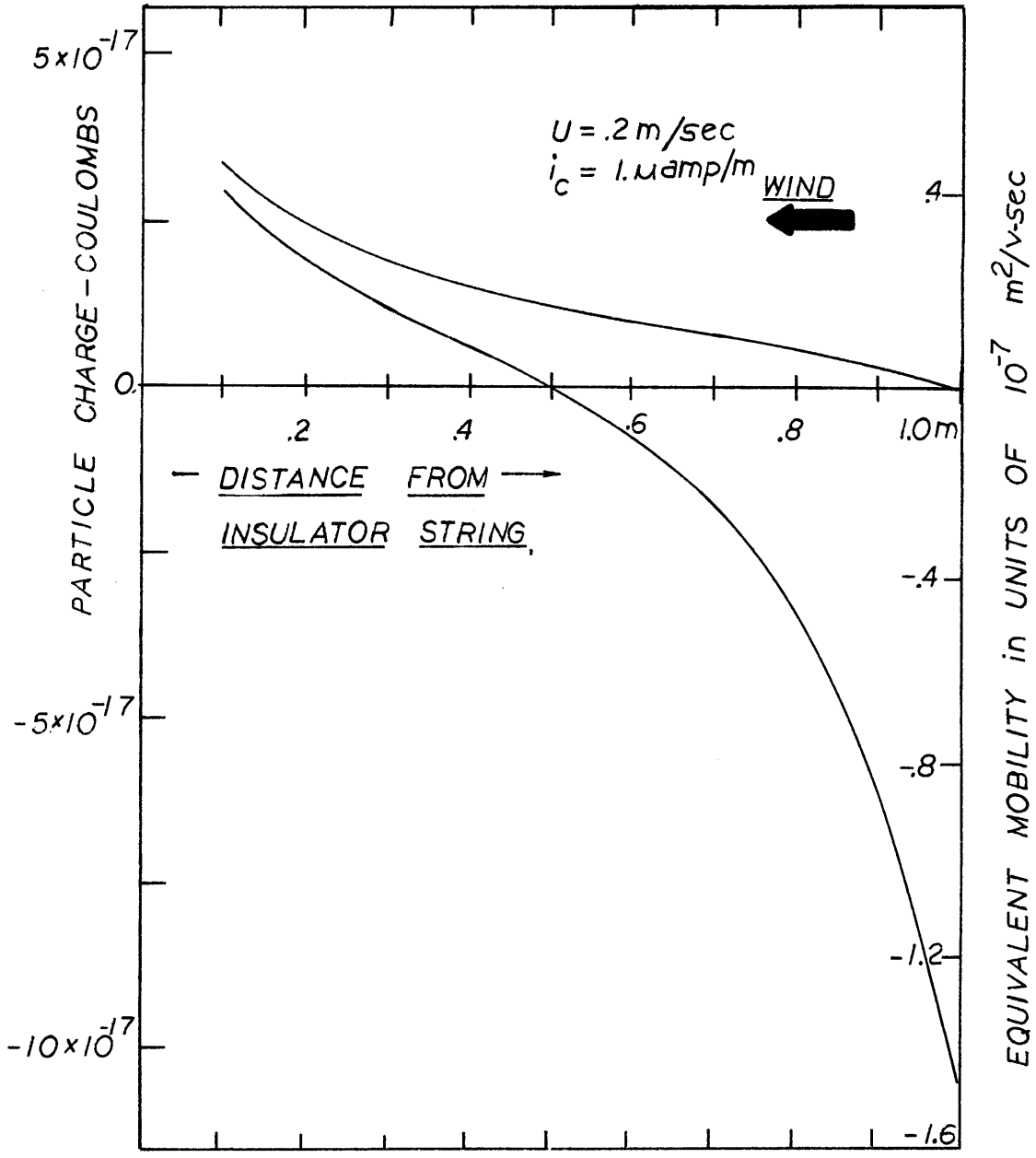

Fig. 6.6 Initially Negative and Initially Neutral Particles Encountering a Positive Corona Flux of 1 μamp/m. U = .2 m/sec

In Fig. 6.6 (i_c = 1 μamp), the discharge process is much slower, but the final charge of the initially negative particle is still very nearly equal that of the initially neutral particle.

Two conclusions may be extracted from this simple corona analysis. First, when neutral particles encounter a corona ion flux, they may acquire substantial charge before arriving in proximity to the insulator string. The mobilities of such particles can be comparable to the highest naturally occurring mobilities. Hence, any prediction of contamination at a transmission line site should evaluate the possibility that particles may be charged by corona. Second, initially charged particles of the attracted species may be rapidly discharged by the corona flux of a given line conductor, and behave thereafter as neutral particles with the possibility that they may be recharged as repelled particles. This phenomena must likewise be taken into account when predicting contamination at a transmission line site. These conclusions are of course very general statements, but consistent with the purpose of this chapter, which has been to develop the basic physical principles involved in particle charging dynamics, as summarized by Eqs. (6.30) through (6.35). To arrive at a thorough understanding and prediction of phenomena above corona threshold, the equations (6.30) - (6.35) must be applied in detail to specific insulator geometries and field computations, which include an analysis

of corona effects in the microregion, macrofield modification due to corona space charge, and the presence of both conductors of an actual bipolar line.

CHAPTER 7

CONCLUSIONS

7.1 Prediction of Contamination

Given information about appropriate parameters at a dc transmission line site, a prediction of the total mass to be deposited on the surfaces of insulator units in a particular string can be made. Such a prediction, generally valid between periods of natural insulator cleaning caused by rainfall or airborne abrasives, will be most useful when combined with knowledge about the mechanisms leading to insulator flashover. Progress in the study of dc flashover at present does not permit identification of maximum tolerable levels of contamination before flashover, but experiments indicate that both total contaminant levels and the distribution of contaminants over the insulator surfaces are important factors in dc flashover.[16,9] The models for particle contamination presented in this thesis are certainly capable of estimating such contaminant levels, provided that certain parameters are known at the transmission line site.

Accurate knowledge of the wind velocity, particle mobility, ambient particle mass density, and particle size permit accurate predictions of the deposition patterns on the insulator surfaces. Usually, however, these required parameters are neither single valued nor easy to measure. Fluctuating wind velocities, and particle mobility and size

distributions may generally be anticipated when measurements are attempted. The simplified contamination model presented in Section 5.2 is formulated to deal with the inexactness of the important parameters, and thus becomes a far more practical engineering tool than the more precise trajectory analysis. To use the simplified model, one need only measure the mass density-collection time product $\overline{\rho T}$, which was identified in Section 5.2. The product $\overline{\rho T}$ contains all the information about the particle mobility distribution, mass density, and size, and thus comprises a "figure of merit" for a given dc transmission line site, i.e. a measure of the likelihood that insulators will become contaminated and subsequently experience flashover.

The test chamber experiments, designed to accentuate the balance between wind forces and electrical forces, model abnormally low wind velocities, but the simplified contamination model is valid within the fluctuation range of all but the most minute wind velocities likely to be encountered at an actual transmission line site. Incorporated into the simplified contamination model is the fact that precipitation, where it occurs, will simply be proportional to the particle mobility times the normal component of electric field at the surface. The exact deposition patterns and demarcation boundaries on insulator surfaces are ignored in favor of an engineering approximation which assumes the entire area of a given contaminated insulator surface to be accessed by

trajectory lines. As an example of the validity of this assumption, we note that as the ambient wind velocity fluctuates, so does the boundary of the wake region. Similarly, different values of particle mobility will cause the wake boundary to change, while the wind, which may blow from different directions, will shift the relative location of the wake on the insulator surface. On the time average, therefore, one will seldom observe a distinct wake region, and ignoring it is a valid approximation.

Unless a peculiar set of circumstances dictates that major portions of insulator surface area be excluded from deposition, as would be the case, for example, with extremely low wind velocities, the simplified contamination model does a good job of estimating contamination, and has general applicability. Note that the model is also valid for extremely high wind velocities. Figure 7.1a shows a trajectory plot for:

$$b = 5 \times 10^{-7} \ m^2/v\text{-sec}$$

$$U_0 = 2.5 \ m/sec$$

i.e., a laminar wind velocity five times the highest value thusfar considered. As shown in the figure, the trajectories are almost horizontal, and most calculated trajectories will just pass by the insulator. The only ones terminating on the lower insulator surface originate in a tiny window of the macro-micro boundary, just adjacent to the lower insulator

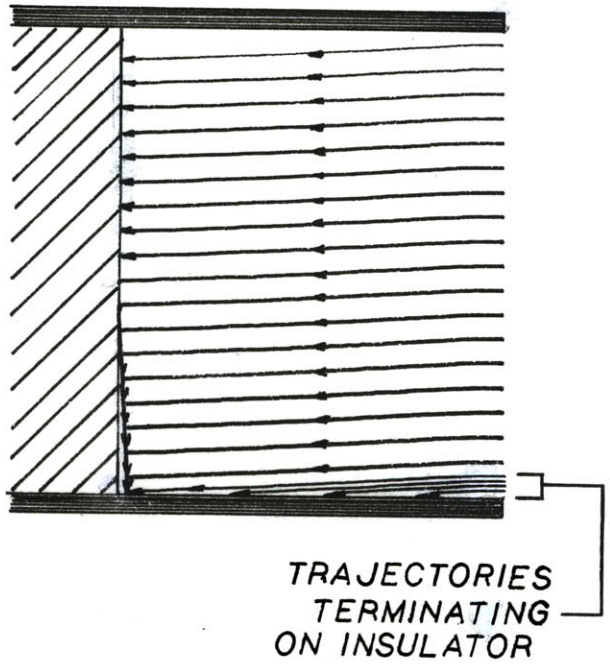

Fig. 7.1a Trajectory Plot for High Wind Velocity
U = 2.5 m/sec b = 5 x 10^{-7} m^2/v-sec

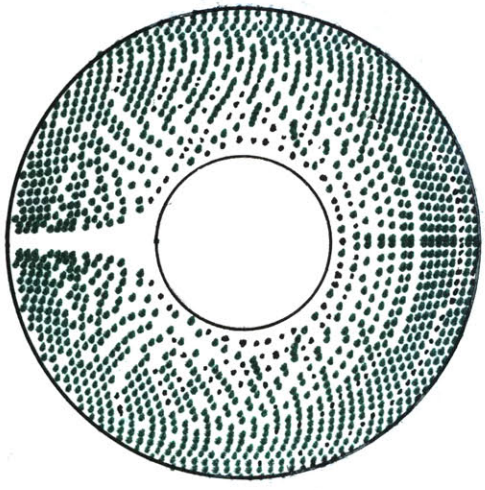

Fig. 7.1b Contamination Plot for High Wind Velocity
U = 2.5 m/sec b = 5 x 10^{-7} m^2/v-sec

disk edge. Nevertheless, the endpoints of trajectories originating in this window still form the deposition pattern shown in Fig. 7.1b, which is similar to the patterns found at lower velocities. The usual clean ring formed by the demarcation boundary on the insulator surface is extremely thin, because a much stronger wind force balances the electrical force, and the trajectory turnaround points occur much closer to the metal post. Another striking difference between Fig. 7.1b and the deposition patterns obtained at low wind velocities is the extremely narrow wake region that results at high wind speeds. In reality, the flow around the back of the metal post will be turbulent at high velocities (the associated Reynolds' number at U_0=2.5 m/sec is 1500), so the appearance of the wake in the plot is somewhat academic. Nevertheless, the mechanism of turbulent diffusion will cause particles to precipitate within the area occupied by the predicted wake, so that most all the insulator surface will experience contamination. Thus, the simplified contamination model, which approximates the deposition on a given contaminated insulator surface as occurring everywhere, is valid. The rate of precipitation, where it occurs, is still equal to $\rho b E_{\perp}$. The discussion at the end of Chapter 4 prevails, i.e. at very high wind velocities, the apparent number of trajectories intersecting the insulator surface is greatly diminished, but the transport of particles by the trajectories is very much faster. Hence, at regions of the insulator surface where trajectories terminate,

a constant particle density ρ is maintained, and pulled to the surface by the normal component of electric field.

Even for completely turbulent windflows, which might be initiated at higher wind velocities, the simplified contamination model is appropriate, because the local mixing model, introduced in Section 4.3 to deal with turbulent flows, indicates the deposition of particles to again occur wherever $\bar{n}\cdot b\bar{E}$ is negative, and to be proportional to $\rho bE_{\perp}$. In fact, the simplified contamination model may be more accurate for turbulent flows than for laminar flows, because contamination free areas like the wake region, ignored when estimating net contamination, may in fact be contaminated when the wind flow creates turbulence capable of diffusing particles into regions forbidden by laminar windflows.

The segregation effect observed in the experiments and analyzed in Section 5.3, while of significant academic interest, is expected to be of secondary concern in the prediction of insulator contamination on actual transmission lines. The experiment and analysis both focus on just single values of particle mobility and wind velocity at any given time. The multiplicity of fluctuating wind velocities and particle mobilities likely to be found around an actual line will tend to smear out the contaminant distributions observed at any one wind velocity and particle mobility. For example, the numerical simulation used in Section 5.3 to obtain the contaminant distributions of Fig. 5.11 yields, for the high wind velocity

case $U_0 = 2.5$ m/sec, essentially a uniform contaminant distribution level over the length of the insulator string. This result is to be expected, given the mechanisms held responsible for the segregation effect. Thus the degree to which a given particle species with a distribution of mobilities is segregated, on the time average, will depend on the percentage of time that the ambient wind velocity is high or low. Typically, predictions of contamination will be implemented so as to insure that contaminant levels on a given string will not exceed some maximum safety margin level. Hence, to what is again a first order engineering approximation, it is practical to neglect segregation when predicting contaminant levels on a real line.

Exceptions to this rule might arise at a site where, for example, the predominant wind velocities were very low, and the prominent naturally charged particles were all of one sign. In such a case the segregation effect should certainly be observed to some degree, with the possible effect of significantly altering the voltage distribution along the insulator string, as deposited contaminant layers begin to dictate the potential distribution along the insulator surfaces.

7.2 Correlation Between Experimental Work and Actual Field Data

The theories presented in this thesis agree well with the controlled scale model experiments, but little if any data from actual dc transmission lines exists for comparison,

largely because only one dc line is at present operational in the U.S., and only several worldwide. Limited field tests have begun at the Sylmar, California dc converter station, but the body of data, compiled primarily for flashover studies, is not at present substantial enough to be useful for contamination work. Field measurements specifically aimed at confirming the contamination theories presented here must eventually be made. For example, a simple method should be designed for measuring the $\overline{\rho T}$ product at a given transmission line site. A measurement of the net mass increase of control electrodes of both positive and negative polarity, energized to a known value of normal electric field, and placed onsite in a configuration so as to be accessed by particle lines for most all wind velocities, should be sufficient. Such a measurement would provide data on the relative ratio of positive to negatively charged particles--important for determining the ratio of top to bottom surface contamination that will occur on a given string between periods of natural cleaning by rainfall.

At the same time, the control electrodes would provide valuable samples of the local contaminants, which could be used to determine their chemical composition, without the cumbersome manipulation of actual energized insulators presently used to collect onsite contaminants. The details of such a controlled electrode scheme need be refined before implementation, but the measurement would be useful in both the

analysis of contamination problems on the existing Pacific Intertie line, and the evaluation of proposed future dc transmission line sites.

The origins of contaminant particles and the mechanisms by which they become naturally charged and airborne are still somewhat of a mystery. An investigation of this topic would be worthwhile, especially if correlatable to onsite measurements of the $\overline{\rho T}$ product. The existence of air turbulence would likely be important to such an analysis of particle generation and transport; similarly any modifications to the trajectory theories caused by the existence of turbulence should be investigated before complete contamination predictions are made.

7.3 Design Concepts for Improved DC Insulators

The underlying conclusion to be drawn from both the simplified contamination model, and the more exact trajectory analysis, is that contamination can be substantially reduced by minimizing the normal electric field on the insulator surfaces. This seemingly obvious conclusion may now be stated with confidence, given the body of knowledge presented within this thesis, which has demonstrated both theoretically and experimentally the fundamental role of the normal electric field in the contamination process. Accomplishing such a reduction of normal field in practice may require radical changes in the way dc insulators are designed. One such design concept is

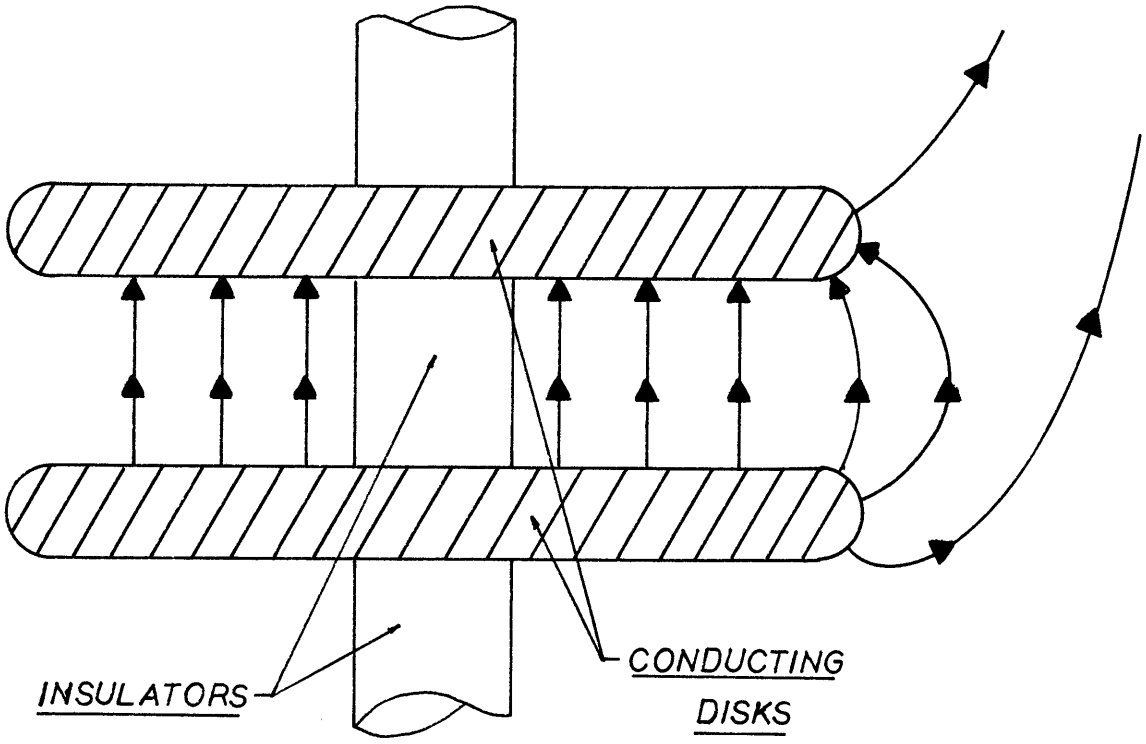

Fig. 7.2 Insulator String Exhibiting Improved DC Design Concept. Normal Electric Field on Insulating Surfaces is Minimized, if Surface Conductivity of Insulators is Uniform.

depicted, for example, in the insulator string of Fig. 7.2, in which metal surfaces and insulating surfaces are inverted. In the vicinity of the critical post surfaces, the field is predominantly uniform and tangential, hence $E_{\perp}$ is essentially zero, and little if any contamination should be expected on the insulating surfaces. The contamination of the metal surfaces would of course be of no consequence. The success of the insulator string depicted in Fig. 7.2 lies in the ability to distribute evenly the surface potential drop along the insulating surface between each pair of disks, so that no normal field component results on the insulating surface. The usefulness of such a design also depends on how much reduction in creepage path length, as compared to standard disk suspension insulators, can be tolerated in responsible transmission line designs. Much work must precede the implementation of such an insulator design, but the fundamental nature of the concepts should be evident and applicable to future designs of dc insulators.

APPENDIX A

SUMMARY OF PARTICLE CHARGING PRINCIPLES

A knowledge of how contaminant dust particles are charged by a flux of ions in an electric field is required for an understanding of the particle charging device of Section 3.4, and also for the analysis of the effects of corona current on the contamination process. The problem is a classic one which was originally examined by Whipple and Chalmers[32] as applied to the charging of water droplets in thunderclouds. A thorough generalization and rigorous mathematical treatment of droplet charging has been assembled by Melcher.[19] For typical values of wind velocity and electric field found both in nature and the scale model experiment, several simplifications of the charging theory may be justified, such that only a small subset of the formulation need be offered here. The reader is directed to the above references for a more detailed discussion.

In Chapter 4, a trajectory analysis was developed for examining the behavior of charged contaminant particles of mobility "b" in a given wind velocity distribution and electric field. The analysis also applies to the motion of ions, although the mobility of the ions in this case is much greater than that of the contaminant particles. For a singly ionized positive or negative oxygen ion in air, $|b_{ion}| \approx 1.4 \times 10^{-4}$ $m^2/v\text{-sec}$,[19] as compared to $|b| \approx 5 \times 10^{-7}$ for a typical charged contaminant particle.

Contaminant particles can be modeled as conducting spheres. (This assumption will be justified later). Let an uncharged one be situated in a uniform electric field E_o, and a uniform, homogeneous source of ions be located at the source of the ambient field lines. The density of these ions must of course be small enough to cause a negligible perturbation to the imposed field E_o. In real situations the electric field is rarely uniform, but as long as its magnitude does not change appreciably over several particle diameters, the analysis here will apply at the location of the particle. Invariably, the contaminant particles will also be found where the wind is nonzero, and the ion motion in the wind should be taken into account. The motion of an ion can thus be described by the same trajectory equation developed in Chapter 4:

$$\frac{d\bar{x}}{dt} = (\bar{v} + b_{ion}\,\bar{E}) \qquad (A.1)$$

Note that all the theorems and definitions applicable to contaminant particle trajectories may thus also be applied to the ion trajectories. In most cases of interest, the component of $\frac{d\bar{x}}{dt}$ due to wind velocity is much less than any ion velocity due to the electric field. For example, in the particle charging device, $E_o \approx 3 \times 10^5$ V/m, and $b_{ion}\,E \approx 42$ m/sec, equivalent to an air velocity of about 100 MPH. In the test chamber, the weakest fields encountered are on the

order of 5×10^4 V/m, leading to ion velocities on the order of 6 m/sec--at least ten times the ambient wind velocity. Hence, for all practical purposes, $|b_{ion}\,\bar{E}| >> |\bar{v}|$ at all times, and

$$\frac{d\bar{x}}{dt} \approx b_{ion}\,\bar{E} \tag{A.2}$$

The electric field solution for the idealized conducting particle can be written as a superposition of the spherical harmonic solution and the field due to any charge accumulated on the particle. Hence, in the neighborhood of the particle, ion trajectories are given by Eq. (A.2):

$$\frac{d\bar{x}}{dt} = b\left[E_o\left(1 + \frac{2\,R_p^3}{r^3}\right)\cos\theta + \frac{q}{4\pi\varepsilon_o\, r^2}\right]\hat{i}_r + b\left[E_o\left(\frac{R_p^3}{r^3} - 1\right)\sin\theta\right]\hat{i}_\theta \tag{A.3}$$

where R_p is the radius of the particle, q is the charge accumulated on the particle, the coordinates are as defined in Fig. A.1, and once again, b reflects the sign of the ions.

For the remainder of this section, the subscript "ion" will be dropped from the ion mobility, with the understanding that $b \equiv b_{ion}$. Also, the charging functions will be developed for a particle experiencing a positive ion flux, although the results apply equally well to particles in a negative ion flux, with the understanding that "q" refers to the

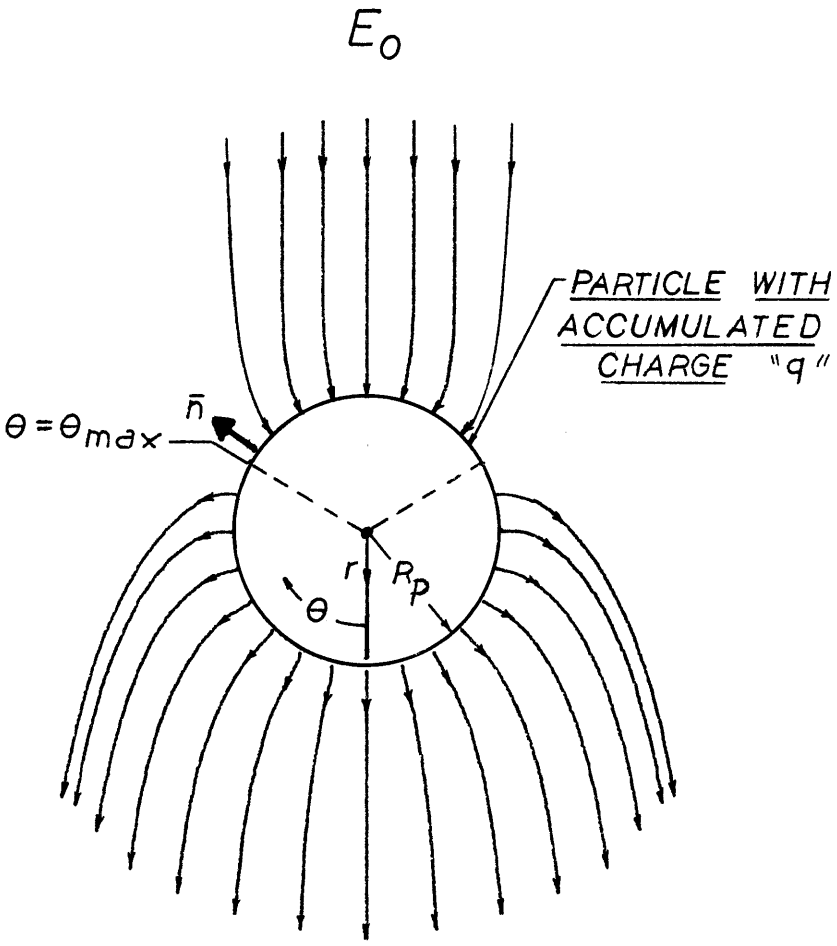

Fig. A.1 Partially Charged Particle in a Uniform Electric Field and Ion Flux

magnitude of the negative charge on the particle.

Let $\bar{n}$ be an outward normal vector at the surface of the conducting spherical particle. Then ions may only be carried to the surface of the particle at regions on the surface where

$$\bar{n} \cdot b\bar{E} < 0$$

As shown in Fig. A.1, this surface region of entering trajectory lines is bounded by a ring of demarcation at $\theta = \theta_{max}$, inside of which all trajectories originate on the particle surface, and carry no ions. The location of θ_{max} is given by the zero field (critical) point:

$$E_r\Big|_{r=R_p} = 3\, E_o \cos \theta_{max} + \frac{q}{4\pi\varepsilon_o R_p^2} = 0$$

or

$$\cos \theta_{max} = \frac{-q}{q_{sat}} \qquad \text{(A.4)}$$

where $q_{sat} = 12\pi\varepsilon_o R_p^2 E_o$. The value of θ_{max} will increase as more ions are carried to the particle thereby changing the amount of accumulated charge q, until $q = q_{sat}$, and $\theta_{max} = \pi$. At this point the particle can accept no more charge.

The rate of particle charging may be computed by invoking the theorem developed in Chapter 4, this time restated so as to apply to ion flow: Along any trajectory line

carrying ions, the density of ions remains constant. Hence the flow of charge to the particle is determined by integrating the inward normal component of current density at the particle surface:

$$-n\cdot\bar{J} = -(Ne)bE_r \tag{A.5}$$

where e is the electronic charge. In this case, according to the theorem, N at the particle surface is identical to that at the source of ions. Thus

$$\frac{dq}{dt} = -\int_S n \cdot \bar{J}\ dA$$

$$\frac{dq}{dt} = \int_{\phi=0}^{2\pi} \int_{\theta=\theta_{max}}^{\theta=\pi} -n\cdot\bar{J}\ R_p^2 \sin\theta\ d\theta\ d\phi \tag{A.6}$$

$$= 2\pi\ Neb \int_{\theta=\theta_{max}}^{\theta=\pi} -\left[3E_o \cos\theta + \frac{q}{4\pi\varepsilon_o R_p^2}\right] R_p^2 \sin\theta\ d\theta$$

Solution of the integral yields the charging current to the particle:

$$i_c = \frac{dq}{dt} = 3\pi R_p^2 E_o Neb \left(1 - \frac{q}{q_{sat}}\right)^2 \tag{A.7}$$

where use of Eq. (A.4) has been invoked. Note that (A.6) and (A.7) are valid only for $-q_{sat} \le q \le q_{sat}$. As discussed

previously,

$$\frac{dq}{dt} = 0 \qquad \text{for} \qquad q > q_{sat} \tag{A.8}$$

For $q < -q_{sat}$, $\theta_{max} = \pi$, and it can be shown by integrating (A.6) from $\theta = 0$ to $\theta = \pi$ that:

$$\frac{dq}{dt} = -\frac{Neb}{\varepsilon_o} q \qquad \text{for } q < -q_{sat} \tag{A.9}$$

The solutions to the differential equations (A.7) through (A.9) yield the charging laws for the particle as a function of time:

$$q = \text{constant} \qquad q > q_{sat} \tag{A.10}$$

$$q = 3\pi R_p^2 E_o Neb \left[\frac{t}{\frac{Neb}{4\varepsilon_o} t + 1}\right] \qquad -q_{sat} \leq q \leq q_{sat} \tag{A.11}$$

$$q = q_o e^{-(\frac{Neb}{\varepsilon_o})t} \qquad q < -q_{sat} \tag{A.12}$$

Note the charging law for an initially neutral particle, (A.11) is hyperbolic, rather than exponential. It is thus a relatively slow function of time, characterized by the hyperbolic time constant $\tau = \frac{Neb}{4\varepsilon_o}$, as was pointed out in Fig. 3.8b. Moreover, Eq. (A.12), which describes how an initially charged particle situated in an oppositely charged ion flux discharges

to $-q_{sat}$, is a rather fast exponential in time.

The justification for modeling the contaminant particle as a conducting sphere can now be examined by noting that charge is carried to the particle on a time scale characterized by the time constant $\tau = \frac{Neb}{4\varepsilon_o}$, but the charges distribute themselves on the particle surface within a time scale characterized by a relaxation time $\tau = \frac{\varepsilon_o}{\sigma_s} R_p \sim 2 \times 10^{-4}$ sec where σ_s is the surface conductivity of a typical contaminant particle. The conducting sphere approximation thus appears valid.

APPENDIX B

PROOF OF INVARIANCE OF TRAJECTORY VECTOR POTENTIAL - EQUATION (4.21)

Solenoidal electric field and wind flows may generally be expressed as the curl of vector potentials $\bar{A}_E$ and $\bar{A}_v$ respectively. In polar coordinates in the steady state, where $\bar{E}$ and $\bar{v}$ have r and θ components only, $\bar{A}_E$ and $\bar{A}_v$ will have only time independent z components, so that:

$$\bar{E} = \nabla \times (A_E \hat{i}z) = \frac{1}{r} \frac{\partial}{\partial \theta} A_E \hat{i}_r - \frac{\partial}{\partial r} A_E \hat{i}\theta \qquad (B.1)$$

$$\bar{v} = \nabla \times (A_v \hat{i}z) = \frac{1}{r} \frac{\partial}{\partial \theta} A_v \hat{i}r - \frac{\partial}{\partial r} A_v \hat{i}\theta \qquad (B.2)$$

The components of the trajectory equation

$$\frac{d\bar{x}}{dt} = \bar{v} + b\bar{E} \qquad (B.3)$$

thus become:

$$\frac{dr}{dt} = \frac{1}{r} \frac{\partial}{\partial \theta} [A_v + b\, A_E] \qquad (B.4)$$

$$r \frac{d\theta}{dt} = - \frac{\partial}{\partial r} [A_v + b\, A_E] \qquad (B.5)$$

Since A_v and A_E do not change with time, we may solve (B.4) and (B.5) for dt, and equate them:

$$\frac{dr}{\frac{1}{r}\frac{\partial}{\partial\theta}(A_v + b\,A_E)} = \frac{-\,r d\theta}{\frac{\partial}{\partial r}(A_v + b\,A_E)} \qquad (B.6)$$

or $$\frac{\partial}{\partial r}(A_v + b\,A_E)\,dr + \frac{\partial}{\partial\theta}(A_v + b\,A_E)\,d\theta = 0 \qquad (B.7)$$

The expression (B.7) is a total differential, whence, if we follow along a trajectory line, as per Eq. (B.3), we note that:

$$d(\bar{A}_v + b\,\bar{A}_E) = 0 \qquad (B.8)$$

along $$\frac{d\bar{x}}{dt} = \bar{v} + b\bar{E}$$

APPENDIX C

MEASUREMENTS OF VOLTAGE DISTRIBUTION ALONG A SCALE MODEL INSULATOR STRING

Interpreting the results of the contamination experiments requires estimating the electric field between any two insulators along an energized string. As shown in Section 4.6, suitable assumptions regarding the nature of the field lead to a solution that can be obtained without the aid of a computer. Implicit in this solution, however, is a knowledge of the voltage existing between the metal fittings of each insulator. While the voltage distribution along an ac string will be dominated by the various capacitances,[6] the voltage distribution along a dc string will be dominated, in a first order approximation, by the resistance present between the terminals of each insulator -- the string forms, in essence, a resistive divider chain where each insulator may be modeled as a lumped element resistor. The voltage distribution along an initially energized string will reach the final equilibrium in a time scale determined by these resistances and the equivalent insulator capacitances.

As discussed in Section 2.6, the resistance of glass-like insulating materials is usually dominated by a conducting surface layer formed by adsorbed moisture and contaminants, which produces surface resistivities that can be several orders of magnitude lower than the bulk substrate resistance. If the insulators are all constructed alike of

similar materials, one may expect their equivalent resistances to be the same. The applied line voltage therefore will divide equally between each insulator. This simplified picture neglects secondary effects that may take place in the surface conducting layer. Surface resistivity may not be constant in time, for example, but may increase after the voltage is applied and localized ohmic heating dries out some of the adsorbed moisture layer. Likewise, surface and bulk-to-surface migration of conducting ions may occur, thereby causing the surface resistivity to change with time. The degree to which the uniform voltage distribution along the string will be altered depends on whether these secondary processes affect all insulators equally. The study of these processes could be the subject of a separate, major investigation; for our purposes in contamination work it appears reasonable to measure experimentally the voltage distribution along the string, and assess its deviation from uniformity.

A generating voltmeter (GVM) designed specifically to accomplish this task is sketched in Fig. C.1. Generating voltmeters are commonly used to measure kilovolt levels of voltage, where ultra-high input impedance is required.[29] The insulating posts of the GVM completely determine the dc input resistance. They are made from plexiglas coated with parafin, and are specially designed to have an extra long leakage path. The first step in the experimental process was to determine both the input resistance R_m, and input

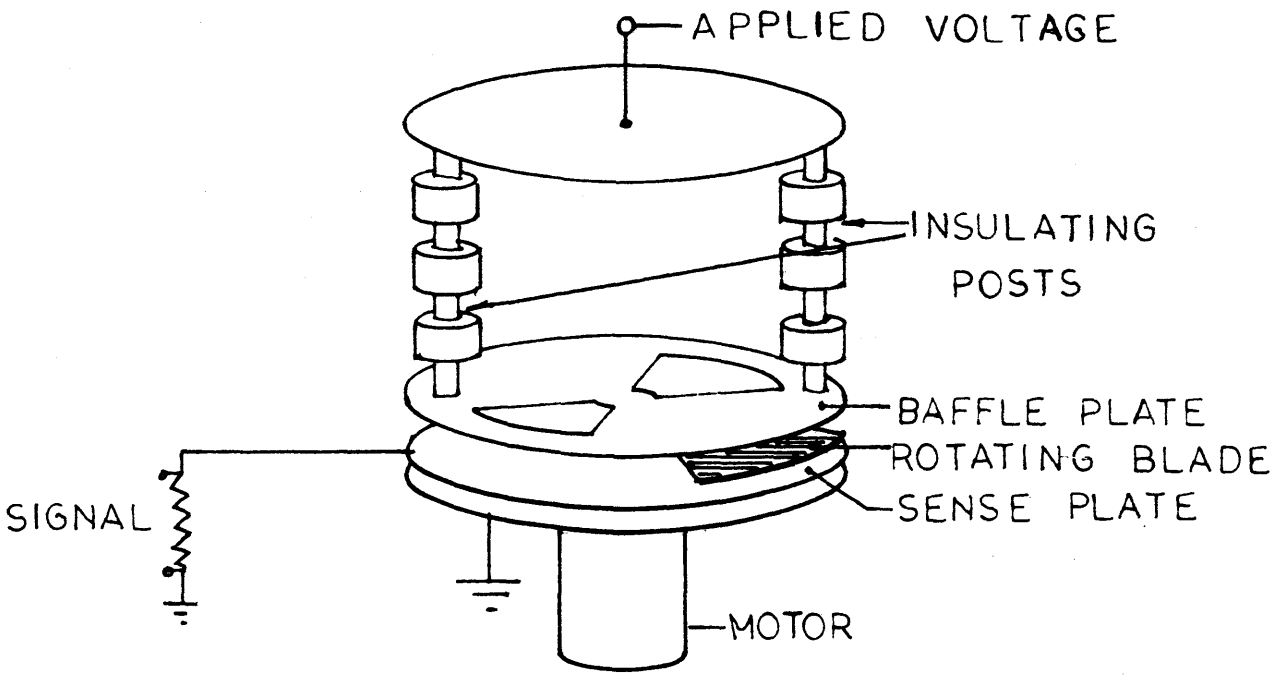

Fig. C.1 Generating Voltmeter (GVM)

capacitance C_m of the GVM. The value of C_m was measured on a GR bridge and found to be equal to about 25 pf. By energizing the GVM and measuring its own self-RC decay time, the resistance R_m was found to be equal to about 2×10^{14} ohms at 50% relative humidity.

The GVM was next connected to the midpoint of the insulator string via a specially designed probe, designed to minimally distort the electric field around the insulator string, and thus have a very small capacitance. The equivalent circuit so formed is depicted in Fig. C.2. The decaying voltages in arbitrary units for both the GVM alone, and with the insulator string connected, are plotted in Fig. C.3. From these plots it is evident that the equivalent resistance presented by the insulator string is much smaller than that of the GVM at the given relative humidity of 50%. Hence resistive loading by the GVM should be minimal, and the effect of its capacitance merely to alter the time after energization required for the voltage distribution along the string to come to equilibrium.

Fortunately, this time constant is not extremely large. Also plotted in Fig. C.3 is the voltage after energization, vs. time, as measured on the GVM, in the same arbitrary units, with the probe in the same position between two insulators. As is evident from the plot, the voltage at this position appears to reach equilibrium after about 400 seconds - a lengthy but not hopelessly inconvenient period of

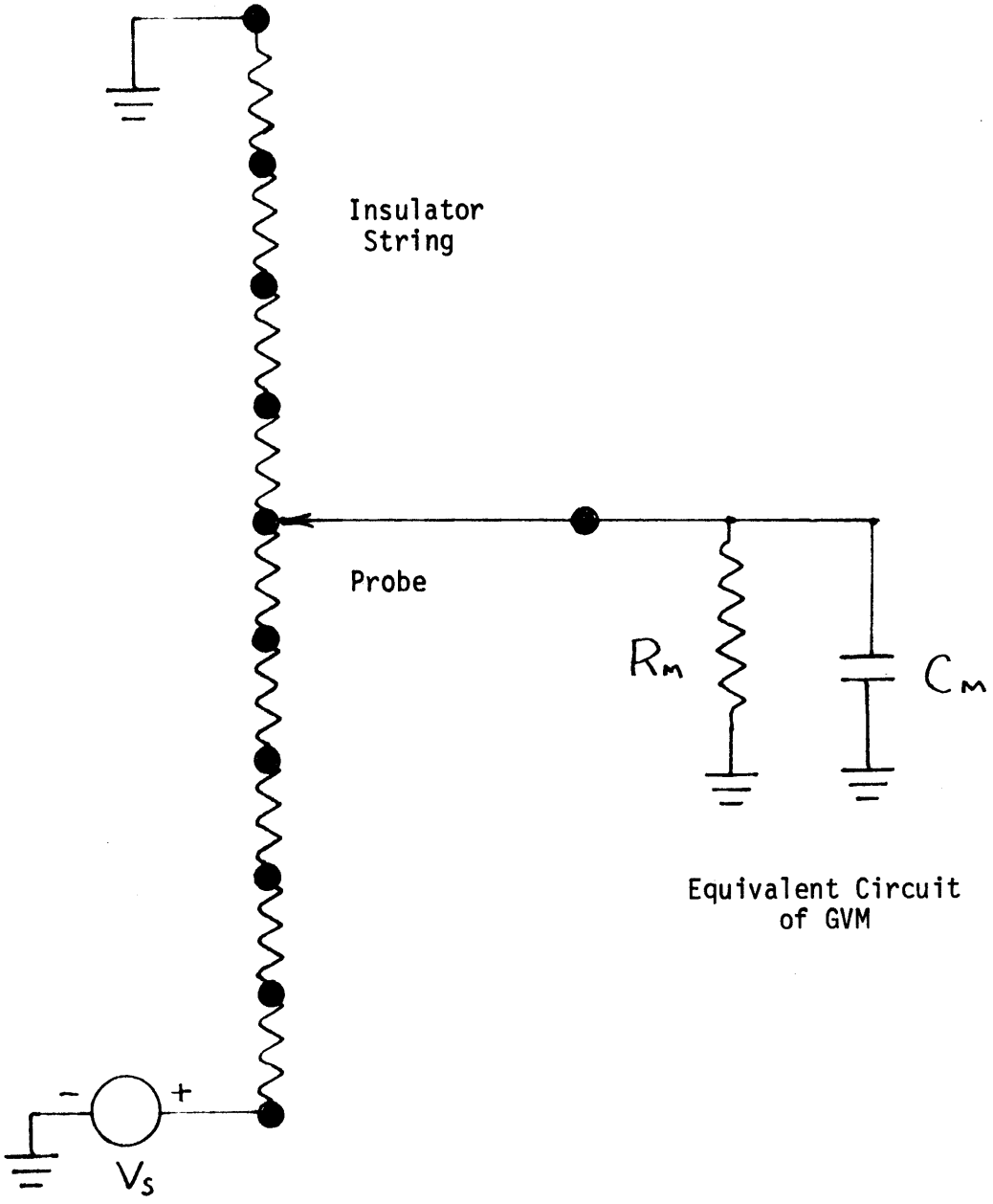

Fig. C.2 GVM Loading Problem

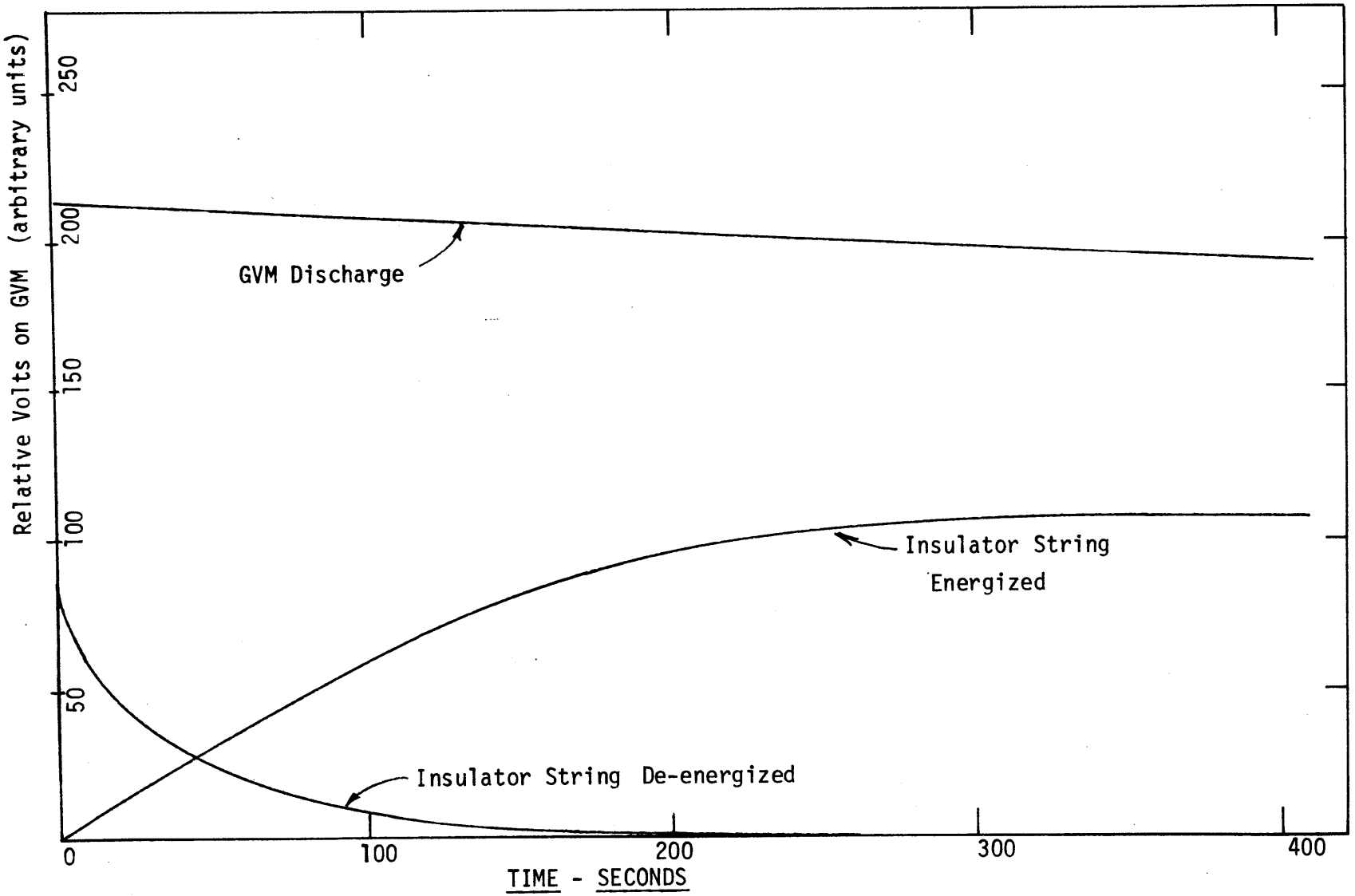

Figure C.3 Time Constant Measurements

time. One result of interest observable on these plots is that the decay time and rise time measured on the insulator string are not identical exponentials. Were the components of the system to be pure resistances and capacitances, one would expect that they should be. The discrepancy is evidence that some sort of secondary surface effect may take place on the insulator units, although no attempt has been made to identify or analyze the specific process.

The set of relative voltages, obtained as described above for each point along the insulator string, with 10 kV applied to the entire string, is plotted in Fig. C.4. Clearly, the distribution appears to be linear. This result will be useful in estimating the electric field magnitude between each pair of insulators, and therefore in interpreting the contamination data.

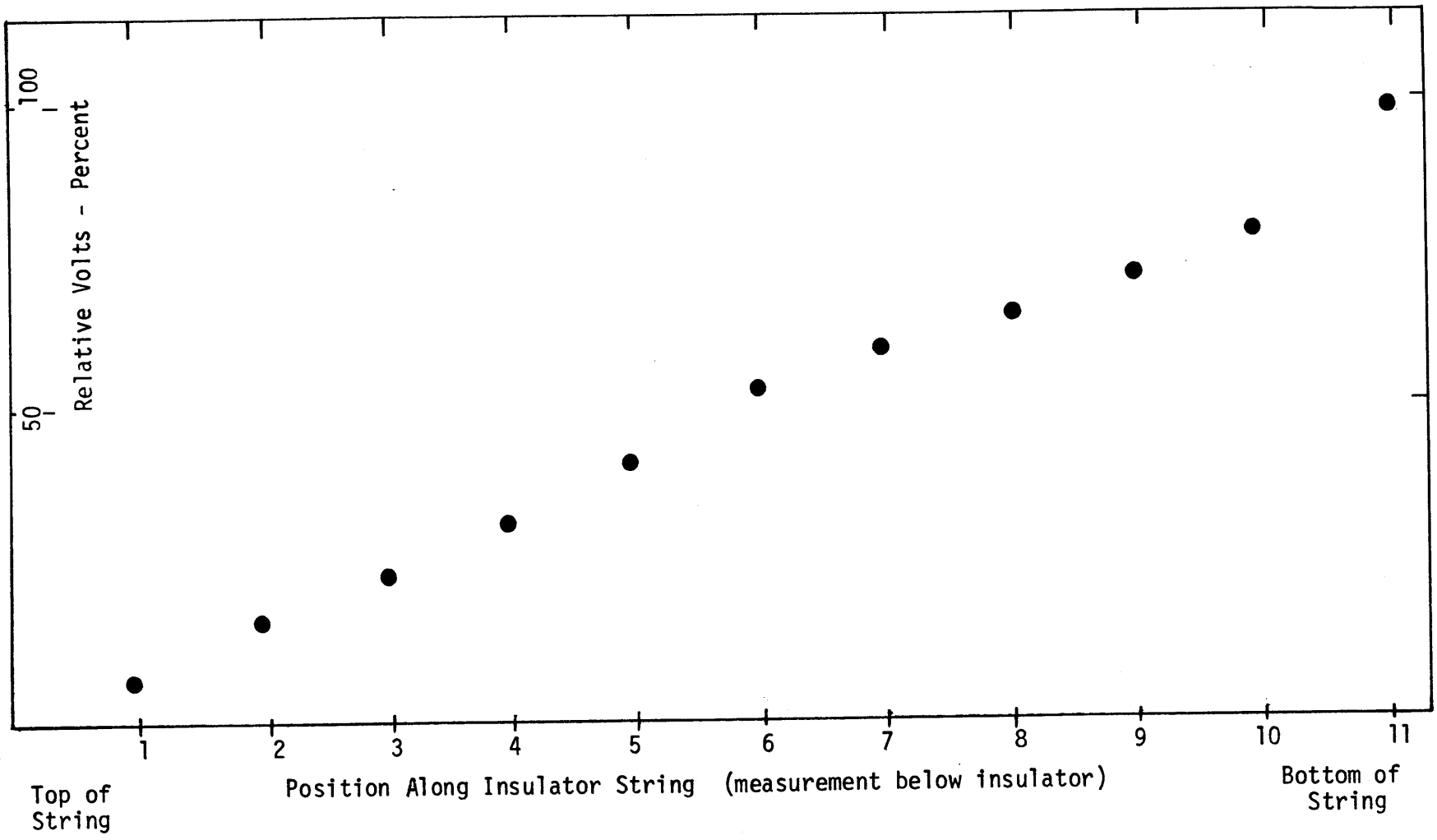

Figure C.4 Measured Voltage Distribution

REFERENCES

1. A. Annestrand and A. Schei, "A Test Procedure for Artificial Pollution Tests on Direct Voltage," Direct Current, Vol. 12, (1), pp 1-8, February 1967.

2. B.M. Bailey, "Progress Report on BPA HV DC Test Line - Radio Noise and Corona Loss," PAS, Vol. 86, (10), pp 1141-1145, October 1967.

3. C.H. Bartlett, Rev. Sci. Instr., Vol. 3, (10), pp 543-552, October 1932.

4. G.K. Batchelor, An Introduction to Fluid Dynamics, Cambridge: Cambridge Univ. Press, 1967, pp 230-235.

5. I.A. Black, "The Voltage Distribution on Insulators Subjected to a High Direct Voltage," Direct Current, Vol. 1 (new series), (3), pp 99-104, February 1970.

6. E.W. Boehne and G.S. Weiner, "Contamination of EHV Insulation - I - An Analytical Study," Paper No. (31 - pp 66-481), IEEE Summer Power Meeting, July 1966.

7. D.J. Bosack, "Acoustic Noise from Corona on Electric Power Transmission Lines," Ph.D Thesis, MIT, January 1976.

8. "Celilo Converter Station," an informal pamphlet published by U.S. Dept. of the Interior and Bonneville Power Administration, August 1970.

9. T.C. Cheng, "A Study of Insulator Flashover Under Contaminated and HVDC Conditions," EPRI Report IP 848-1, QPR 6, February-April 1977.

10. J.D. Cobine, Gaseous Conductors, New York: Dover Pub., 1958, pp 252-281.

11. H.L. Curtis, "Insulating Properties of Solid Dielectrics," Bull. Bureau Stds., Vol. 11, p. 359, 1915.

12. F.J. Ellert and N.G. Hingorani, "HVDC for the Long Run," IEEE Spectrum, pp 36-42, August 1976.

13. B.C. Furumasu, "Contamination Mechanisms for High Voltage Direct Current Insulators," M.S. Thesis, Washington State University, 1977.

14. M.N. Horenstein, "Summary of Theoretical Model and Qualitative Experimental Deposition Studies," Report on ERDA Contract No. E(49-18)-2068, December 1976.

15. H. Haerer, "Insulators for High Voltage Direct Current Under Contamination Conditions," Ph.D Thesis, Univ. of Stuttgart, July 1971.

16. D.C. Jolly, "Contamination Flashover Mechanisms of DC Transmission Line Insulators," U.S. Dept. of Energy Report No. HCP/T-2068/1, January 1978.

17. D.O. Lavelle, "Thermal Considerations in the Surface Behavior of Insulators," Ph.D Thesis, Queen's Univ. of Belfast, October 1970.

18. J.R. Melcher and E.J. McHale, "Physical Processes and Scaling Laws Relevant to Deposition of Contamination of HVDC Insulators," Internal Memorandum, EPSEL/CEL, MIT, June 1976.

19. J.R. Melcher, Continuum Electromechanics, to be published.

20. P. Moon and D.E. Spencer, Field Theory for Engineers, Princeton, N.J: D. Van Nostrand, 1961, pp 372-376.

21. F. Ollendorff, "Potentialfelder Der Elektrotechnik," Verlag von Julius Springer, 1932.

22. R.G. Olsen and J. Daffe, "The Effect of Electric Field Modification and Wind on the HVDC Insulator Contamination Process," IEEE Winter Power Meeting, February 1978, Paper No. A 78 120-8.

23. F.W. Peek, Jr., Dielectric Phenomena in High Voltage Engineering, New York: McGraw Hill, 1929, pp 54-61.

24. D.Y.H. Pui, "Experimental Study of Diffusion Charging of Aerosols," Particle Technology Lab Pub. No. 289, Univ. of Minnesota, March 1976.

25. W.M. Rohsenow and H.Y. Choi, Heat, Mass, and Momentum Transfer, Englewood Cliffs, N.J: Prentice Hall, 1961.

26. H.E. Rose and A.J. Wood, Electrostatic Precipitation in Theory and Practice, London: Constable and Co., 1966, pp 138-139.

27. E.C. Salthouse, "The Effects of Direct Voltages on Insulator Surfaces," Ph.D Thesis, Queen's Univ. of Belfast, November 1960.

28. E.C. Salthouse, "Initiation of Dry Bands on Polluted Insulation," Proc. IEE, Vol. 115, (11), pp 1707-1712, November 1968.

29. A.J. Schwab, High Voltage Measurement Techniques, Cambridge, Mass: MIT Press, 1972, pp 141-146.

30. H. Singer, H. Steinbigler, and P. Weiss, "A Charge Simulation Method for the Calculation of High Voltage Fields," PAS, Vol. 93, (5), pp 1660-1668, September/October 1974.

31. V.L. Streeter, Fluid Mechanics, New York : McGraw Hill, 1962, pp 196-200.

32. F.J.W. Whipple and J.A. Chalmers, "On Wilson's Theory of the Collection of Charge by Falling Drops," Quart. Journ. of the Roy. Met. Soc., Vol. 70, pp 103-119, 1944.

33. H. Witt, Insulation Levels and Corona Phenomena on HVDC Transmission Lines, Gumperts, Goteborg: Chalmers Univ. Books, 1960.

34. H.J. White, Industrial Electrostatic Precipitators, Reading: Addison-Wesley, 1963, p. 64.